4D IMAGE RECONSTRUCTION WITH DUAL RESPIRATORY AND CARDIAC MOTION CORRECTION FOR CARDIAC PET

by

Tao Feng

A dissertation submitted to Johns Hopkins University in conformity with the requirements for the degree of Doctor of Philosophy

Abstract

4D image reconstruction with motion correction is the solution to improve image quality and resolution degraded by respiratory motion (RM) and cardiac motion (CM) in cardiac PET scans. The improved image quality can potentially improve clinical diagnosis, and can be traded for reduced injected radiation dose or reduced imaging time for improving patient comfort. There are three steps for 4D image reconstruction with motion correction: 1) 4D data generation (gating), 2) 4D respiratory and cardiac (R&C) motion estimation, and 3) 4D R&C motion correction. We have developed and evaluated multiple methods for each step including (step 1) data-driven gating, MRI-navigator-gating, (step 2) 4 different methods for dual R&C motion estimation after reconstruction (MEAR), CM estimation during reconstruction (MEDR), RM estimation before reconstruction (MEBR), and (step 3) dual R&C motion correction after (MCAR), during (MCDR), and before (MCBR) image reconstruction. Realistic Monte Carlo simulated 4D cardiac PET data using the 4D XCAT phantom and accurate models of the scanner design parameters and performance characteristics and clinical patient data were used to evaluate all different methods. Data-driven gating method was shown to provide robust gating results in high myocardium uptake situations while MRI-navigator based gating showed better results in low myocardium uptake situations. Separate R&C MEAR with modeling of RM on CM estimation was shown to be the best option for accurate estimation of dual R&C motion estimation. The MCDR method yields the best performance for different noise situations for both patient and simulation, while MCBR reduces computational time dramatically but the resultant 4D cardiac gated PET images has overall inferior image quality when compared to that from the MCAR and MCDR approaches in the 'almost' noise free case. Also, the MCBR method has better noise handling properties when compared with MCAR and provides better quantitative result in high noise cases. In general, our developed methods demonstrated the importance of motion correction on image qualities, our work also provide a general guideline for different applications that requires either highly quantitative data or qualitative images. Our works also provide practical means for applying 4D image reconstruction with reasonable computational cost.

Acknowledgments

I would never have been able to finish my dissertation without the guidance of my research advisor and committee members, help from friends and members of DMIP, and support from my family and wife.

I would like to express my deepest gratitude to my advisor, Dr. Benjamin Tsui, for his excellent guidance, caring, patience, and providing me with an excellent atmosphere for doing research. I would like to thank Dr. Blumke, with the support for my research and opportunity for working on PET/MRI. I would also like to thank Dr. Xu, Dr. Ahlman, Dr. Kolbitsch, Dr Faul and Liheng Guo, for the support and guidance for my research.

I would also like to thank my parents. They were always supporting me and encouraging me with their best wishes. Finally, I would like to thank my wife, Jizhe Wang. She was always there cheering me up and stood by me through the good times and bad.

CONTENTS

List of Figures viii

List of Tables xvi

List of Abbreviations xvii

Chapter 1. Introduction 1

1. Overview 1

2. Introduction to Cardiac PET 2

3. PET Systems 4

Instrumentation 4

2D/3D PET 4

List-mode/Sinogram 5

4. PET Physics and Image Degrading Factors 6

Radiation physics 6

Image Degrading Factors 8

5. Image Reconstruction 15

Filtered Back-Projection 15

Statistical Iterative Methods 18

Listmode Reconstruction 20

6. Motion Effects and 4D Image Reconstruction 21

Clinical Relevance and Significance 21

What Has Been Done? 24

What Is Required? 29

7. Contributions of This Dissertation 32

8. Orgnization of This Dissertation 34

Chapter 2. Methods and Materials 36

1. Simulation and Patient Data 36

Introduction to Simulation Tools 36

Realistic Monte Carlo Simulation 39

Acquisition of Patient Data 41

2. Gating Techniques 43

Data-Driven Respiratory Gating 43

MRI Navigator Driven Respiratory Gating 47

ECG Guided Cardiac Gating 47

3. Motion Estimation Techniques 47

Motion Estimation Based on PET Data 48

Motion Estimation Based on Other Modalities 60

Motion from 4DXCAT 61

4. Motion Correction Techniques 63

Dual R&C Motion Correction after Reconstruction (MCAR) 65

Dual R&C Motion Correction during Reconstruction (MCDR) 66

Dual R&C Motion Correction before Reconstruction (MCBR) 71

5. Evaluation Techniques 75

Studies with Known Truth 76

Studies without Known Truth 79

Chapter 3. Result....83

1. Realistic Monte Carlo Simulation 83

2. Gating Techniques 86

Data-Driven Respiratory Gating 86

MRI Navigator Driven Respiratory Gating....87

3. Motion Estimation Techniques 96

Motion estimation based on PET data....96

Motion estimation based on other modalities....107

True motion from XCAT 109

4. Motion Correction Techniques....111

Dual R&C Motion Correction during Reconstruction 111

Dual R&C Motion Correction before Reconstruction....116

Comparison of MCAR, MCDR and MCBR for Dual R&C 117

Chapter 4. Conclusions 136

Gating Techniques....136

Motion Estimation Techniques....137

Motion Estimation after image reconstruction 137

Motion Estimation before image reconstruction 138

Motion Estimation from MR Navigator 139

Motion Correction Techniques 139

Motion Correction after Image Reconstruction 140

Motion Correction during Image Reconstruction 140

Motion Correction before Image Reconstruction 141

Chapter 5. Future Work 142

Reference 144

LIST OF FIGURES

Figure 1-1 Cardiac anatomy and PET images [16]. 3

Figure 1-2. 8-frame ECG gated cardiac PET images with ^{18}FDG. 3

Figure 1-3 Illustration of a PET imaging system. 4

Figure 1-4 Difference between 2D and 3D PET. 5

Figure 1-5 Illustration of a 3D sinogram. 6

Figure 1-6 Attenuation of gamma photon signal in patient body. 10

Figure 1-7 Three types of coincidence. 11

Figure 1-8 Illustration of the law of momentum in the annihilation process. 13

Figure 1-9 Detector response and detector gap. 14

Figure 1-10 Radon transform. 16

Figure 1-11 An illustration of the center slice theorem. 17

Figure 1-12 Transaxial PET/CT images used for detection of lung lesions [52]. 22

Figure 1-13 Cardiac gated images of short-axis view from a noisy simulation study. 22

Figure 1-14 Mis-localization of the lesion (arrow) by the attenuation and the activity map mismatch [55]. 23

Figure 1-15 Artifacts in myocardium caused by mis-match of attenuation and activity [57]. 23

Figure 1-16 Respiratory gating. 25

Figure 1-17 ECG wave of a cardiac cycle and cardiac gating. 26

Figure 1-18 Dual respiratory and cardiac gating with 6 respiratory gates and 8 cardiac gates. 27

Figure 1-19 Tagged MRI in one cardiac cycle from (a) ED to (b) ES to (c) ED. 28

Figure 2-1 General scheme for 4D image reconstruction with R&C motion correction. 36

Figure 2-2 Illustration of the combination of GATE, SIMSET and 4D XCAT. 37

Figure 2-3 Block diagram of the modules in the SimSET software. 38

Figure 2-4. 4D XCAT phantom with cardiac (top) and respiratory (down) motions. 39

Figure 2-5 Illustration of the simulation for FDG tracer uptake from individual organ uptakes. 40

Figure 2-6 Effects of detector non-uniformity and uniformity correction. 40

Figure 2-7 Illustration for the calculation of sinogram contrast. 42

Figure 2-8 Typical look of measured center-of-mass signal in frequency domain. 44

Figure 2-9 Mask used for calculating center-of-mass. 45

Figure 2-10 The scheme for equal amplitude amplitude-gating. 46

Figure 2-11 The scheme for equal counts amplitude-gating. 46

Figure 2-12 Sample image of the 1D navigator over time. 47

Figure 2-13 Illustration of the calculation of voxel-based MVF from control-point based MVF using B-Spline interpolation. 49

Figure 2-14 Image mask used for registration. 50

Figure 2-15 The flowchart for three-step dual respiratory and cardiac MEAR. 50

Figure 2-16 Scheme for combining estimated respiratory and cardiac motion. 51

Figure 2-17 The flowchart for four-step dual respiratory and cardiac MEAR. 52

Figure 2-18 Scheme for combining estimated respiratory and cardiac motion. 52

Figure 2-19 Inverse motion transform used in actual implementation 53

Figure 2-20 The calculation of dual respiratory and cardiac motion based on inverse motion transform. 53

Figure 2-21 The relationship of 3D MVF and motion transformation matrix. 55

Figure 2-22 Illustration of a small change of motion vector in voxel a_5 in target frame. 56

Figure 2-23 Illustration of the effect of motion on LOR and projection data. 59

Figure 2-24 Cases where the approximation can be applied and cannot. 60

Figure 2-25 Illustration of 1D respiratory motion measured using MRI navigator. 61

Figure 2-26 Illustration of linear interpolation model used to calculate 1D respiratory MVF. 61

Figure 2-27 Illustration of a) anatomical structure of the heart, b) cardiac motion from 4D XCAT. 62

Figure 2-28 The difference of motion phases from actual patient and 4D XCAT. 62

Figure 2-29 Two choices of reference frame for true MVF. 63

Figure 2-30 General schemes for a) MCAR, b) MCDR, c)MCBR. 64

Figure 2-31 Flowchart of MCAR for dual respiratory and cardiac motion. 65

Figure 2-32 The use of conventional motion transform scheme results in inaccurate implementation of transpose motion transform. 68

Figure 2-33 2D illustration of new interpolation method for motion transformation. 69

Figure 2-34 Update scheme for simultaneous activity and motion estimation. 71

Figure 2-35 The 2D illustration of effects of image domain motion in projection domain. 72

Figure 2-36 Projection of image domain motion vector. 73

Figure 2-37 Calculation of the error vector. 76

Figure 2-38 Measurement of myocardium FWHM. 77

Figure 2-39 A typical look of the bias-noise curve 79

Figure 2-40 A typical look of the contrast-noise curve. 81

Figure 2-41 Illustration of noise at fixed contrast. 81

Figure 3-1 4D projection data before (a, c) and after (b, d) uniformity correction. 83

Figure 3-2 Conversion to equal-counts amplitude gating from time-based gating of respiratory motion. 84

Figure 3-3 Eight Cardiac gated projection data with three different angles. 85

Figure 3-4 Six Respiratory gated projection data with three different angles. 85

Figure 3-5 Dual gated projection data of five different noise levels. 86

Figure 3-6 Measured center-of-mass signal in frequency domain from a noisy patient scan. 87

Figure 3-7 Sample patient data used for data-driven respiratory gating 87

Figure 3-8 Good match between Data-Driven gating and navigator gating for patient P053. 88

Figure 3-9 Respiratory gated reconstructed images for patients with low myocardium uptakes. 89

Figure 3-10 Respiratory gated reconstructed images for patients with high myocardium uptakes. 90

Figure 3-11 Reconstructed cardiac gated for patient P008. 90

Figure 3-12 Reconstructed cardiac gated for patient M014. 91

Figure 3-13 Reconstructed cardiac gated for patient M024. 91

Figure 3-14 Reconstructed cardiac gated images for patient P053. 92

Figure 3-15 Reconstructed cardiac gated images for patient P055. 92

Figure 3-16 Reconstructed cardiac gated images for patient M007. 93

Figure 3-17 Reconstructed cardiac gated images for patient P057. 93

Figure 3-18 Contrast-noise curve for patient M024 with reduce myocardium uptake. 94

Figure 3-19 Contrast-noise curve for patient with high myocardium uptake. 95

Figure 3-20 The percentage RMSE of dual R&C MVF in myocardium using four motion estimation methods at three different noise levels. 97

Figure 3-21 The percentage RMSE of respiratory MVF in myocardium using four motion estimation methods at three different noise levels. 97

Figure 3-22 The percentage RMSE of cardiac MVF in myocardium using four motion estimation methods at three different noise levels. 98

Figure 3-23 The comparison of true MVF (blue) and estimated MVF (red) using Method 3 and almost noise free image data in (a) short axis view. (b) vertical long axis view and (c) horizontal long axis view. 98

Figure 3-24 . The percentage RMSE of dual R&C MVF in each voxel in the heart plotted in bull's eye plot. 99

Figure 3-25 Transverse view of the myocardium region using 100

Figure 3-26 Convergence curve of MEDR. 102

Figure 3-27 MEDR and MEAR from end systole to end diastole, using noise-free projection data. 103

Figure 3-28 Motions estimation from ES to ED using clinical noise level 3D PET projection data. 103

Figure 3-29 Percentage RMSE of 3D MVF estimation from different frames using noisy data. 104

Figure 3-30 Angle distribution of total Percentage RMSE of using noisy data. 104

Figure 3-31 Colonial view of the reconstructed image for one respiratory gate. 105

Figure 3-32 Profiles from different respiratory gated frames using 106

Figure 3-33 3D VOI around the heart used for measuring the change of COM due to respiratory motion. 106

Figure 3-34 The relative motion along vertical axis measured using the COM of the heart region. 107

Figure 3-35 Short axis view for patient P057 without cardiac gating and cardiac motion correction 108

Figure 3-36 Contrast-noise curve for comparing navigator based motion and MEAR 108

Figure 3-37 MCDR using original 4D XCAT MVF (second row) and smoothed 4DXCAT MVF (Third row) compared with the original phantom (first row). 110

Figure 3-38 Cardiac gated images of multiple iteration using R&C MCDR with unsmoothed MVF from 4D XCAT. 111

Figure 3-39 Cardiac gated images of multiple iteration using R&C MCDR with smoothed MVF from 4D XCAT. 111

Figure 3-40 Sample short axis view of the cardiac gated images of using different reconstruction methods. 112

Figure 3-41 RMSER and measured FWHM across the myocardium wall at different iteration numbers ..113

Figure 3-42 Short axis view of cardiac gated images using 114

Figure 3-43 Normalized bull's eye map for left ventricle for both ED and ES using AP an NAP. 115

Figure 3-44. Comparison of activity of the heart with activity preserving and non-activity preserving model. 115

Figure 3-45 Coronal view of end-systolic phase of (left) phantom image, (middle) motion correction using reference frame choice 1, (right) motion correction using reference frame choice 2. 116

Figure 3-46 RMSER of 8 cardiac gate with MCBR using choice 1 and choice 2. 117

Figure 3-47 Short-axis cardiac gated PET images from a patient PET scan (V001). 118

Figure 3-48 Contrast-to-noise plot from a patient V001 using three different image reconstruction methods. 119

Figure 3-49 Short-axis view of cardiac gated PET images from patient scan M007 120

Figure 3-50 Contrast-to-noise plot from a patient scan M007 using three different image reconstruction methods. 121

Figure 3-51 Short-axis view of cardiac gated PET images from patient scan P053. 121

Figure 3-52 Short-axis view of cardiac gated PET images from patient scan P055. 121

Figure 3-53 Short-axis view of cardiac gated PET images from patient scan M007. 121

Figure 3-54 Short-axis view of cardiac gated PET images from patient scan P057. 122

Figure 3-55 Short axis view of cardiac gated images using almost noise free simulation data. 123

Figure 3-56 RMSER and measured FWHM of myocardium wall in different image iterations. 124

Figure 3-57 Short axis view of cardiac gated images using simulation data of a 20 minutes scan. 124

Figure 3-58 Short axis view of cardiac gated images using simulation data of a 10 minutes scan. 125

Figure 3-59 Short axis view of cardiac gated images using simulation data of a 5 minutes scan. 125

Figure 3-60 Short axis view of cardiac gated images using simulation data of a 3 minutes scan. 125

Figure 3-61 Image-based noise estimation and ensemble-based noise estimation using no motion correction. 126

Figure 3-62 Image-based noise estimation and ensemble-based noise estimation using MCBR. 127

Figure 3-63 Image-based noise estimation and ensemble-based noise estimation using MCAR. 127

Figure 3-64 Image-based noise estimation and ensemble-based noise estimation using MCDR. 128

Figure 3-65 Contrast-noise curves using image-based nosie estimations for dual R&C motion correction129

Figure 3-66 Contrast-noise curves using ensemble-based nosie estimations for dual R&C motion correction 130

Figure 3-67 Bias-Noise tradeoff curve of three different dual R&C motion correction methods using.....131

Figure 3-68 Measured RMSER of different noise levels using MCBR, MCAR, and MCDR using true motion vector field from XCAT.....132

Figure 3-69 Short axis view of cardiac gated images using almost noise free simulation data.....133

Figure 3-70 Short axis view of cardiac gated images using simulation data of a 20 minutes scan. 133

Figure 3-71 Short axis view of cardiac gated images using simulation data of a 10 minutes scan. 133

Figure 3-72 Short axis view of cardiac gated images using simulation data of a 5 minutes scan. 134

Figure 3-73 Short axis view of cardiac gated images using simulation data of a 3 minutes scan. 134

Figure 3-74 Measured RMSER of different noise levels using MCBR, MCAR, and MCDR using individual estimated MVF.....135

LIST OF TABLES

Table 2-1 List of Patient data used in this study. 41

Table 3-1 Total counts in the center slice for different noise levels. 85

Table 3-2 List of patient used in comparing PET data-driven and MRI navigator gating. 88

Table 3-3 Noise at fixed contrast = 50% maximum. 95

Table 3-4 Noise at fixed contrast = 80% maximum. 96

Table 3-5 Correlation coefficient using noisy image and estimated MVF. 100

Table 3-6 Correlation coefficient using almost noise free image and estimated MVF. 101

Table 3-7 Noise at fixed contrast = 50% maximum. 108

Table 3-8 Noise at fixed contrast = 80% maximum. 109

Table 3-9 Patient list for comparison of MCDR and MCAR. 117

Table 4-1 Pros and cons for PET-based and MRI-based respiratory gating methods. 136

LIST OF ABBREVIATIONS

1

^{18}F-FDG

^{18}F labeled fludeoxyglucose 1

A

AP

activity-preserving 31

B

BGO

Bismuth germinate 4

C

CAD

coronary artery disease 2

CC

correlation coefficient 79

CHO

Channelized hoteling observer 143

CM

cardiac motion 21

COM

center of mass 25

CT

computed tomography 1

D

DOI

depth of interaction....14

E

ECG

electrocardiography....3

ED

end-diastolic....3

EM

expectation maximization....19

ES

end-systolic....3

F

FBP

filtered back projection....1

FWHM

Full width at half maximum....77

G

GATE

Geant4 Application for Tomographic Emission....37

H

HLA

horizontal long axis....2

L

LOR

line of response....1

M

MCAR

Motion correction after image reconstruction 28

MCBR

Motion correction after image reconstruction 28

MCDR

Motion correction after image reconstruction 28

MEAR

Motion/MVF estimation after image reconstruction 28

MEBR

Motion/MVF estimation before image reconstruction 28

MEDR

Motion/MVF estimation during image reconstruction 28

ML-EM

maximum likelihood expectation maximization 1

MP

myocardial perfusion 38

MPI

myocardium perfusion imaging 2

MRI

Magnetic resonance imaging 10

MTM

motion transformation matrix 54

MVF

motion vector field 27

N

NAP

non-activity-preserving 31

NAV

1D MRI navigator 107

NMC

original data without motion correction 107

NURBS

non-uniform rational b-splines 38

O

OS-EM

ordered subset expectation maximization 1

P

PET

Positron Emission Tomography 1

PHG

Photon History Generator 38

PMTs

photomultiplier tubes 4

PVE

partial volume effects 70

R

R&C

respiratory and cardiac 24

RM

respiratory motion 21

RMSE

root mean square error 76

RTA

registration-transformation-average 65

S

SA

short axis 2

SPECT

single photon emission computed tomography 2

T

TOF

time-of-flight 10

V

VLA

vertical long axis 2

VOI

volume of interest 76

X

XCAT

NURBS-based Cardiac-Torso 37

CHAPTER 1. INTRODUCTION

1. OVERVIEW

Positron Emission Tomography (PET) [1] is an imaging technique that detects the three dimensional distributions of an tracer amount of administrated radio-pharmaceuticals inside the human body, providing functional information of the body. PET is used for cancer diagnosis and treatment evaluation [2], brain function evaluation [3], and heart function evaluation [4].In this dissertation, our main focus is its application in cardiac study.

The radio-pharmaceutical, or tracer, is a molecule labeled with radioactive isotope and is essential for PET imaging. An example is ^{18}F labeled fludeoxyglucose (^{18}F-FDG), which is widely used in PET imaging to provide *in vivo* information of glucose metabolism. The radio-isotope ^{18}F emits a positron during each decay process, and the positron annihilates with an electron and produces a pair of 511 KeV energy photons travelling in the opposite direction. The photon pair is detected by the PET scanner, which identifies one line of response (LOR). To get activity distribution from recorded LORs, image reconstruction is required.

There are two types of image reconstruction algorithms. One is based on an analytical model [5], such as the filtered back projection (FBP) method; the other is based on a statistical model, and often requires iterative algorithms, such as maximum likelihood expectation maximization (ML-EM) [6, 7] and ordered subset expectation maximization (OS-EM) [8]. Analytical image reconstructions are fast and widely used in computed tomography (CT), but for the application in PET, analytical image reconstruction approaches are less desirable options as the image is greatly affected by noise and degraded by image degradation factors such as scatter, and finite detector resolution. To model the above mentioned image degradation factors and improve image noise characteristics, statistical image reconstructions have been developed, and the image quality is improve by modeling those image degradation factors. Using 4D PET reconstruction with modeling of motion will improve the image quality even further, which is the main topic of this dissertation.

2. INTRODUCTION TO CARDIAC PET

The human heart plays an important role in the human body by pumping blood into the circulatory system that supplies the body with oxygen, nutrients and helps removes metabolic wastes. Heart diseases such as cardiovascular abnormalities and conditions that affect muscle, valves or rhythm of the heart have received great attention in clinical, academic research, and industries [9].

As a specific PET imaging application, cardiac PET [10] aims at providing images of human heart for diagnosis of heart disease such as coronary artery disease (CAD), which is the leading cause of death in the world. PET imaging techniques provide multiple means for detecting CAD, such as myocardium perfusion imaging (MPI) [11], the evaluation of abnormality in myocardium wall motion[12] and ejection fraction [13], and more recently plaque imaging [14]. In the procedure of MPI, the cardiac PET requires intravenous injection of radioactive blood flow marker. Commonly used perfusion agent includes Rubidium-82 and Nitrogen-13 ammonia [15]. The uptake of the radioactive tracer in the myocardium is mainly influenced by the condition of the coronary arteries. In presence of cardiovascular disease, the coronary artery is narrowed or blocked, which can lead to heart attack, stroke, or even heart failure. The reduced blood flow of the blocked vessels results in lack of perfusion in the certain region of the myocardium, which will be reflected as a "cold" region in the myocardial perfusion PET images. Therefore, images provided by the PET scanner can be used to identify regional abnormalities in coronary artery blood flow and evaluate myocardial function and viability. Figure 1-1 shows the anatomy of the human heart and the corresponding myocardial perfusion PET image [16] with Nitrogen-13 ammonia in short axis (SA), vertical long axis (VLA), and horizontal long axis (HLA). A perfusion defect pointed by the arrow can be observed from the image.

In cardiac PET imaging, non-perfusion agent such as ^{18}FDG can also be used to assess the metabolism in the heart and cardiac viability in order to diagnose disease such as cardiac sarcoidosis [17]. Although perceived as more expensive in comparison to general nuclear medicine cardiac testing using single photon emission computed tomography (SPECT), cardiac PET has advantages in better image resolution, system sensitivity. The assessment of functional abnormalities of the coronary vessels and myocardium allowed by

cardiac PET imaging makes it a widely accepted imaging technique in clinical diagnosis of coronary artery/heart disease.

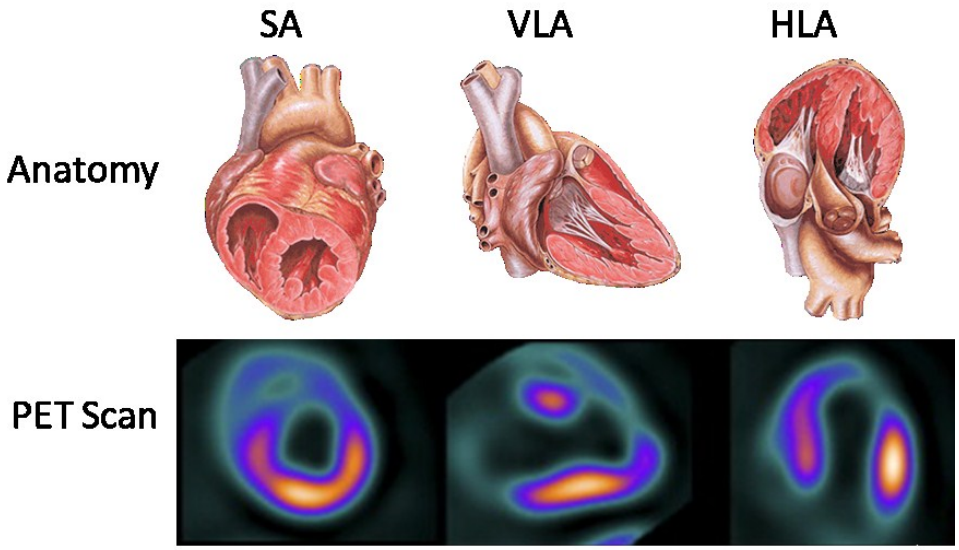

Figure 1-1 Cardiac anatomy and PET images [16].

Besides functional information of the heart, cardiac PET also has the potential in revealing the abnormalities in cardiac motion. Cardiac PET data acquired with the simultaneous recording of the electrocardiography (ECG) signal can be divided into several gates based on the cardiac phases. Motion of the myocardium is visualized as the change of shape of the heart in the gated cardiac images during the cardiac cycle. Figure 1-2 shows a set of cardiac PET images at 8 cardiac phases based on ECG gating. Starting from end-diastolic (ED) phase, the heart contracts until end-systolic (ES) phase and then expands back to ED phase in the last frame. Gated cardiac PET images contain important information on cardiac motion and can be used to detect and evaluate motion defects.

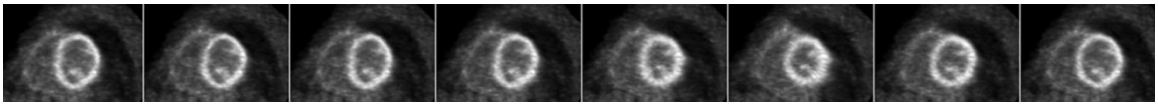

Figure 1-2. 8-frame ECG gated cardiac PET images with ^{18}FDG.

3. PET SYSTEMS

INSTRUMENTATION

Imaging of the distribution of the radiotracer in the patient body relies on the detection of the gamma photon pairs generated from positron annihilations. A typical clinical PET imaging system consists of gamma photon detector rings, electronics for pulse processing and coincidence detection, and image reconstruction module, as shown in Figure 1-3. Detector rings are composed of several blocks of gamma photon detectors. In the photon detector, scintillation crystals such as Bismuth germinate (BGO) are coupled with photomultiplier tubes (PMTs), and together they generate electrical signal for incoming gamma photons. The gamma photons generated from annihilation interact with scintillation crystal through Compton scatter and photoelectric effect, exciting free electrons in the crystal which generate visible light photons after returning to lower energy state. The PMTs coupled to the end of the crystal collect the visible light photons and transform the light signal to an electrical signal which is further amplified by the multi-level photo-diodes in the PMTs. The electrical signal is analyzed in the electronics of PET system to identify the location and energy of the incident gamma photon.

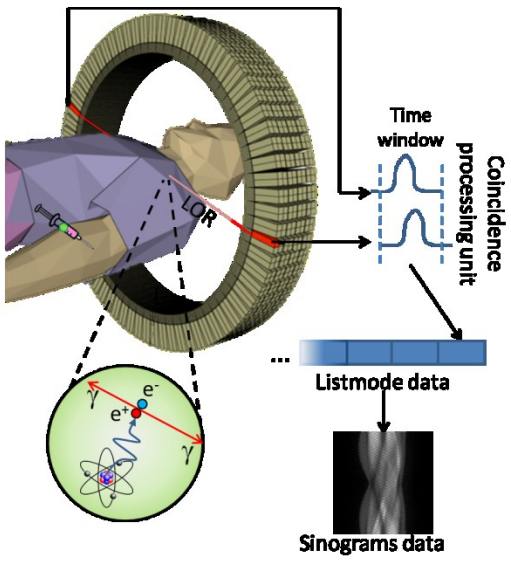

Figure 1-3 Illustration of a PET imaging system.

2D/3D PET

Historically there are two modes of PET data acquisition: 2D mode and 3D mode. In 2D mode, axial septa made of lead or tungsten is mounted in front of the detector to separate each crystal ring. As a result, only gamma photon pairs that are detected by the same detector ring or in two adjacent rings are accepted. In 3D mode, there will be no septa and coincidences detected by any two rings will be recorded, yielding 2~4 times more LORs and much higher sensitivity than that of 2D mode. This also means that more scattered and random coincidences will be accepted by the detector. The properties of 2D and 3D PET are shown in Figure 1-4. Currently most PET scanners operate 3D mode mainly because of its high sensitivity. With proper scatter and random correction, the performance of 3D PET is more favorable than 2D PET.

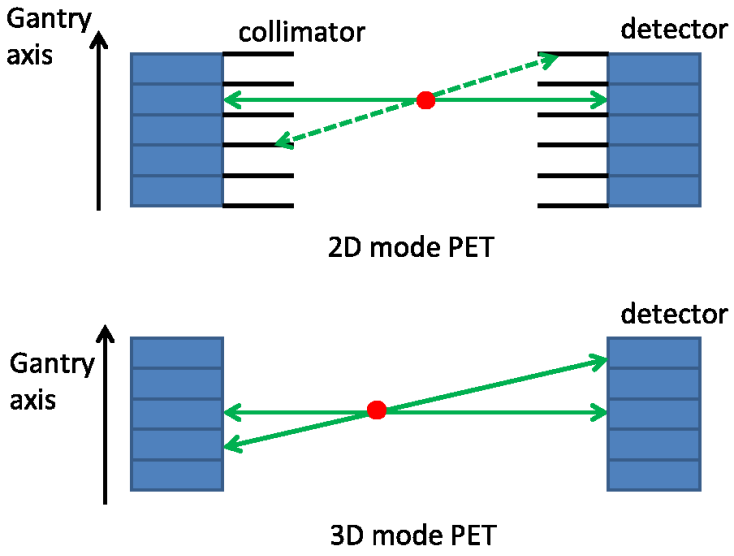

Figure 1-4 Difference between 2D and 3D PET.

LIST-MODE/SINOGRAM

There are two types of data format that are used by PET scanner to record the incident gamma photons. The list-mode acquisition records the information of every event such as energy, ring number sequentially with time stamps. The list-mode PET data contain all the possible information during the scan and require a large storage size. PET data can also be stored in the sinogram format, in which the events during certain period of time are accumulated into one sinogram. The two data formats are shown in Figure 1-3. List-mode PET data can be easily transformed to the sinogram format, but not the vice versa since the sinogram

PET data do not record information of every single event. Sinogram is three dimensional with three axis: detector bin number, angle, z, as shown in Figure 1-5.

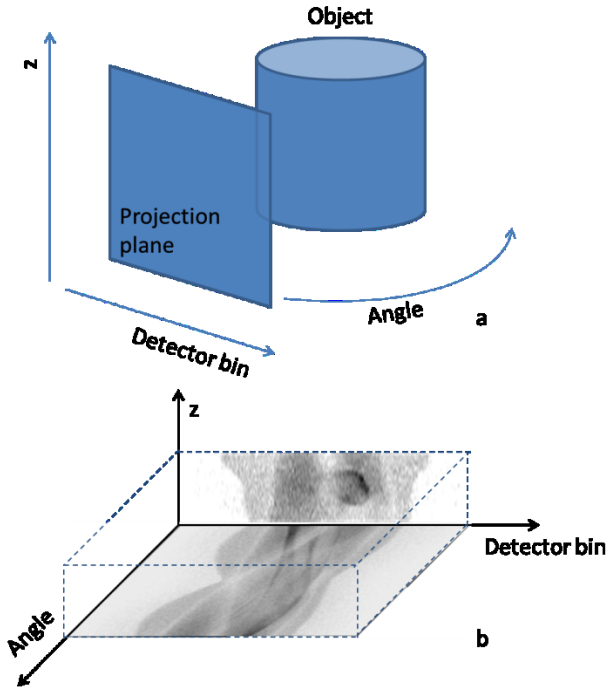

Figure 1-5 Illustration of a 3D sinogram.

(a) Geometric relationship with the original object, (b) data format

4. PET PHYSICS AND IMAGE DEGRADING FACTORS

RADIATION PHYSICS

Radioactive tracer employed in PET imaging undergoes beta decay which results in emission of a positron.

The generic equation of beta decay is [18]:

$$ {}^{A}_{Z}X \rightarrow {}_{Z-1}{}^{A}X' + e^{+} + v_e \, , $$

Equation 1-1

where X and X' represent certain element and Z is the atomic number while A is the mass number, e^{+} is a positron while v_e is a neutrino.

When the emitted positron encounters an electron from the surrounding material, the collision of the positron and electron results in annihilation of both particles and the generation of a pair of gamma ray photons:

$$e^- + e^+ \rightarrow \gamma + \gamma$$

Equation 1-2

The two gamma ray photons travel in opposite directions and each has an energy of 511keV.

The gamma photons go through three types of interactions with physical matters in the patient body and the detector crystals. The first type of interaction is photoelectric absorption in which the gamma photon completely disappears and its energy is transferred to one of the bounded orbital electrons of an atom in the absorbing material. The electron is ejected from the atom with a kinetic energy equal to the gamma photon energy minus its binding energy. The possibility of the photo-electric absorption is determined by the effective atomic number Z_{eff} of the absorbing matter and the photon energy E_γ in the following equation:

$$p \propto \frac{Z_{eff}^4}{E_\gamma^3}$$

Equation 1-3

The second type of interaction is Compton scattering during which the gamma photon collides with a free electron. Part of the energy of the incident gamma photon is transferred to the kinetic energy of the electron and gamma photon changes its direction after the encounter. The remaining energy of the gamma photon $E_{\gamma'}$can be calculated by the following equation:

$$\frac{E_{\gamma'}}{E_\gamma} = \frac{1}{1 + \frac{E_\gamma}{m_e c^2}(1 - cos\theta)}$$

Equation 1-4

where E_γ is the energy of the incident photon, m_e is the rest mass of an electron, c is the speed of light and θ is the scattering angle with respect to the incident direction. The Compton scattering obeys the

conservation of energy and momentum. The differential cross-section of Compton scattering is provided by Klein-Nishina formula [19]:

$$\frac{d\sigma}{d\Omega} = \alpha^2 r_c^2 (\frac{E_{\gamma'}}{E_\gamma})^2 \left[\frac{E_{\gamma'}}{E_\gamma} + \frac{E_\gamma}{E_{\gamma'}} - 1 + cos^2\theta\right]/2$$

Equation 1-5

In which Ω is the solid angle, α is the fine structure constant (~1/137.04), $r_c = \frac{\hbar}{m_e c^2}$ is the Compton radius of an electron. Since Compton scattering is the interaction between the gamma photon and a free electron in the absorbing material, its probability is approximately proportional to the electron density of the interacting matter and is not sensitive to the photon energy for gamma photon used in PET.

The third type of interaction is coherent scattering. No energy is lost during this process and the gamma photon only changes its traveling direction. In PET imaging, the interaction between gamma photons of 511 keV and the patient body is dominated by Compton scattering and the effect of photoelectric absorption is negligible [20]. When the energy of the gamma photon is reduced to around 20 keV after experiencing multiple Compton scatterings, the photoelectric absorption is dominant. The probability of coherent scattering is very low compared with Compton scattering and therefore is not considered in PET.

IMAGE DEGRADING FACTORS

The image quality of a PET system is influenced by a few physical factors. Research has been carried out to reduce the effect of these factors in order to achieve higher image quality.

POSITRON RANGE

The positrons emitted from the radioactive element travels a distance before they reach thermal energies to annihilate with electrons. This distance is called the positron range. It is usually in the range of 1~4 mm [21], depending on the energy of the positron-emitting isotopes. Due to the positron range, the reconstructed annihilation location based on LOR is not the real location of the radio-isotope. Hence the resolution of the PET system is limited. Fortunately, there are two possible ways to reduce the influence of

the positron range. One way is to apply a strong magnetic field which will reduce the positron range by Lorentz force [22]. Another way is to incorporate the positron range into the system matrix [23] to improve image resolution and even the noise properties [24].

ATTENUATION

The gamma photons emitted from the annihilation event may not be able to escape the patient body and arrive at the scanner due to the interactions described above. The reduction of gamma photon after passing through the material is called attenuation. In the narrow beam mono-energetic photon model, as shown in Figure 1-6, the attenuation of the gamma photon 1 and in the patient body is determined by the attenuation coefficient of the body tissue along the photon path:

$$P_1 = e^{-\int_0^{l_1} \mu(l) d\vec{l}}$$

$$P_2 = e^{-\int_0^{l_2} \mu(l) d\vec{l}}$$

Equation 1-6

Where P_1 and P_2 are the probabilities that photon 1 and 2 escape the patient body without being absorbed, $\mu(l)$ is the attenuation coefficient at location l, $\vec{l}$ is the line along which the LOR is located. Attenuation coefficient is a measurement of a material's ability to interact with the passing photon through the above mentioned types. Therefore, the probability of the gamma photon pair arriving at the detector without interaction is:

$$P = P_1 P_2 = e^{-\int_{-l_1}^{l_2} \mu(l) dl}$$

Equation 1-7

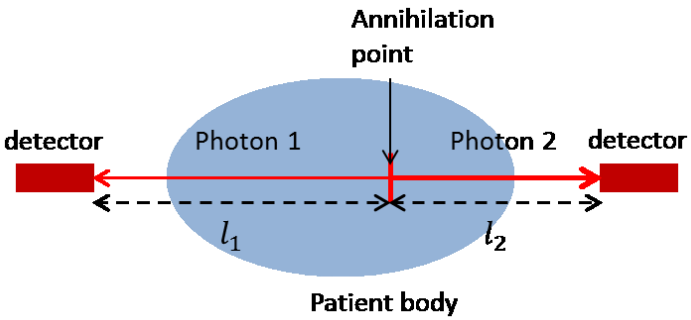

Figure 1-6 Attenuation of gamma photon signal in patient body.

Attenuation of photon by patient body results in inaccurate estimation of activity distribution. Notice that in PET imaging, attenuation along the LOR is independent of the location of annihilation point on the LOR.

In the early days, the attenuation correction method for 2D PET is to measure the attenuation along every LOR using a radioactive rod source. The rod source is placed close to the imaging object and rotated around the scanner axis [25]. The measured attenuation factors can be used directly to recover the original activity at each LOR. An attenuation map can be reconstructed from the transmitive projection data acquired with the rod source, and proper image processing techniques such as segmentation and smoothing can help reduce noise in the attenuation map. However, this method is still significantly limited by the noise in the detected counts from the rod source as well as the radiation dose. Furthermore, it is not practical for 3D PET in which the number of LORs is fundamentally larger.

To obtain an accurate attenuation map for attenuation compensation in PET data, other imaging modalities such as X-ray CT and Magnetic resonance imaging (MRI) are combined with PET scanner in 3 multi-modality imaging systems. In a PET/CT scanner, the CT unit provides high-resolution image of the attenuation coefficient of patient body which can be used for attenuation correction in PET [20]. Another benefit of the CT unit is the anatomical information it provides. In simultaneous PET/MRI, both segmentation based [26] and atlas based [27] attenuation correction are being studied. A novel approach of using time-of-flight (TOF) PET data alone was also proposed [28] and could potentially achieve attenuation correction without the addition of other modalities.

CO-INCIDENCE DETECTION

Gamma photons that fall into a coincident timing window are recognized as a coincidence event by the coincidence detection circuits in the PET system. The detected locations of the two coincident photons on the detector ring specify the path of the two photons through the body, which is defined as a LOR. The LOR will be used to find the location of the annahilation during image reconstruction process. However, not all coincident events detected by the gamma camera are "true coincidence" in which the two gamma photons are generated from one positron annihilation and travel through the patient body without any interaction. Figure 1-7 shows three types of coincident events. Among the three type of coincidence, only the true coincidence provides accurate information of the annihilation location. Both scattered and random coincidences increase background counts and result in reduced image contrust and increased noise. Scatter and random correction can be applied to total detected events by subtracting an approximation of scatter and random events.

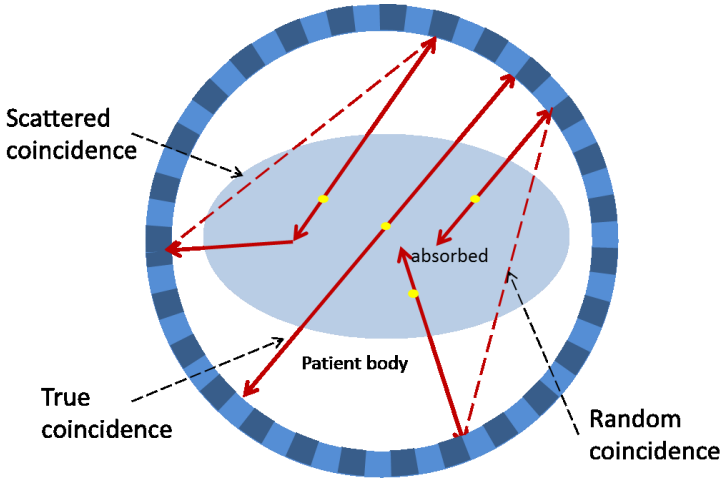

Figure 1-7 Three types of coincidence.

In some cases, the gamma photons may experience Compton scattering while travelling through the body before being detected, resulting in decreased photon energy and altered photon path. This is called scattered coincidences. The energy resolution and the associated lower energy threshold of the detector determine the acceptance of scattered events. Furthermore, the two or even more gamma photons that reach the detecter within the same coincidence window and are recognized as one coincidence event may not come from the same positron annihilation. This situation is called random coincidence. The rate of random

coincidence along the LOR connecting detectors i and j is mathematically modeled using the following equation:

$$R = 2\tau R_i R_j$$

Equation 1-8

Where τ is the width of coincidence timing window, R_i and R_j are the rates of detecting single gamma photons at detectors i and j.

Accurate estimation of the random and scatter coincidences is crucial to recover the true coincidence and reconstruct the true distribution of the radio tracer. For random coincidence estimation, there are two methods. The first method is to estimate the rate of random coincidences using Equation 1-8. Accurate measurement of the single gamma photon rate at each detector pixel is critical to the accuracy of this method. Since the single rates in a particular acquisition are generally much higher than the coincidence rates, the statistical quality of the estimated rancom coincidence rate tends to be good. The second method, called the delayed coincidence channel method [29], uses the number of coincidences acquired with a delayed time window to approximate the number of random coincidences. For the delayed coincidences, the timing signals from one detector are delayed by 3~5 times of the width of the coincidence timing window so there will be no true coincidences in the delayed coincidence channel. Although the count of delayed coincidence events is proven to be an unbiased estimate for the count of real random coincidences, it is noisy since the random coincidence rate is much smaller than the singles rates.

The influence of scattered coincidences is more prominent in 3D PET than in 2D since the amount of scatter in the signal has the same order of magnitude as the true coincidences [30]. Methods proposed for scatter correction in 3D include, model-based scatter correction algorithms [31], the “Gaussian fit” approach [32], the convolution-subtraction method [33], Monte-Carlo modelling methods [34], the multiple energy window method [35], and the direct measurement method [36]. The model-based approach uses the Klein-Nishina formula to calculate the scatter coincidence rate based on the emision data and the attenuation map as well as the model of the imaging system. One example of the model-based methods is the single scatter simulation method [37] that calculates the counts of single scattered coincidences along

each LOR assuming only one of the two detected gamma photons is scattered once. Multiple-scattered coincidence rates can be modeled based on the convolution of the single scattered coincidence counts and a proper kernel. Monte-Carlo based methods are generally more accurate than model-based methods but are more computationally costly. Each of these methods has its own limitations and scatter correction remains an active research topic in 3D PET.

NON-COLLINEARITY

The coincident detection of LOR is based on the assumption that the photons produced in Equation 1-2 travel in the opposite direction, which is not always true as the momentum of the positron before annihilation is not necessarily zero. Non-collinearity is the result of a non-zero momentum of the positron which is illustrated in Figure 1-8, where the total momentum of the two photons p_1 and p_2 is equal to the total momentum of the electron and positron p_{e-} and p_{e+}

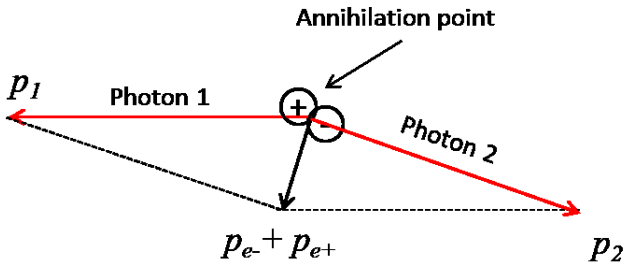

Figure 1-8 Illustration of the law of momentum in the annihilation process.

Fortunately, the effect of non-collinearity is not as dramatic as shown in Figure 1-8. A study by K. Shibuya1 [38] using *in vivo* ^{18}FDG showed that the distribution of the angles between the two photons was approximately a Gaussian distribution with FWHM of 0.54 degree centered at 0 degree, which resulted in ~2.1mm resolution degradation for a system with scanner diameter being 80 cm.

DETECTOR RESPONSE AND DETECTOR NON-UNIFORMITY

Besides positron range and scatter of the gamma photon within the patient body, the interaction between the gamma photon and the detector also limits the spatial resolution of PET imaging. As depicted inFigure 1-9, the incident gamma photon travels a certain distance in the scintillation crystal before it interacts with

the crystal material. This distance is called depth of interaction (DOI). The photon may also change direction and energy due to Compton scattering while traveling in the scintillation crystal. Meanwhile, the visible light photons created due to the relaxation of excited electrons are emitted in all directions, so only the part that travel toward the PMT are collected and used to identify the incident location of the gamma photon. Furthermore, gamma photons may travel through and interact with different crystal pieces. In the end, the location calculated based on the light signal detected by the PMTs is no longer the true incident location due to the complex physical interaction of the gamma photon in the detector. The blurring effect of the detector to the gamma photon signal is defined as the detector response. Approaches to obtain a good estimation of the detector response include direct measurement using point source [39]. Both analytical approximation and statistical model of the detector response function have been introduced and incorporated into the system matrix to achieve accurate modeling of the imaging process [40-42]. On the hardware aspect, researchers are working on developing scintillation crystals with strong stopping power and high spatial resolution to reduce the blurring of the detector response. Detectors with DOI encoding capabilities are also designed and utilized for more accurate estimation of the interaction location of the gamma ray in the detector to improve the system resolution [43].

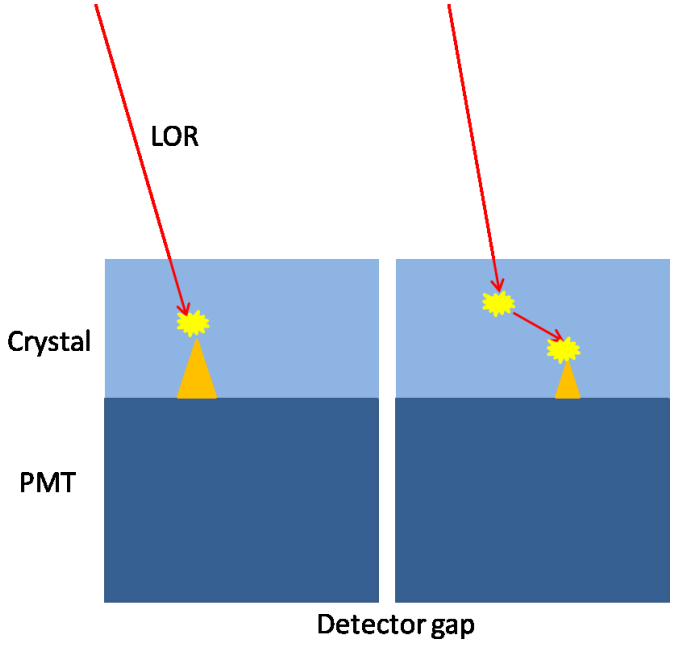

Figure 1-9 Detector response and detector gap.

Since the scintillation crystals and the PMTs are not identical, different detector blocks have different sensitivities. In other words, the detectors are not uniform. The quantitative accuracy of image reconstruction requires that every LOR is received by the detector with the same sensitivity. The compensation for the non-uniformity of the detector is called normalization. A straightforward method is to multiply the detected LOR with the corresponding detector coefficient, which is calculated from experimental scan with a known source [44]. The accuracy of the measured detector coefficient is limited by the statistics of the normalization source, but dead-time effects of the detector prevent the use of high-activity sources. Component-based normalization techniques [45, 46] are developed to improve the accuracy of normalization coefficients without high requirement on the normalization source.

5. IMAGE RECONSTRUCTION

Image reconstruction techniques are required to create images of activity distribution based on gamma photon pairs received by the detectors.

FILTERED BACK-PROJECTION

Assuming a simplified 2D scenario shown in Figure 1-10, the goal of image reconstruction is to determine the radiotracer distribution in the patient body $f(x, y)$ from projection $p(s, \theta)$. Neglecting image degrading factors such as attenuation effects, the basic relationship between activity map and projection data is described by the 2D Radon transform [18]:

$$p(s,\theta) = \iint_{R\times R} f(x,y)\delta(xcos\theta + ysin\theta - s)dxdy$$

Equation 1-9

In other words, the projection of the intensity map in a certain direction is its line integral. Note that the 1D Fourier of the projection is equal to the 2D Fourier transform of the intensity map along the projection direction, which is called the central slice theorem (Figure 1-11).

$$P(S,\theta) = F(Scos\theta, Ssin\theta)$$

Equation 1-10

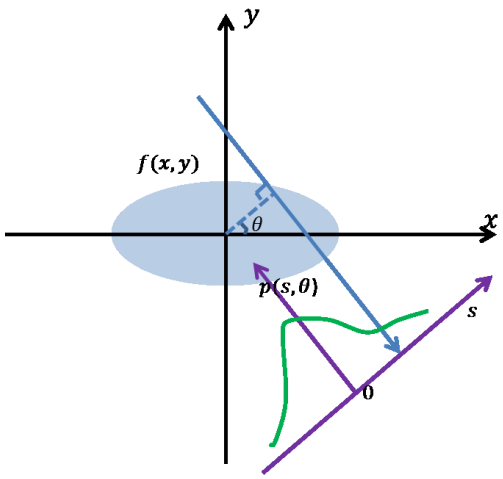

Figure 1-10 Radon transform.

FBP [5] is a well-established analytical image reconstruction method. Using inverse Fourier transform and the central slice theorem, the activity image is calculated by the following equation:

$$f(x,y) = \int_0^{\pi} \int_{-\infty}^{\infty} P(S,\theta) e^{2\pi i S l} |S| dS|_{l=xcos\theta+ysin\theta} d\theta$$

Equation 1-11

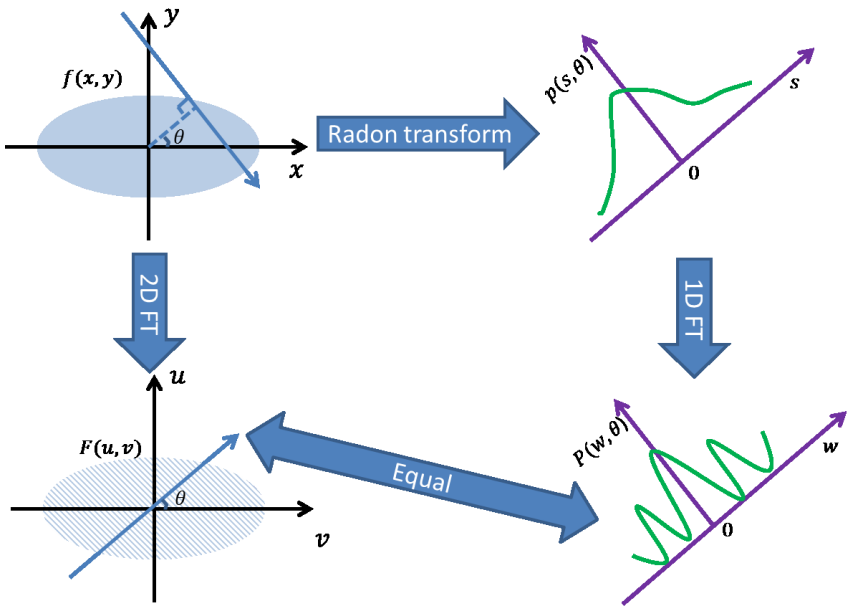

Figure 1-11 An illustration of the center slice theorem.

The $|S|$ acts as a high pass filter which is called the ramp filter, it increases the influence of high frequency in $P(S,\theta)$. Essentially, the solution is a back projection of the filtered Fourier transform of the projection data. To avoid aliasing problem, the ramp filter is usually multiplied by a low-pass window function.

In a general sense, the projection process is simplified as the following discrete model:

$$\boldsymbol{g = Hf}$$

Equation 1-12

Where f is a vector that represents the image space, g is the projection, and H is the system matrix. The filtered back projection method tries to obtain the image f by inverting the projection process. However, since there is always noise in the projection data $\boldsymbol{g = (H_{Radon} f_{true} + n)}$, the solution by FBP method will be:

$$\hat{\boldsymbol{f}} = \boldsymbol{B_{FBP} g = B_{FBP}(H_{Radon} f_{true} + n) = f_{true} + B_{FBP} n}$$

Equation 1-13

With the ramp filter in the $\boldsymbol{B_{FBP}}$, noise will be amplified.

In realistic case, attenuation effect is an important factor that affects the quantitative accuracy of the reconstruction. Equation 1-7 suggests that for a fixed LOR, the attenuation effects does not depend on the location of annihilation, in this case, the attenuation effects can be compensated prior to image reconstruction. Other factors such as scatter can also be corrected on the projection data but such corrections are usually approximations and less accurate. The use of ramp filter in Equation 1-11 also amplifies image noise. Because of its limitations, the FBP method is not widely used in clinical situations.

STATISTICAL ITERATIVE METHODS

To better handle the noise in PET data and model the image degrading factors that affect image quality, statistical iterative algorithms seek to find the radioactivity distribution by incorporating assumptions about the statistical distribution involved in the data acquisition. ML-EM [6, 7] and the OS-EM [8] which is the acceleration of ML-EM are the most widely used statistical iterative image reconstruction methods.

The projection data is regarded as a random realization of a Poisson distribution with a mean value determined by the unknown radioactivity distribution and the system matrix. Assuming projection bin values are independent, the probability of getting the projection data is:

$$Prob[\boldsymbol{p}|\boldsymbol{x};\boldsymbol{K}] = \prod_i \left(\left(\sum_j K_{ij} x_j \right)^{p_i} (p_i!)^{-1} \exp\left(- \sum_j K_{ij} x_j \right) \right)$$

Equation 1-14

In the above equation, x_j is the activity at pixel or voxel j, p_i is the photon counts at detector bin i, and K_{ij} is the system parameter that determines the contribution of voxel j to detector i. The goal is to find the activity map estimate $\boldsymbol{x}$ that maximizes the probability function.

ML-EM

The ML-EM method uses the expectation maximization (EM) algorithm to find the activity distribution map that maximizes the likelihood function (Equation 1-14). To simplify the equation, the conditional expectation of the log likelihood function of the process in Equation 1-14 is often used.

$$E\{\log Prob[p|\hat{x};K\} = \sum_i \sum_j -K_{ij}\hat{x}_j + \frac{K_{ij}\hat{x}_j}{\sum_k K_{ik}\hat{x}_k} p_i \log\left(K_{ij}\hat{x}_j\right) + R$$

Equation 1-15

The update formula given by the EM approach is

$$\hat{x}_j^{l+1} = \frac{\hat{x}_j^l}{\sum_i K_{ij}} \sum_i K_{ij} \frac{p_i}{\sum_{j'} K_{ij'}\hat{x}_{j'}^l}$$

Equation 1-16

The term $\sum_{j'} K_{ij'}\hat{x}_{j'}^l$ is called the projection step since it calculates the expectation of the projection value based on the current image estimate. The term $\sum_i K_{ij} \frac{p_i}{\sum_{j'} K_{ij'}\hat{x}_{j'}^l}$ back-project the ratio between the expectation of projection and the acquired projection value to the image space to update the image estimate. The term $\sum_i K_{ij}$ is known as the sensitivity map, it represents the probability that a decay at voxel j is detected by the detector ring. l is the iteration number.

The ML-EM image reconstruction algorithm is generally convergent [47]. Since the update is multiplicative, it is easy to impose non-negative constraint on the voxel intensities which is consistent with the PET imaging situation.

OS-EM

It is computationally expensive to update all image voxels using all the LORs during each iteration as in ML-EM algorithm. The OS-EM algorithm was developed to reduce the computational cost by updating the image estimates one subset of projection at a time. The LORs are grouped into M subsets S_m $(m = 0,1,\ldots,M-1)$ to make sure each certain LOR. belongs to only one subset at a time. In each iteration, there

will be M updates, and each time image estimation is updated by using one subset. Here is the description of iteration l in the OS-EM algorithm:

For $m = 0,1, \dots, M-1$

$$\hat{x}_j^{lM+m+1} = \frac{\hat{x}_j^{lM+m}}{\sum_{i \in S_m} K_{ij}} \sum_{i \in S_m} K_{ij} \frac{p_i}{\sum_{j'} K_{ij'} \hat{x}_{j'}^{lM+m}}$$

End

Equation 1-17

The OS-EM algorithm is generally M times faster than the ML-EM when using M subsets. Therefore, the reconstruction image using OS-EM with iteration number *n* and subset number *m* is equivalent to ML-EM with iteration number *n*m*. The number of subsets M needs to be chosen carefully to balance the efficiency and accuracy of the algorithm. To avoid confusion, in this dissertation, the word iteration is used for the ML-EM approach, and the word update is used for OS-EM, which is the multiplication of the iteration number and the subset number.

Comparing with the FBP algorithm, statistical iterative algorithms are more advantageous in accurately modeling the system geometry. Scattered coincidence can also be modeled and incorporated into the projection matrix $\boldsymbol{K}$ in the likelihood function of the algorithm. More accurate modeling of the geometrical response leads to higher image resolution and better scatter estimation is crucial to accurate PET image reconstruction. Furthermore, statistical iterative algorithms have better noise properties.

However, compared with FBP approach, some of our studies suggested that statistical iterative approaches for reconstructing noisy data could lead to the quantification bias in small anatomical structures such as the aorta in the vicinity of larger anatomical structures such as the kidneys even after sufficient number of updates.

LISTMODE RECONSTRUCTION

The collected data are usually binned into sinograms, which may involve compression in the axial or radial directions to reduce the data size and improve computation efficiency of image reconstruction. For high resolution PET imaging systems with list-mode data acquisition, this data-mashing can adversely influence image resolution. List-mode reconstruction processes the coincident events one by one and thus is more favorable in many aspects. Also, with the development of PET scanners that records TOF information, list-mode image reconstruction that provide much easier solution to reconstruct the list-mode data and make full use of the TOF information that the conventional sinogram based reconstruction. The ML-EM and OS-EM image reconstruction algorithms have been adapted to list-mode data and have demonstrated improvement in image quality and reconstruction speed [48, 49].

6. MOTION EFFECTS AND 4D IMAGE RECONSTRUCTION

Patient motion causes degradation of image quality and resolution in clinical PET scans. The effects of voluntary patient motions, such as body movement, have been studied extensively and many of them can be reduced by appropriate patient training and correction methods [50]. Involuntary patient motions, mainly respiratory motion (RM) and cardiac motion (CM), and their effects are more difficult to control, and remain active research topics.

CLINICAL RELEVANCE AND SIGNIFICANCE

RESPIRATORY MOTION

RM introduces overall blurring of the cardiac image. Although RM can be controlled and reduced to a some extent by appropriate instructions, it cannot be completely eliminated [51]. The blurring of reconstructed 3D activity distributions itself sometimes can dramatically influence diagnosis, creating false positive or false negative results.

In oncology, lung and liver lesion imaging is crucially important for the detection and treatment evaluation of cancer. A study done by Nehmeh [52] pointed out with unhandled respiratory motion, the activity uptake in small lesions in the lung and liver region were significantly reduce by blurring effects and their finding are shown in Figure 1-12. The reduction of activity uptake not only hindered detection, but it reduced the

quantification value as well, which in return can produce inaccurate results for radiation treatment or evaluating therapy response[53]. In cardiac PET scans, blurring effects caused by respiratory motion in some cases can reduce the activity uptake level in anterior and posterior region, as shown in Figure 1-13, which can be misclassified into myocardium defect, and results in false position diagnosis.

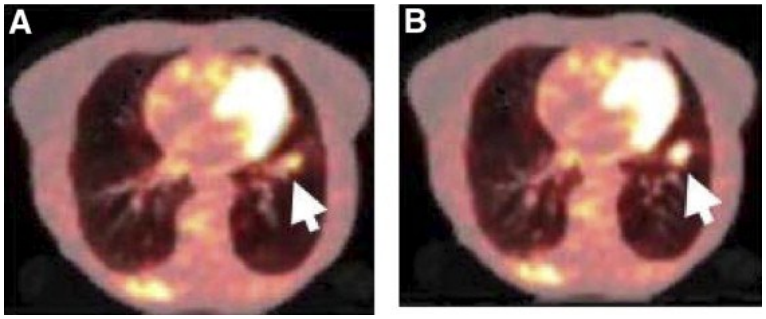

Figure 1-12 Transaxial PET/CT images used for detection of lung lesions [52].
(A) acquisition without respiratory gating with blurring effects, (B) respiratory gated acquisition with reduced respiratory blurring effect. The reduction of activity level by blurring effect can results

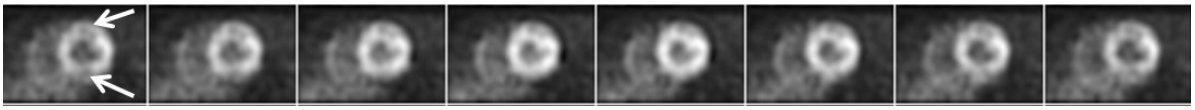

Figure 1-13 Cardiac gated images of short-axis view from a noisy simulation study.
Respiratory blurring effects can be seen in anterior and posterior region (arrow) and results in reduced activity level.

While the blurring effects itself creates problems for diagnosis, the mismatch of activity distribution and attenuation map can also be problematic. As mentioned in the above section "Attenuation", attenuation map is essential to achieve quantitatively correct activity distributions. PET images are obtained in a relatively longer time, the attenuation map produced by a shorter acquisition time of CT or MRI may be in a difference respiratory motion phase with the PET images, resulting in artifacts in attenuation corrected PET images [54]. Similar to the blurring effects, the attenuation-activity mismatch effects could also hinder diagnosis. Figure 1-14 shows the mismatch artifacts from a study carried out by W. Sureshbabu [55]. The mismatch of attenuation and activity map due to respiratory motion resulted in mis-localization of the lesion at the dome of liver. In this case, not only the lesion looks smaller than its actual size, the location of lesion is also misplaced from liver to lung region. For cardiac PET, the mismatch of attenuation and

activity could also result in unmatched lung-heart boundary in activity map and attenuation map, resulting reduced myocardium uptake in anteroapical and anterolateral region as shown in Figure 1-15[56, 57]. The reduction of activity uptake could be mis-identified as myocardium defect and creating false positive results.

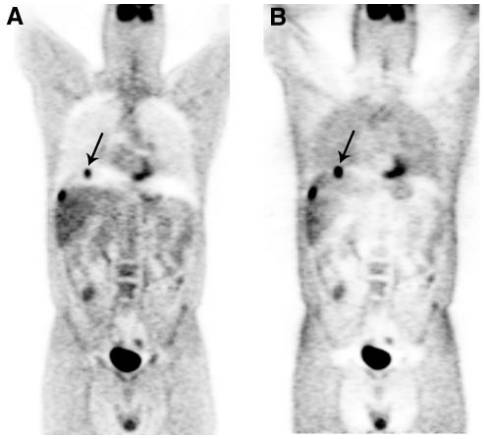

Figure 1-14 Mis-localization of the lesion (arrow) by the attenuation and the activity map mismatch [55]. A) Image with attenuation correction. B) Image without attenuation correction.

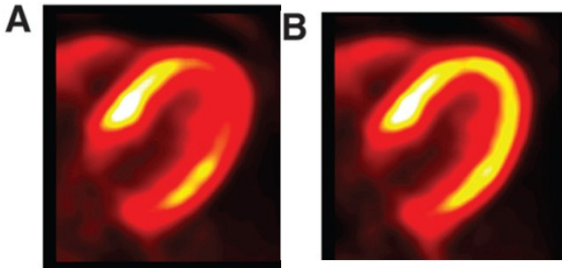

Figure 1-15 Artifacts in myocardium caused by mis-match of attenuation and activity [57]. A) Original image, the reduction of activity levels in anteroapical and anterolateral region can be mis-identified as myocardium defect. B) Images after manual registration of activity and attenuation map. The reduction of activity ware gone.

CARDIAC MOTION

Similar to respiratory motion, cardiac motions degrade image quality by introducing additional motion blurring. The motion blurring itself would also impact the detectability of small lesions such as cardiovascular plaques [58], which are crucially important for early detection of CAD.

As mentioned in section “Introduction to Cardiac PET”, PET can also be used to detect abnormalities in cardiac motion. To acquire cardiac motion information, cardiac gating [59] techniques are required, which will be covered in the next section “Cardiac Gating”. One short comings of doing cardiac gating is the acquired image only contains a fraction of the total counts and therefore it usually takes a long scan for noise suppression.

Unlike respiratory motion, the mis-match effect of attenuation map and activity map introduced by cardiac motion is not significant due to the fact that blood and myocardium have very similar attenuation coefficient.

WHAT HAS BEEN DONE?

In clinical cardiac PET scans, respiratory and cardiac (R&C) gating techniques [60, 61] can be used to reduce motion blurring effects at the expense of low statistics. 4D image reconstruction with motion correction, is a promising approach to reducing motion-blurring effects without lowering the statistics, has been actively investigated by researchers in medical imaging field. By applying 4D image reconstruction with R&C motion correction, the image quality can be improved dramatically, which can also result in reduced dose and scan time. Essentially, 4D PET reconstruction with motion correction is comprised of three inter-related components: gating, motion estimation, and image reconstruction with motion correction.

GATING

RESPIRATORY GATING

Respiratory gating divides the PET dataset into several gates; each one has a different motion phase. In literature, there are two respiratory gating methods: time-based gating and amplitude-based gating [62], amplitude-based gating was shown to be more effective than time-based gating, but it requires the amplitude signal of respiratory motion. Figure 1-16 shows a typical respiratory gating based on the amplitude of breathing motion. The tracking of the amplitude of breathing is a key for respiratory gating [60, 63-65], which is often estimated using external markers or internal organ activity as markers (Data-driven method). One approach of using external markers was implemented by securing a pneumatic

bellows around the chest area of the patient [60], which converted chest expansion to analog voltage signals. Another approach put reflective markers on the patients' abdomen and used a camera to record the movement of the marker [66]. The disadvantages of using external markers include reduction of patient's comforts, increase of hardware cost, requirement of additional scan protocols, and possible mismatch of internal organ movement with external marker movement. Data-driven method with the use of internal organ activity as markers can overcome the above disadvantages. One approach used the heart itself [67]. The center of mass (COM) of the heart was calculated from the listmode data of every 50-ms, and upon further processing, can be used as a surrogate of the breathing motion.

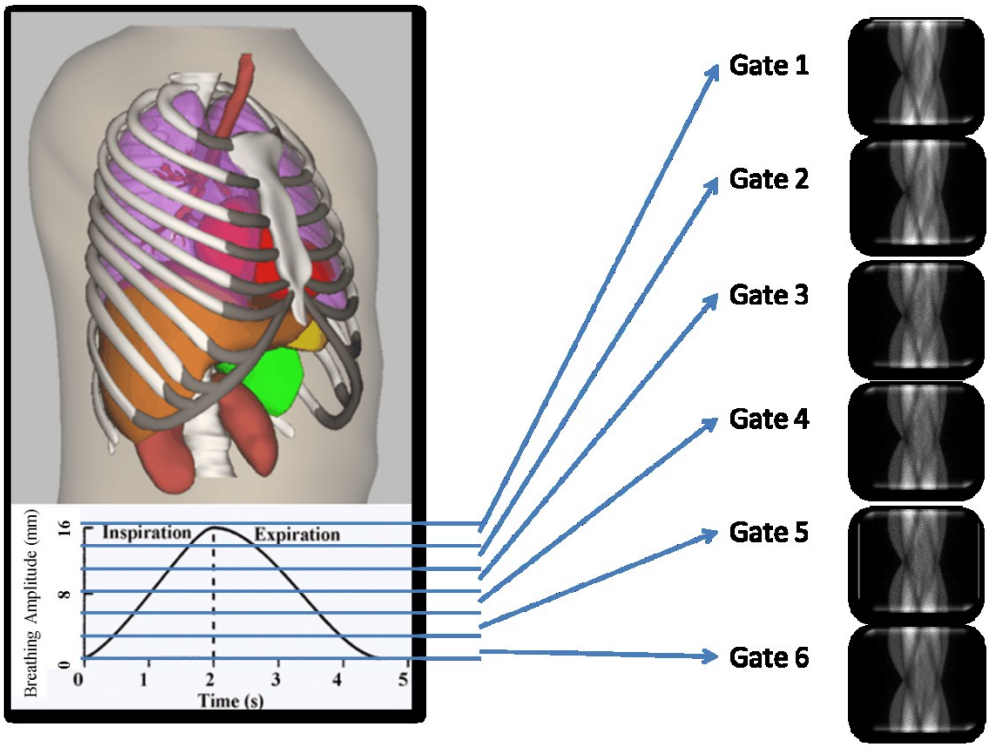

Figure 1-16 Respiratory gating.

CARDIAC GATING

Cardiac gating divides PET data into several (typically 8) time frames based on information of the cardiac motion during the scan. A widely used method is to use electrocardiogram (ECG or EKG) signal recorded together with the PET data as a reference [59]. Electrocardiogram records the electrical activity of the heart,

the electrical impulses generated by the polarization and depolarization of cardiac tissue are translated into a waveform. Figure 1-17 shows an example of a typical ECG signal and the cardiac gating scheme. The R wave of the ECG is used as an indication of the beginning of a cardiac contraction. PET data between two adjacent R peaks are divided into 8 equal-time gates.

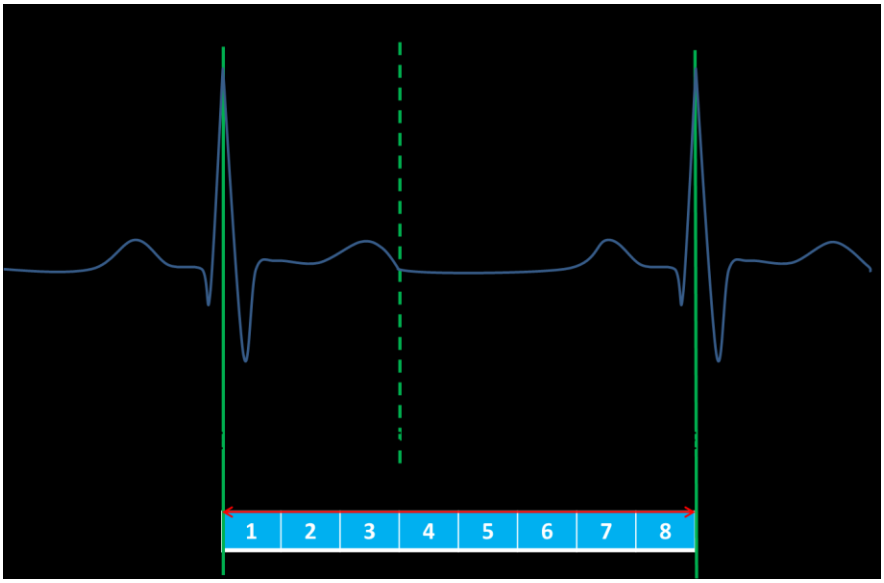

Figure 1-17 ECG wave of a cardiac cycle and cardiac gating.

DUAL RESPIRATORY AND CARDIAC GATING

R&C gating [68] can potentially better resolve finer structure in the myocardium compared with results without R&C gating. Dual gated data are obtained by gating each cardiac gate into different respiratory gates or vice versa. As a result, there will be $F_r \times F_c$ gates in total. F_r and F_c are number of R&C gates respectively. Each gate contains only $\frac{1}{F_r \times F_c}$ of the total counts of the PET scan; therefore, dual R&C gated PET data are usually very noisy. Although the noise level can be reduced by optimum F_r and F_c [69], but this approach is essentially finding a compromise between noise level and motion blurring effects.

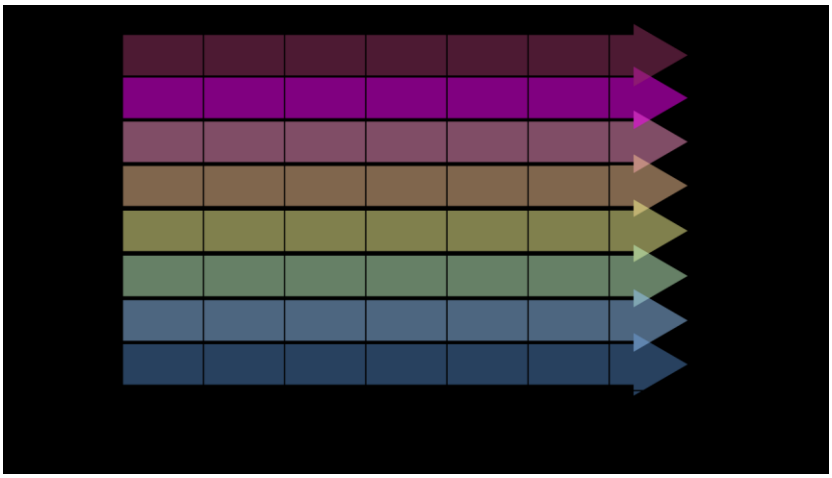

Figure 1-18 Dual respiratory and cardiac gating with 6 respiratory gates and 8 cardiac gates.

MOTION ESTIMATION

The estimation of the non-rigid R&C motion or motion vector field (MVF) is a major challenge. Many related works have been reported in the literature for better MVF estimation. One option for MVF estimation is to use images from other modalities such as CT [70-73] or MRI [74-76]. Respiratory gated CT was used for respiratory motion estimation [70, 72] by applying image registration approaches on the CT reconstructed images. The estimation of cardiac MVF using CT is more challenging due to relatively short period and low soft tissue contrast but can be achieved using ECG gating [71, 73]. The shortcomings of CT based MVF estimation are the extra dose for patient, which is not desirable. Motion estimation using MRI can be more straightforward using MRI tagging techniques together with simultaneous PET/MRI [74]. The disadvantages of using MRI tagging techniques are the relatively long acquisition time (up to ~20 minutes [74]) and the tagging of the myocardium sometimes fades within one cardiac cycle as shown in Figure 1-19, therefore advanced tagging techniques must be developed for cardiac motion estimation. Similar to CT, image based motion estimation methods from MRI images were also developed [77]. Image based motion estimation based on MRI does not require additional dose as that in CT, but it take relatively long time for 4D motion estimation.

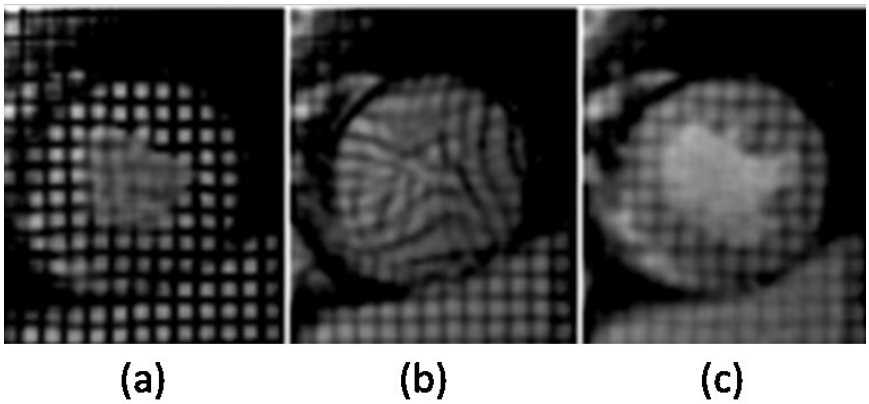

Figure 1-19 Tagged MRI in one cardiac cycle from (a) ED to (b) ES to (c) ED.

On the other hand, MVF estimation using PET data alone has the advantages of more achievable as motion estimation from CT or MRI may not always available, but it suffers from the low count statistics of the PET data, which requires advanced algorithm for motion estimation. In general, PET-based motion estimation can be categorized into three different approaches: motion estimation after reconstruction (MEAR) [78-80], during image reconstruction (MEDR) [81] and before reconstruction (MEBR) [82]. MEAR, with [79] or without activity-preserving [78, 80] image registration constraint, is the most well studied among the others as this approach is essentially image registration problem, and the problem is not too different from other image-based motion estimation methods using CT or MRI. MEAR is more complicated and this method is essentially comparing projection data with image data, therefore were less studied and used. MEBR acquired motion transformation by comparing projection data with projection data before image reconstruction, and current approaches all assume that the motion is rigid.

MOTION CORRECTION

With the estimated motion, methods for PET motion correction could be categorized into three different approaches, i.e., motion correction after, during and before image reconstruction, i.e., the MCAR, MCDR and MCBR approaches.

The general scheme of MCAR is to transform the gated reconstructed images into a reference image to reduce motion-blurring effects, and then sum up the transformed image to obtain a static cardiac image with significantly lower image noise without resolution degradation. By transforming the static cardiac

image using the estimated CM, a 4D gated cardiac image set with significantly improved image quality can also be generated. Gigengack and others [79] used this approach for dual R&C motion correction with activity-preserving motion transform, and observed improved image quality compared with no motion correction. However, in their results, the lack of attenuation correction leads to quantitation error. Traditional attenuation correction methods together without respiratory motion correction may introduce artifacts caused by the mismatch between the PET images which are acquired over all respiratory phases and affected by motion blurring and the CT-based attenuation map which is often acquired in a snap shot with minimal motion effect [54]. A method developed by Chen [83] solved the above problem by applying the estimated respiratory motion to the attenuation map, then applying attenuation correction using the transformed attenuation maps, and eventually correcting both RM and CM after image reconstruction.

MCDR, also known as motion incorporated reconstruction, embeds motion transformation inside traditional iterative image reconstruction methods, e.g., the iterative ML-EM algorithm based methods, to reduce motion-blurring effects while simultaneously generate the motion corrected PET images. Existing motion correction methods mostly focus on either respiratory-only [74, 84] or cardiac-only [81] motion. With the use of conventional image transformation approach, inverse motion transformation was often used within the projection matrix as an approximation of actual transpose motion transformation [72].

MCBR has the inherent advantage of being much faster, and has potential to correct for intra-frame motion. However, most studies that use the MCBR approach only apply a rigid motion model for respiratory motion [82], but the nature of respiratory motion is non-rigid. In order to perform dual R&C MCBR, more advanced theory is required.

WHAT IS REQUIRED?

With the potential of increasing detection accuracy and reduction of patient scan time. 4D image reconstruction with R&C motion correction is becoming increasingly important. While some related works had been done in the literature when we started our project, there are still a lot unresolved questions that need answers. In this section, we will present those issues in three groups: gating, motion estimation, and motion correction.

GATING

For respiratory gating, most unresolved issues are related with the acquisition of respiratory motion signal. Although respiratory motion signal can be acquired external devices, this approach inevitably increases the complexity of the procedure. Moreover, the signal from external device does not necessarily represent the true respiratory motion in the heart as pointed out by some researchers [85]. Data-driven method avoids the above problems but is limited by the presents of noise and signal strength in the listmode data. In a study when the count level in the heart is not high enough, the motion signal information is corrupted by noise and may be inaccurate. Those effects haven't been verified quantitatively and the limitations of data-driven method are never fully studied. In this dissertation, we will quantify the limitation of data-driven method and provide guidelines for applying data-driven method in different clinical cases.

MOTION ESTIMATION

Motion estimation is essential for 4D motion correction in PET. As mentioned in the above section, most related works were focused on the estimation of respiratory MVF only or the estimation of cardiac MVF only. The challenge for dual R&C MVF estimation is the extreme high noise level in dual R&C gated images compared with respiratory or cardiac gated images. While it is possible to apply the same method for R&C motion estimation from dual R&C gated images [79], the impact of image noise on motion estimation accuracy are never fully studied. In this dissertation, we will explore and evaluate more advanced image-based R&C motion estimation methods for better noise handling and accuracy. The results should provide a practical solution for dual R&C motion estimation using PET data with improved accuracy.

The evaluation of motion estimation remains another challenge. Most of existing method used image-based methods to evaluate the accuracy of MVF [78-80], which is by comparing the different images after applying motion transformation using MVF. The disadvantage of the method is not only that MVF were evaluated indirectly, but also the results are significantly influenced by image quality. In other words, image-based MVF evaluation methods have trouble distinguishing between the difference caused by image

noise and the difference caused by motion. Therefore, additional studies are required for better evaluation of the MVF and also to evaluate the image-based evaluation methods themselves.

MEDR has been shown to have better accuracy than MEAR in theory, but more work is required for comparison with MEAR in realistic dataset with realistic human anatomies. MEBR potentially can be very fast but is rarely studied and most of existing studies are based on rigid motion assumption and are for respiratory motion only [82], while the true respiratory motion is 3D in nature and cardiac motion cannot be simplified using rigid motion model. In this study, we will also address the above issues by developing and evaluating MEDR and MEBR methods.

MOTION CORRECTION

Similar to motion estimation, most work on motion correction methods are done on respiratory motion only or cardiac motion only. While dual R&C MCAR was already achieve in our previous work [83] and in literature [79], with iterative image reconstruction being non-linear, the individual reconstruction for each dual R&C gated frame can be problematic and may result in undesirable image bias, which could be more severe with reduce counts. As one of the potential benefit of 4D image reconstruction with motion correction is to reduce scan time or dose, the situations with low counts are going to be common. MCDR provides a solution for better noise handling properties as with the modeling of motion the whole dataset is reconstructed at once, but most studies were focused on either respiratory or cardiac motion. The application for dual R&C motion correction is required and a through comparison of MCAR and MCDR in the dual R&C motion case is also needed.

The currently widely used non-activity-preserving (NAP) motion transformation scheme does not guarantee the conservation of counts, which makes it another unresolved problem in this area. In this dissertation, we will implement activity-preserving (AP) motion transformation process and evaluate the difference and impact of AP and NAP transformation on the quantitation of PET images.

Using conventional interpolation scheme for motion transformation, the transpose motion transform operation step in MCDR cannot be implemented accurately without further modification and approximation. In literature, inverse motion transform were often used as an approximation as the actual

transpose motion transformation [72].The effects of the approximation were never fully studied and the exact implementation for MCDR is required. In this dissertation, we will propose a new interpolation scheme that allows the exact implementation of MCDR and compare with the approximations used in literature.

While MCAR and MCDR work in theory, the dramatic decrease in calculation speed prevents them being used in practical case. As with 48 dual R&C gates, the required calculation time for MCAR and MCDR increase by at least 48 times. One solution to this problem is to apply motion correction on the projection data, i.e. MCBR. In theory, while MCAR and MCDR require 48 reconstructions for 48 gates, MCBR only requires one reconstruction in theory regardless of number of gates. As mentioned above, current MCBR methods [82] are only based on rigid motion model, which may be proper for approximating respiratory motion but not for modeling cardiac motion. Non-rigid MCBR was never proposed nor explored in the literature before. Therefore, in this dissertation, we will present a new theory and practical implementation of MCBR with non-rigid motion model that can model both R&C motion that can truly speed up motion correction process. With the newly developed MCDR and MCBR, we will evaluate and compare the performance of each method with the existing MCAR, and the results should also provide general guidelines for different applications that have different requirement.

7. CONTRIBUTIONS OF THIS DISSERTATION

In this dissertation, we have made original and major contributions to the theory, implementation and evaluation of 4D image reconstruction methods with R&C motion correction for cardiac PET imaging. As mentioned in previous section “Motion Effects and 4D Image Reconstruction”, respiratory motion cause resolution loss; cardiac gating produce a set of cine frames of the beating heart for better visualization of the cardiac motion but are affected by increased image noise. Our contributions address major difficulties encountered by conventional 4D images reconstruction methods and provide comprehensive comparison of conventional and our proposed implementation methods. They demonstrated the significant improvement in 4D cardiac PET image quality in terms of much reduce image resolution loss due to respiratory motion and much reduced image noise in the cine beating heart images. The improvements can potentially improve clinical diagnosis, such as detecting cardiac motion abnormalities and heart diseases. The improved image

quality can be traded for reduced injected radiation dose to the patient or reduced imaging time for improving patient comfort.

Specifically, our major contribution can be divided into three areas. They correspond to the three major steps in the 4D image reconstruction with respiratory and cardiac motion correction: 4D data acquisition/gating, 4D motion/MVF estimation, and 4D motion correction.

For the first step, we focused on improving the respiratory gating in 4D data acquisition. On one hand, we proposed quantitative criteria to test the limitations of the existing PET-based data driven method and MR-navigator gating using clinical data. On the other hand, we developed an improved data driven method to extract the respiratory motion signal with higher accuracy. This method is able to detect weak respiratory motion from the projection data that cannot be extracted using conventional method. Based on the performance of different methods for patient data of various activity uptake and noise level, we also provided guidelines for methods selection in clinical practice.

For the second step, we developed new methods for each of the three types of motion estimation techniques: motion estimation before, during and after image reconstruction (MEBR, MEDR, and MEAR). We evaluated all the methods qualitatively and quantitatively using realistic simulation data. Our methods provide higher accuracy in motion estimation compared with existing approaches and show strong advantage in handling clinical data with current or even increased noise levels.

The major contribution of the dissertation is the third step. It is the first time that 4D R&C motion correction techniques has been thoroughly discussed and evaluated using both realistic simulation data and clinical data. We studied three types of methods: MCBR, MCDR, and MCAR. Although MCAR and MCDR were proposed in literature, approximations were used for implementing MCDR. In this dissertation we proposed and evaluated the exact implementation of MCDR for dual R&C motion correction, which was not present in literature. The comparison also suggested that MCDR with exact implementation achieve the highest quantitative accuracy. Motion correction using either MCAR or MCDR requires tremendous amount of time, which is impractical for clinical use. We also proposed and evaluated a completely new non-rigid MCBR method, which corrects for motion on the projection data and

theoretically much faster than the other two methods. The MCBR achieved higher quantitative accuracy than MCAR in high noise situations, which makes it even more promising for practical use.

Besides the new methods, our contribution also includes the generation of a whole set of 4D almost-noise-free Monte Carlo simulation data, using the 4D XCAT phantom, Monte Carlo simulation tools including SimSET [86] and GATE [87]. This data set provides realistic simulation of a commercial PET scanner and can be used to generate PET data with arbitrary organ uptake.

8. ORGNIZATION OF THIS DISSERTATION

In the following dissertation, we will present our work in the following four chapters after Chapter 1, which are “Chapter 2. Methods and Materials”, “Chapter 3. Result”, “Chapter 4. Conclusions”, and “Chapter 5. Future Work”. In each chapter, we will also present our work in three sub-sections: 4D data generation/gating techniques, motion or MVF estimation techniques, and motion correction techniques.

In gating techniques, we will focus on improving data-driven method and test its performance regarding myocardium uptake ratio noise level; we will also compare data-driven method with MRI-based gating methods to further test the feasibility for both methods.

In motion estimation techniques, we will focus on PET-data based motion estimation methods, which are motion estimation after (MEAR), during (MEDR), before (MEBR) reconstruction. Advanced methods for better noise handling will be developed and MVF-based motion evaluation will be used for accurate quantification of motion estimation accuracy. We will also explore possible MRI-based motion estimation as simultaneous PET/MRI is becoming increasingly available at the moment.

In motion correction techniques, we will focus on the development and evaluation of three non-rigid dual R&C motion correction approaches: MCAR, MCDR and MCBR. Detailed study such as the comparison of using activity-preserving and non-preserving, the effects of inverse approximations in the MCDR, and the performance of three approaches at different noise levels are studied. This study should provide a general guideline for choosing motion correction approaches for different image scenarios.

CHAPTER 2. METHODS AND MATERIALS

4D dual R&C motion compensation for cardiac PET data consists of three steps. The first step is generation of respiratory and cardiac gated PET data. For clinical patient studies, listmode PET data with ECG signal and external respiratory motion measurement equipment is acquired for dual R&C gating. For simulation study, dual R&C gating is achieved by generating digital phantom of different cardiac and respiratory phases. The second step is to obtain motion information required in motion correction. The respiratory and cardiac motion is obtained either from images reconstructed with PET data or based on information provided by other imaging modalities such as MRI. The third step is to apply the motion estimated in the second step to the gated data to reduce the motion blurring and improve image statistics in the final cardiac PET images. There are multiple approaches for each step. In this dissertation, new methods were developed for each step; evaluation of proposed methods and comparison with existing methods were carried out using both simulation data and clinical patient data. The general structure for both 4D motion correction and the organization of this chapter is shown in Figure 2-1.

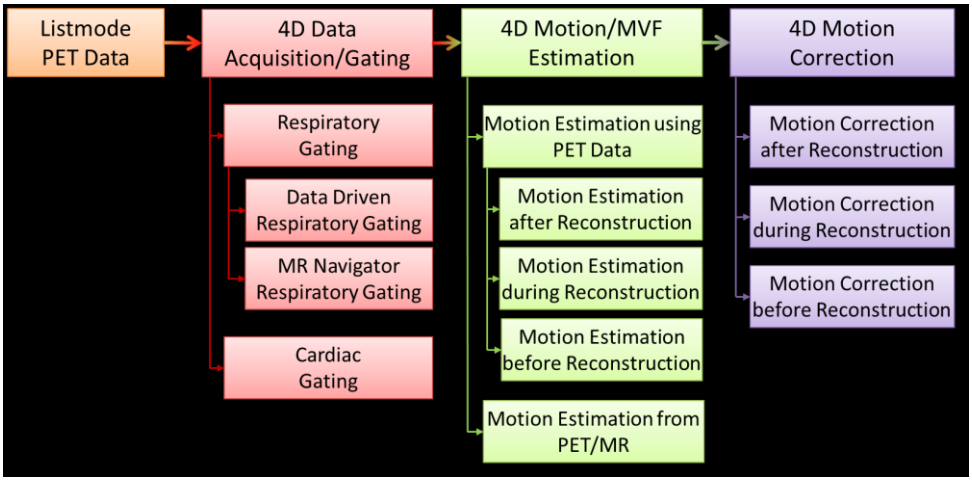

Figure 2-1 General scheme for 4D image reconstruction with R&C motion correction.

1. SIMULATION AND PATIENT DATA

INTRODUCTION TO SIMULATION TOOLS

Monte Carlo simulation is a numerical calculation method to solve mathematical problems based on random variable sampling. Monte Carlo simulation has been playing an important role in nuclear medicine such as SPECT and PET for designing new medical imaging devices, optimizing acquisition protocols, and developing and evaluating image reconstruction algorithms and correction techniques. This study employed two Monte Carlo simulation tools to generate noise-free data from the phantom. The integration of the SimSET and GATE in PET simulation with 4D NURBS-based Cardiac-Torso (XCAT) phantom (Figure 2-2) has been validated [88] and proven capable of speedup the generation of noise-free data.

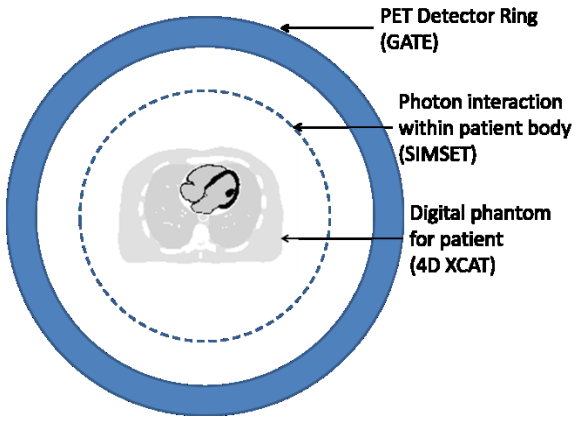

Figure 2-2 Illustration of the combination of GATE, SIMSET and 4D XCAT.

GATE

The Geant4 Application for Tomographic Emission (GATE) [87] is a Monte Carlo simulation tool developed by the OpenGATE collaboration for numerical simulations in nuclear medicine. Built upon GEANT4, it provides intuitive, versatile, and convenient modeling of complex system geometry through a user-friendly interface, as well as capability of modeling time-dependent processes such as radioactive decay. Its main strength is intuitive implementation of complex system configurations as well as comprehensive simulations for the collimator/detector components. However, it is relatively slow in simulating photon interactions and transport inside voxelized phantoms.

SIMSET

The SimSET software developed by University of Washington [86] models the physical processes and instrumentation used in emission tomography with Monte Carlo techniques. The core module of the software is the Photon History Generator (PHG) that simulates the radioactive decay and the resulting photon paths through the phantom one by one. Random coincidence is simulated by the random coincidences generation module. Collimator and detector are simulated in the collimator module and the detector module respectively. In our study, the output of PHG was set as an input of the GATE,

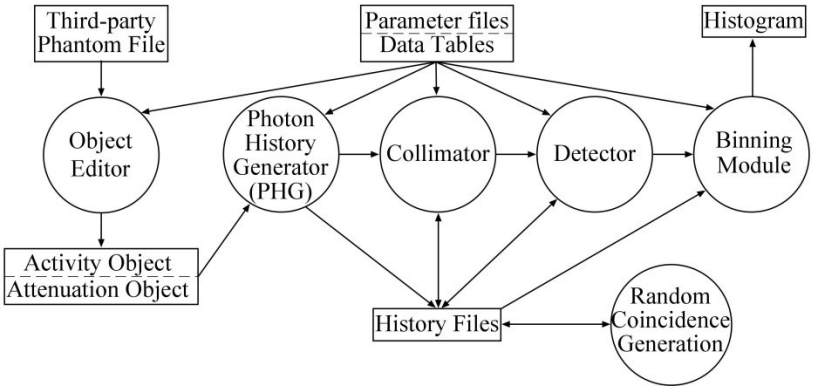

Figure 2-3 Block diagram of the modules in the SimSET software.

4D XCAT

In this study, the 4-D XCAT phantom [89] featuring a 4-D beating heart model with known cardiac MVF was employed to simulate myocardial perfusion (MP) PET images for implementation and evaluation of the proposed motion compensation method. As a digital anthropomorphic phantom widely used in nuclear medical imaging study, the 4-D XCAT phantom provides both realistic activity and attenuation maps of the human body and allows for simulation of medical image data with known medical imaging processes. The shapes of the organs in the XCAT were modeled with non-uniform rational b-splines (NURBS) surfaces based on a 3-D cardiac-gated CT image dataset. The 4-D cardiac MVF of the original XCAT phantom was determined from a set of 4-D tagged MRI cardiac images, and the respiratory motion came from a 4-D high resolution respiratory-gated CT dataset. The ability to provide realistic, predictive 3D and 4D imaging data for both normal and abnormal patients makes the XCAT phantom an ideal tool to study the performance of imaging devices and techniques.

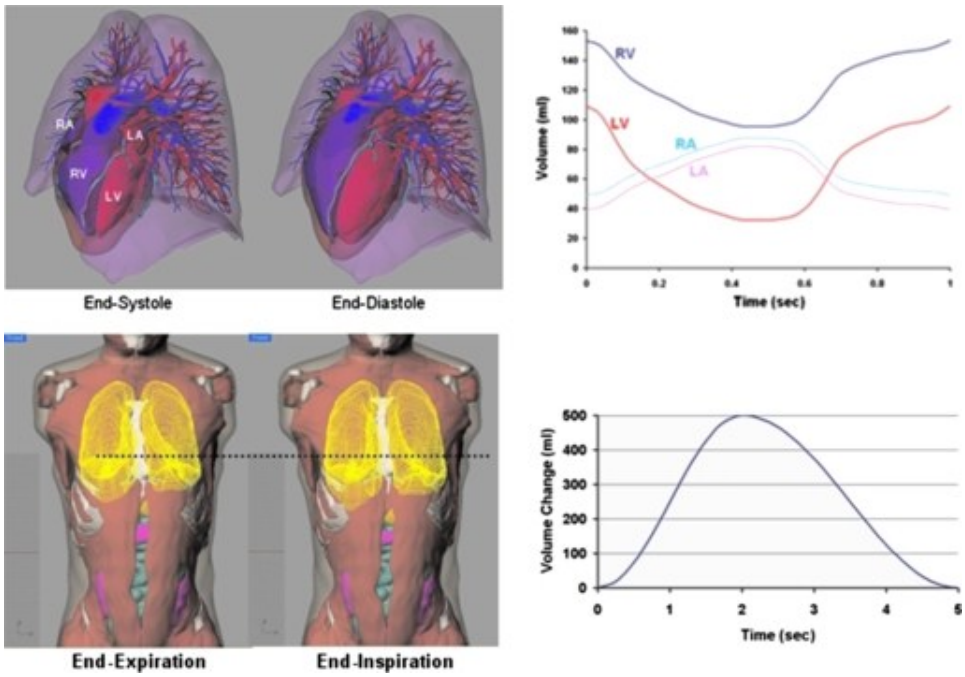

Figure 2-4. 4D XCAT phantom with cardiac (top) and respiratory (down) motions.

REALISTIC MONTE CARLO SIMULATION

Realistic Monte Carlo simulation modeling the GE discovery RX scanner was done with GATE and SIMSET software, as the combination of both was shown to yield faster speed [88]. The 4D XCAT phantom [89] with realistic R&C motion was employed to generate raw data for simulation of cardiac PET scan. Scatter events was also stored for accurate scatter correction purpose.

Almost noise free data were generated and later used for the study of different scan times by adding Poisson noise. Organs including myocardium, blood pool in the heart, spleen, lung, stomach, liver, and the rest of the body were simulated individually. The simulation of separate organs allows creation of any tracer uptake by summing organ projections with different weight, as shown in Figure 2-5. In this study a typical FDG tracer uptake was simulated. The projection data in Figure 2-5 is scaled to isotropic voxel resolution from the original simulation (2.13mm/pixel in horizontal axis and 6.54mm/pixel in vertical axis) for illustration purpose.

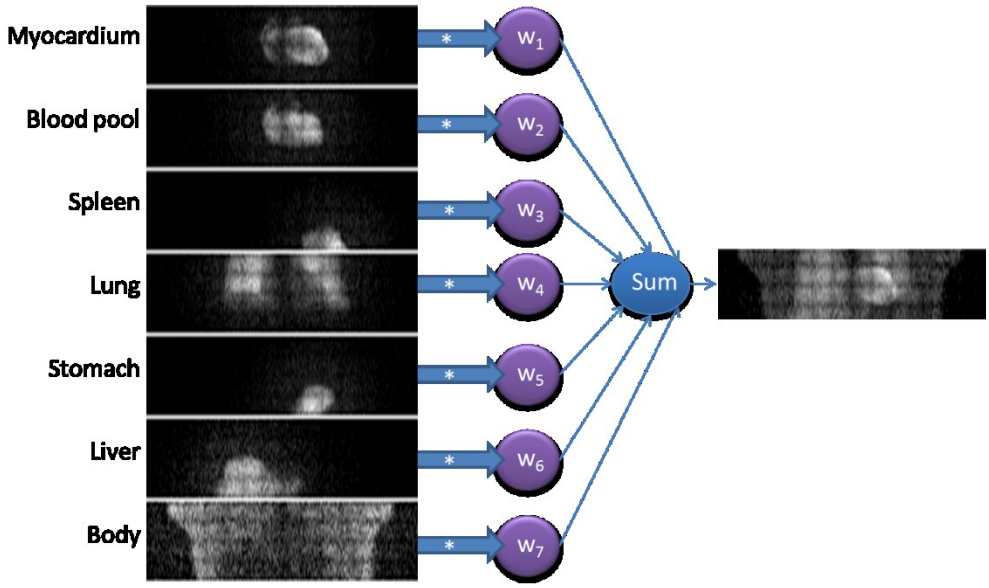

Figure 2-5 Illustration of the simulation for FDG tracer uptake from individual organ uptakes.

The dark strip in Figure 2-5 as well as Figure 2-6a was caused by non-uniformity in the detectors and detector gaps based on realistic configuration of the GE RX PET scanner. To correct for this effect, a detector coefficient map was obtained from a separate simulation using a digital cylinder phantom (Figure 2-6b).The uniformity map (Figure 2-6c) was calculated by dividing the theoretically calculated sinogram of the cylinder phantom considering only attenuation effect with the Monte-Carlo simulated sinogram.

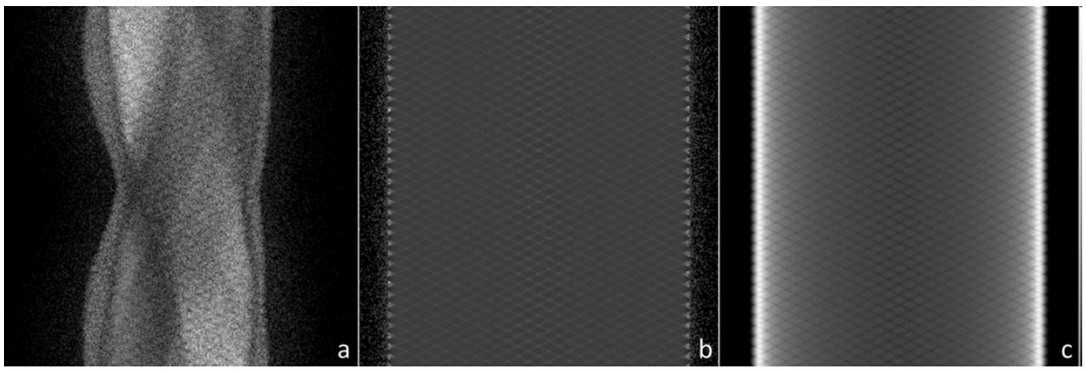

Figure 2-6 Effects of detector non-uniformity and uniformity correction.

a) simulated sinogram of the 4D XCAT phantom before uniformity correction, b) simulated sinogram of the digital cylinder phantom, c) uniformity map.

A combination of 24 equal-time respiratory gates and 48 equal-time cardiac gates with total of 1152 gates were generated. To save simulation time, projections of 1152 dual R&C gates were simulated only for the myocardium and blood pool shown in Figure 2-5. For the rest organs, projections of only 24 respiratory gates were simulated as we assume that the cardiac motion did not affect organs other than the heart. In this case a total of 2424 (1152*2+24*5) projections were simulated. Different levels of Poisson noise were added on the simulated projection data as well for evaluation purpose.

ACQUISITION OF PATIENT DATA

Eleven patients injected with ~10 mCi ^{18}F-FDG and scanned for 4 to 14 minutes on a simultaneous PET/MRI scanner (Siemens Biograph mMRI) were used in this study Information of the patients is provided in Table 2-1. Listmode data with only electrocardiogram signal was acquired. Most of the patient scans showed higher noise levels than that of a typical cardiac PET scan as them were acquired ~2 hours after injection while a typical cardiac scan is usually acquired ~1 hour after injection. The decay of ^{18}F due to the delayed scan starting time resulted in poor statistics in some of the patient data. Since the scan starting time is different for the patients, the scan duration was not a good indicator of the noise level. Instead, total counts was used for quantifying the noise level in the patient data, where the total counts was measured as the counts in the middle slices across the myocardium region (Figure 2-7a) summed for all angles, segments and gates, and normalized by slice thickness (5.2 mm between adjacent detector rings).

Table 2-1 List of Patient data used in this study.

Patient ID	MRI-Navigator	MRI-Respiratory Motion	MRI-Cardiac Motion	Total counts (1/mm)	Total Scan Time (min)
M005	**Yes**	No	No	77k	9.0
V002	**Yes**	No	No	56k	6.3
P030	**Yes**	No	No	30k	6.6
M024	**Yes**	No	No	18k	13.6

M014	**Yes**	**Yes**	No	55k	11.2
P008	**Yes**	No	No	45k	6.1
P053	**Yes**	No	No	44k	6.9
P055	**Yes**	No	No	45k	4.5
M007	**Yes**	No	No	20k	10.8
P057	**Yes**	**Yes**	No	46k	5.5
V001	No	No	No	243k	12.0

As some of the patient data was used for study of plaque imaging, the uptakes of the myocardium were suppressed in those cases. To quantify the myocardium uptakes, sinogram contrast for each patient data was measured using the following method as shown in Figure 2-7:

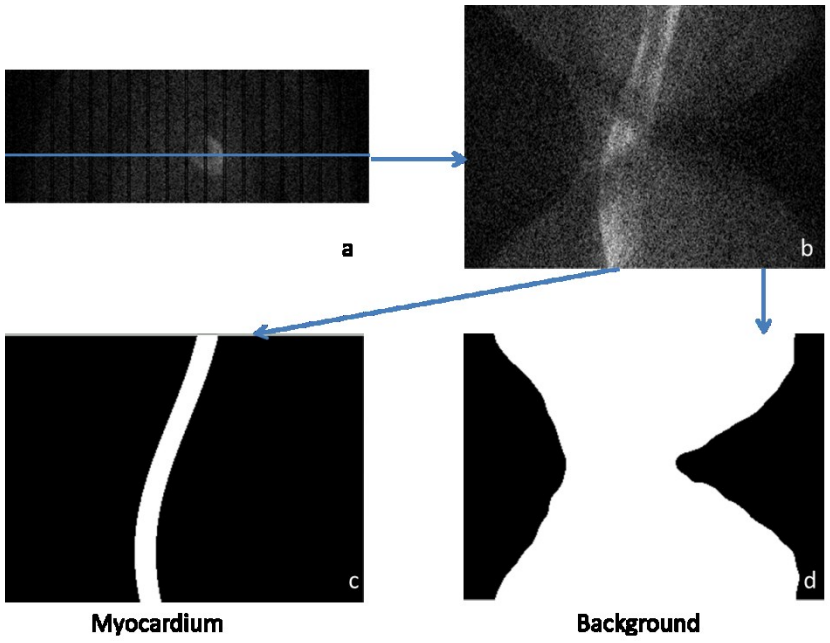

Figure 2-7 Illustration for the calculation of sinogram contrast.

For each patient data, the slice that across the center of myocardium region in the 3D projection data was chosen (Figure 2-7a) and the resulting 2D sinogram is shown in Figure 2-7b. Two separate masks were created on the 2D sinogram. The first one (Figure 2-7c) is the projection of the myocardium region defined by a circle with a diameter equal to average heart size. The second mask (Figure 2-7d) is the background

region, which contains the counts from all over the patient body including the heart. The sinogram contrast is defined using Equation 2-1:

$$Sinogram\ Contrast = \frac{Average\ counts\ in\ myocardium\ region}{Average\ counts\ in\ background\ region}$$

Equation 2-1

2. GATING TECHNIQUES

Dual R&C gating is inherent in the simulation study through phantom image generation. For the clinical patient data, the following approaches were implemented to the listmode PET data for dual R&C gating.

DATA-DRIVEN RESPIRATORY GATING

Without the need of using external devices, PET-based data-driven respiratory amplitude-gating approach [67] extracts the information contained in the listmode data to identify the respiratory status of the patient for respiratory gating. The data-driven approach measures the location of COM of the total activity distribution the field of view along the vertical axis (z axis) from the listmode data in every fixed time interval Δt as shown in Equation 2-2, where $e(a, b, z, t)$ represent each co-incident event detected at time t, a is the angle of the LOR in horizontal plane, b is the detector bin number, and z is the center location of the LOR along the vertical axis. Based on clinical data, the breathing interval for human is usually around 5 seconds but can be as fast as 2 seconds. To get reasonable number of samples to fully capture the respiratory signal, the sampling interval between two COM calculations should be shorter than 500 ms. With sampling interval shorter than 500 ms, the contribution of quantum noise in each measurement can be very high. Additional smoothing must be applied to reduce the effects of noise. For some patient study, the measurement of COM contains cardiac beating signal as well, indicating the prospective feasibility of this data-driven approach in cardiac gating.

$$COM(n) = \frac{\int_{t=n\Delta t}^{t=(n+1)\Delta t} \int_{v=FOV} z * e(a, b, z, t) dv\, dt}{\int_{t=n\Delta t}^{t=(n+1)\Delta t} \int_{v=FOV} e(a, b, z, t) dv\, dt}.$$

Equation 2-2

Figure 2-8 shows the Fourier transform of a typical COM signal. For this specific case, the spectrum contains both respiratory motion peaks and cardiac peaks. To reduce noise level and eliminate the effects of cardiac signal in our measured data, a low pass filter that essentially reduced the high frequency background noise and removed cardiac signal was applied on the signal. The red dashed rectangle that contains cardiac peaks and high frequency components is removed by the low pass filter.

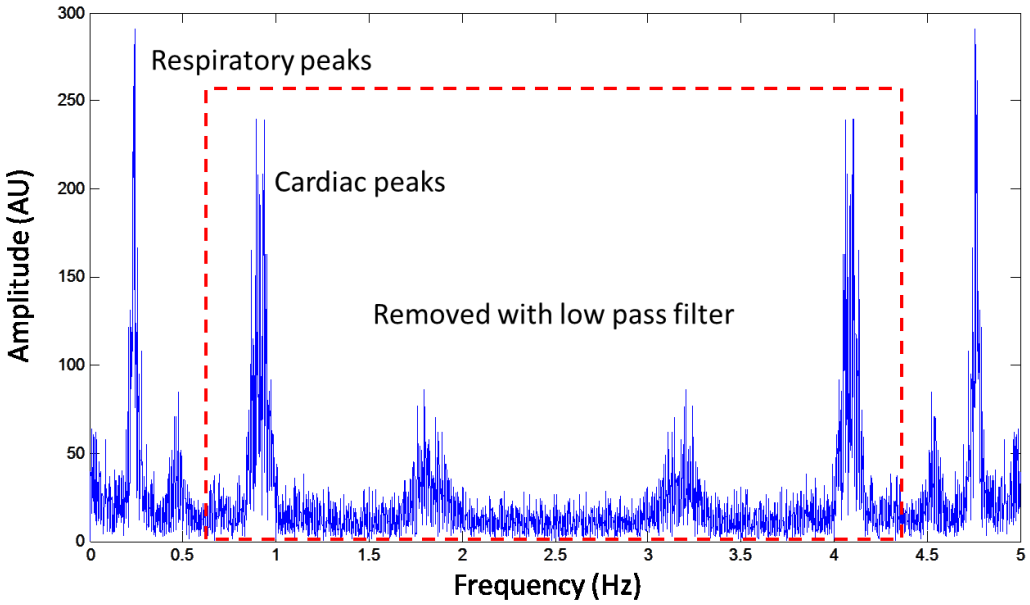

Figure 2-8 Typical look of measured center-of-mass signal in frequency domain.

High frequency noise and cardiac motion was removed by using low pass filter.

In some of our patient data, conventional data-driven methods failed as the noise level in the patient listmode data goes to high. No "respiratory peak" was visible in its Fourier domain. The method was modified to improve the respiratory motion signal extraction. In this new method, a mask that covers only the myocardium region was placed in the projection data to as shown in Figure 2-9, and only listmode events from within the mask were used for calculating COM, as shown in Equation 2-3.

$$COM(n) = \frac{\int_{t=n\Delta t}^{t=(n+1)\Delta t} \int_{v=Myocardium} z * e(a,b,z,t) dv\, dt}{\int_{t=n\Delta t}^{t=(n+1)\Delta t} \int_{v=Myocardium} e(a,b,z,t) dv\, dt}.$$

Equation 2-3

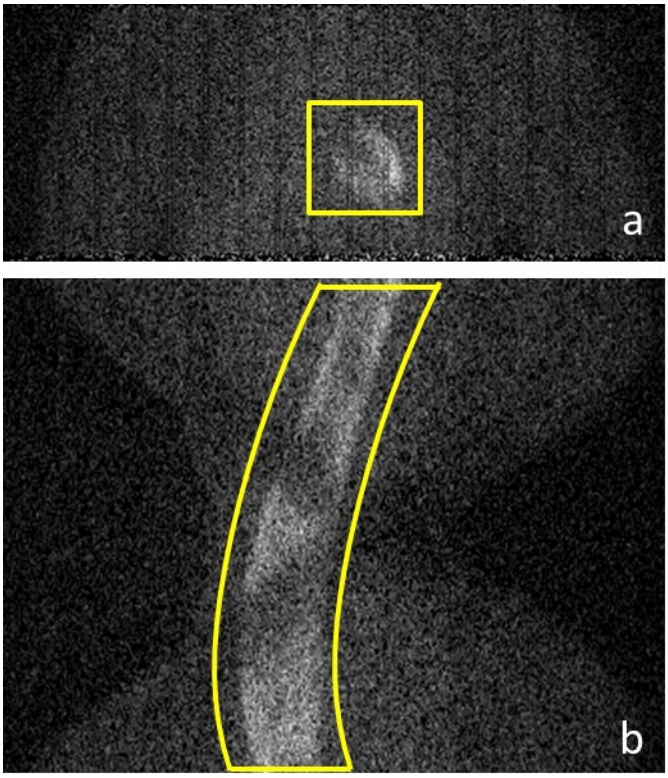

Figure 2-9 Mask used for calculating center-of-mass.

a) Mask in projection view (*b*-*z* plane). b) Mask in sinogram view (*b*-*a* plane).

Based on the amplitude of COM signal, the PET data is divided into 6 respiratory gates. There are two ways for amplitude-based respiratory gating: equal amplitude (Figure 2-10) and equal counts (Figure 2-11). The advantage for equal amplitude gating is that the respiratory motion is evenly distributed among different gates, resulting in theoretically small and equal intra-frame motion within each gate. However, with different total counts in each gate, the noise level in each reconstructed gated image can be quite different and could affect the accuracy of motion estimation based on those images. Therefore, equal-counts amplitude-based respiratory gating was used in this work.

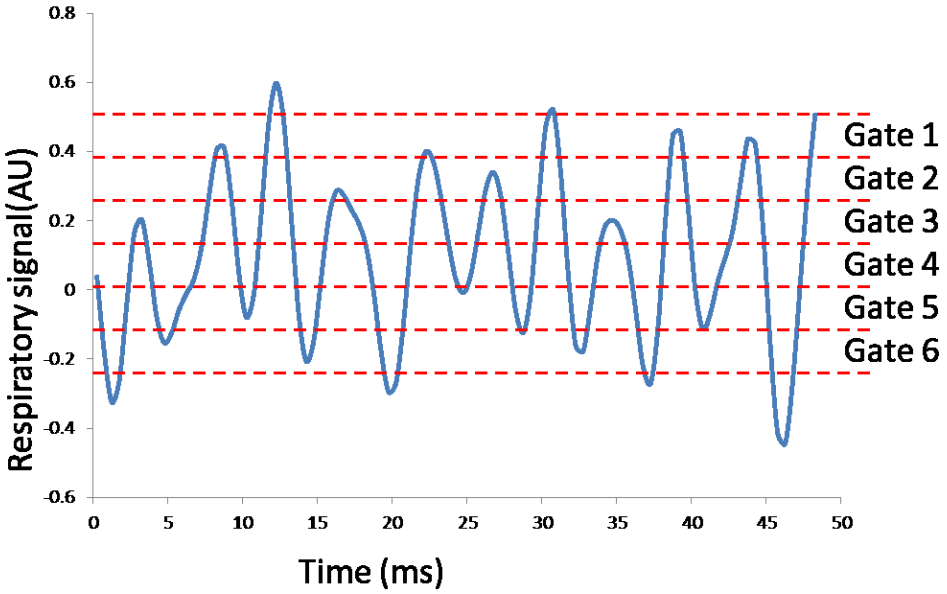

Figure 2-10 The scheme for equal amplitude amplitude-gating.

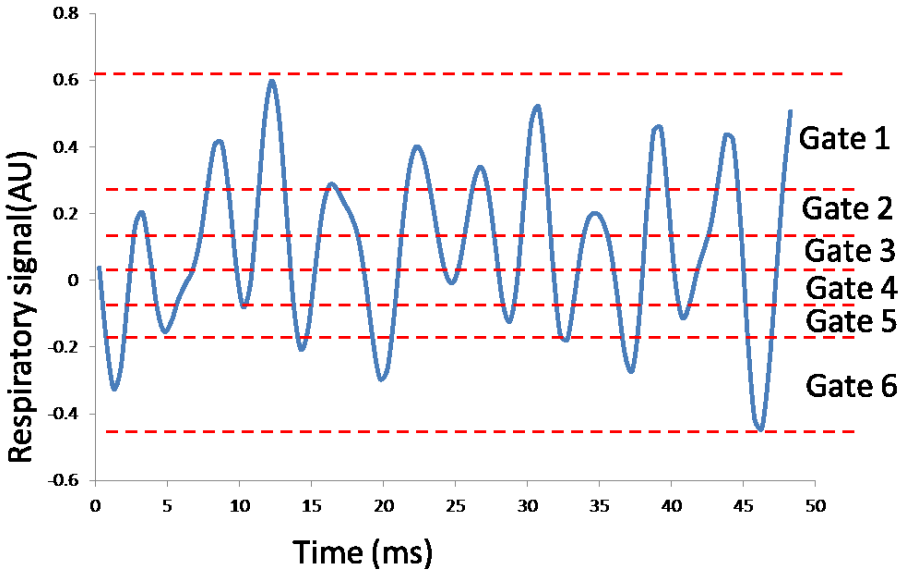

Figure 2-11 The scheme for equal counts amplitude-gating.

Even with improved data-driven method, the detection of respiratory signal still failed when the patient data is extremely noisy or has suppressed myocardium uptakes. In these cases, MRI navigator based respiratory gating was used instead.

MRI NAVIGATOR DRIVEN RESPIRATORY GATING

With the help of simultaneous PET/MRI, MRI navigator could be used for amplitude-based respiratory gating [85], which is commonly used in MRI gated acquisitions [90]. The MRI navigator is a pencil-beam placed on the right diaphragm that measures the one dimensional image alone the axial direction. The sampling rate of navigator measurement is around every 800 ms. Figure 2-12 shows a sample navigator image, which is a stack of 1D image over time (horizontal axis). The lighter part is the liver and the darker part is the lung. Respiratory signal was measured by tracking the boundaries between lung and liver over time. Using the measured signal from the MRI navigator as reference, amplitude-based respiratory gating was implemented on the PET data as described in the last section.

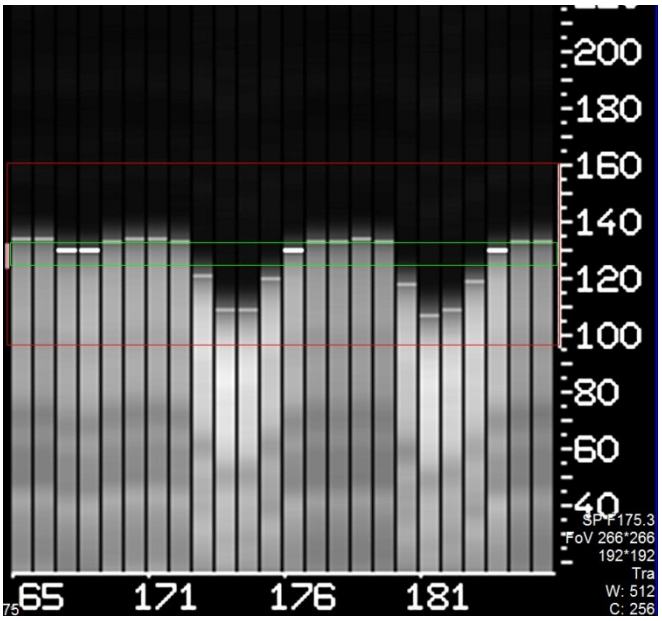

Figure 2-12 Sample image of the 1D navigator over time.

ECG GUIDED CARDIAC GATING

ECG signal was embedded in listmode acquisitions, and was used for cardiac gating. This method is descripted in section Cardiac Gating in Introduction.

3. MOTION ESTIMATION TECHNIQUES

The second step for dual R&C motion correction on 4D PET data is to get accurate motion information from the reconstructed images of gated PET data. Several sophisticated algorithms were developed to complete this task.

MOTION ESTIMATION BASED ON PET DATA

MOTION ESTIMATION AFTER IMAGE RECONSTRUCTION (MEAR)

The estimation of patient motion based on reconstructed PET images, or motion estimation after image reconstruction is essentially image registration problem, which is the estimation of displacement vector field or motion vector field between reconstructed images of different gates. The challenges lie in the poor image resolution and high quantum noise. Unlike other image registration problems, the spatial resolution of the motion vector field for patient motion is limited thanks to physiological factors, suggesting it is possible to use low-resolution PET image to estimate patient motion.

To reduce the effect of noise, the following two approaches were used in our motion estimation methods. 1) Additional smoothing filter was applied on the PET images prior to image registration. 2) Control points based motion estimation was used instead of voxel based motion estimation. In both cases, the effect of noise was reduced by further lowering the resolution of estimated MVF.

The B-spline group-wise based image registration [91] was used for MEAR based on reconstructed PET images, in which case, the MVF that transformed each image into the reference image was estimated using Equation 2-4:

$$\left\{\widehat{\vec{T}}_g(\vec{r}), g = 1, 2, \dots, G\right\} = \operatorname{argmin} \sum_{g_2 \neq g_1}^{G} \sum_{g_1=1}^{G} \iiint_{\Omega} \left[f_{g_1}\left(\vec{T}_{g_1}(\vec{r})\right) - f_{g_2}\left(\vec{T}_{g_2}(\vec{r})\right)\right]^2 dxdydz,$$

Equation 2-4

where $\widehat{\vec{T}}_g(\vec{r})$ represents the estimated voxel based MVF, which is also a function of control points. g stands for different gate number from 1 to G. The MVF transforms each gated image into the reference image which is chosen so that the difference among motion transformed images is minimized. As shown in Figure

2-13, Voxel base MVF (blue vectors) is derived from control-point based MVF (red vectors) using B-spline interpolation.

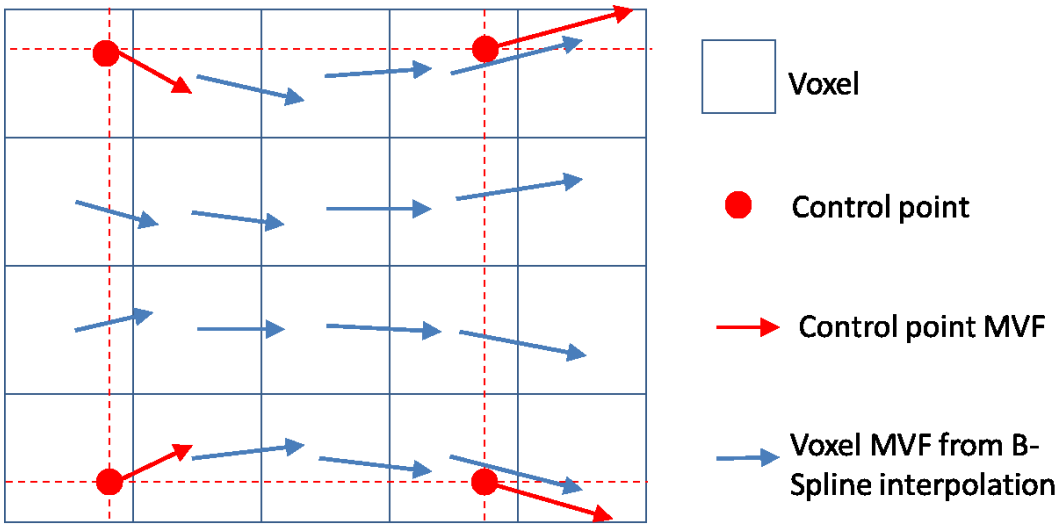

Figure 2-13 Illustration of the calculation of voxel-based MVF from control-point based MVF using B-Spline interpolation.

RESPIRATORY MOTION ESTIMATION

Respiratory motion estimation was done by directly implement the above approach on the reconstructed respiratory gated PET images. In cases where only one attenuation map is acquired along with PET data, previous study [92] suggested that motion estimation using images without attenuation correction outperforms motion estimation using attenuation corrected images, as later approach may introduce activity-attenuation mismatch. Cardiac motion was ignored when estimating respiratory motion as the high spatial frequency component of respiratory motion tends to be small and resulting smaller change for adjacent regions in the myocardium.

DUAL RESPIRATORY AND CARDIAC MOTION ESTIMATION

The challenge of estimating dual R&C motion based on PET images lie in the extremely high noise in the dual gated PET reconstructed images. Since the respiratory motion and cardiac motion of human body happen simultaneously in different pattern and frequency, it is impossible to completely separate these two

motion components in cardiac PET images. To minimize the mutual interference of respiratory and cardiac motion, four different methods were developed for estimating dual R&C motion:

Method 1: Direct motion estimation from dual R&C gated images.

This is the most straight-forward approach [79], in which case, respiratory frame 1 and cardiac frame 1 was chosen as the reference image, and the rest 47 images were registered to the reference image using Equation 2-4. As our region of interest is the myocardium region, a 3D mask was chosen to only register images intensities within the mask shown in Figure 2-14.

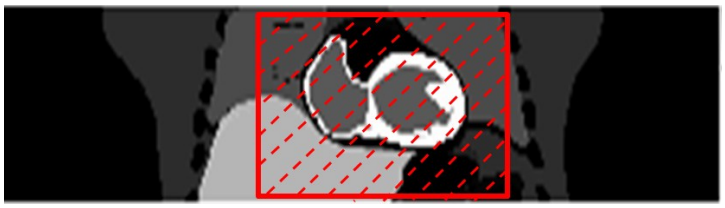

Figure 2-14 Image mask used for registration.

Method 2: Three-step approach

In this approach, respiratory motion and cardiac motion were estimated separately under the assumption that respiratory motion and cardiac motion are independent. The three steps are (Figure 2-15):

A) Estimation of respiratory motion based on respiratory gated reconstructed images

B) Estimated of cardiac motion based on cardiac gated images

C) Combine estimated respiratory motion and cardiac motion into dual R&C motion

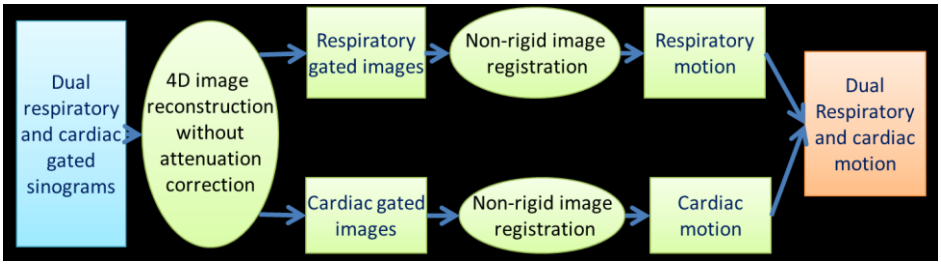

Figure 2-15 The flowchart for three-step dual respiratory and cardiac MEAR.

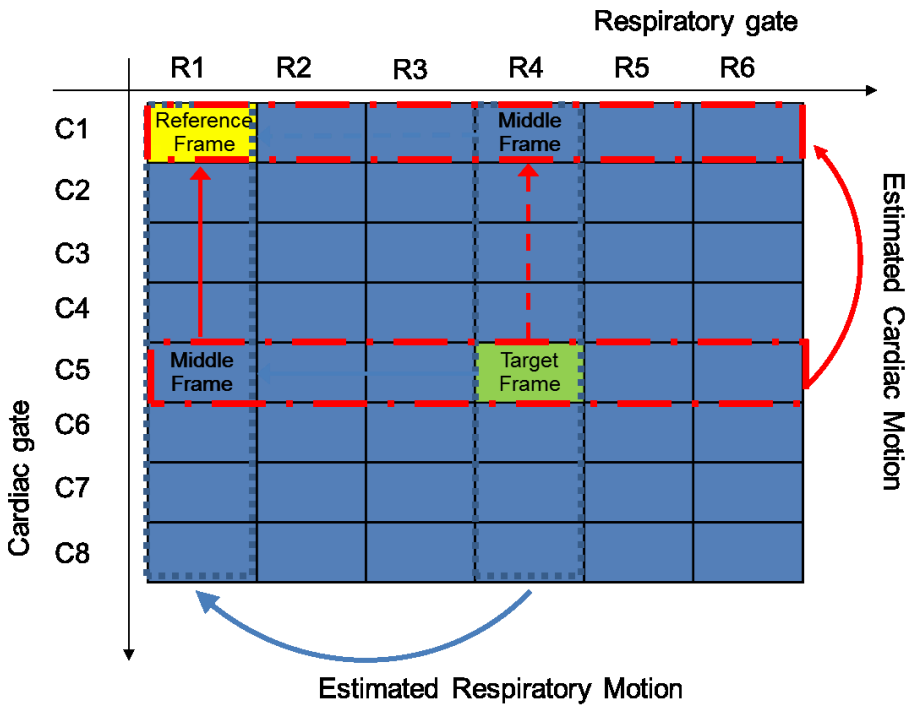

Figure 2-16 Scheme for combining estimated respiratory and cardiac motion.

In step B), same mask as shown in Figure 2-14 were applied for cardiac motion estimation. In step C), to generate dual R&C motion that can transform arbitrary target frame into the reference frame, two possible ways exists as shown in Figure 2-16 with solid arrow and dash arrow. The solid arrow path was chosen to be consistent with the other methods.

Method 3: Four-step approach

Similar to three-step approach, R&C motion were estimate in two different steps. However, the influence of respiratory motion on cardiac motion was taken into consideration by incorporating an additional step into the previous approach (Figure 2-17):

a) Estimation of respiratory motion based on respiratory gated reconstructed images

b) Image-based respiratory motion correction on dual R&C gated reconstructed images to generate respiratory motion free cardiac gated images.

c) Estimated of cardiac motion based on respiratory motion corrected, cardiac gated images

d) Calculation of dual R&C motion based on estimated respiratory motion and cardiac motion.

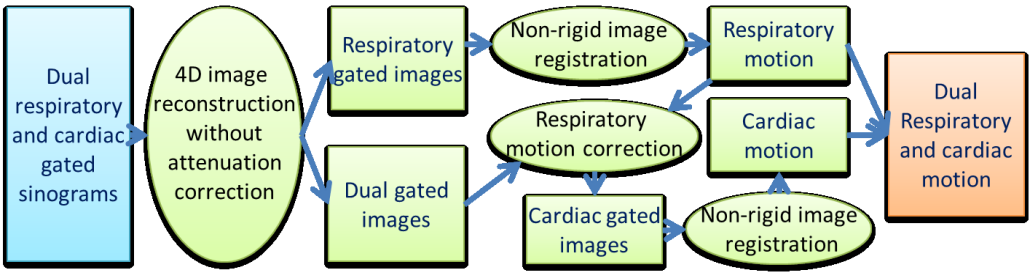

Figure 2-17 The flowchart for four-step dual respiratory and cardiac MEAR.

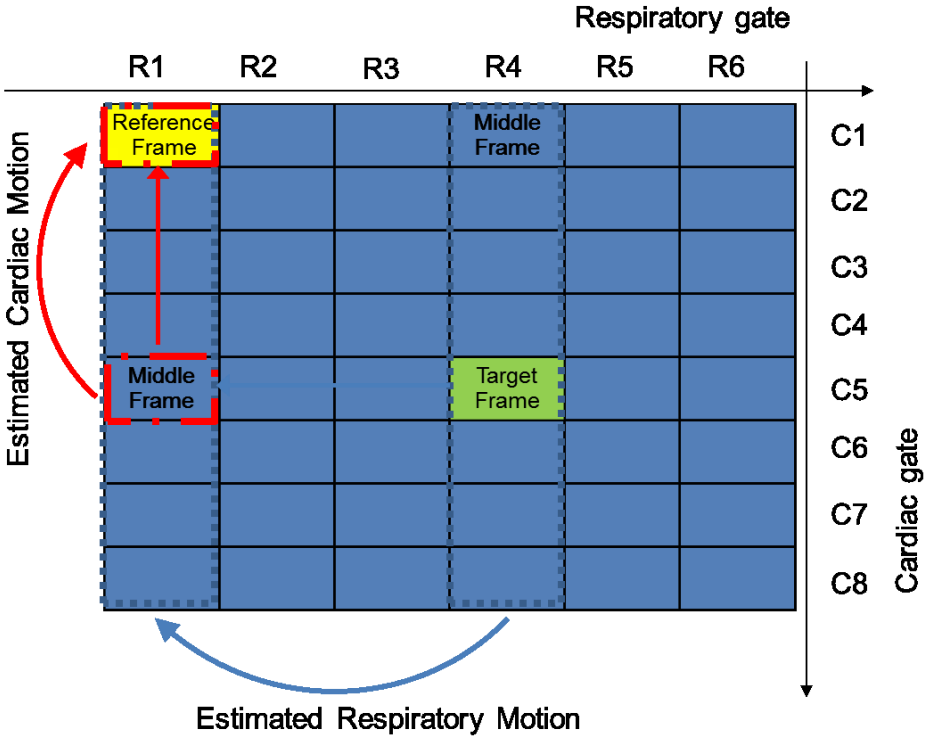

Figure 2-18 Scheme for combining estimated respiratory and cardiac motion.

With estimated cardiac and respiratory motion for each individual voxel, MVF for each dual R&C phase to the reference frame was calculated. Unlike the three-step approach, to obtain dual R&C motion, only one path was possible.

The calculation of the MVF on voxel index *j* was not a simple addition of cardiac MVF and respiratory MVF of the corresponding voxel. In actual implementation to transform the target frame into reference frame, inverse motion transform was used instead of forward motion transform as shown in Figure 2-19. The reason was that the inverse transform guaranteed every voxel in the reference frame had a

corresponding voxel in the target frame, so that the reference frame could be calculated from the target frame, which was not true in forward transform. In the actual implementation to combine R&C motion as shown in Figure 2-20, the cardiac MVF on voxel j and the respiratory MVF on voxel j' were summed, where voxel j' is the destination of the cardiac MVF at voxel j.

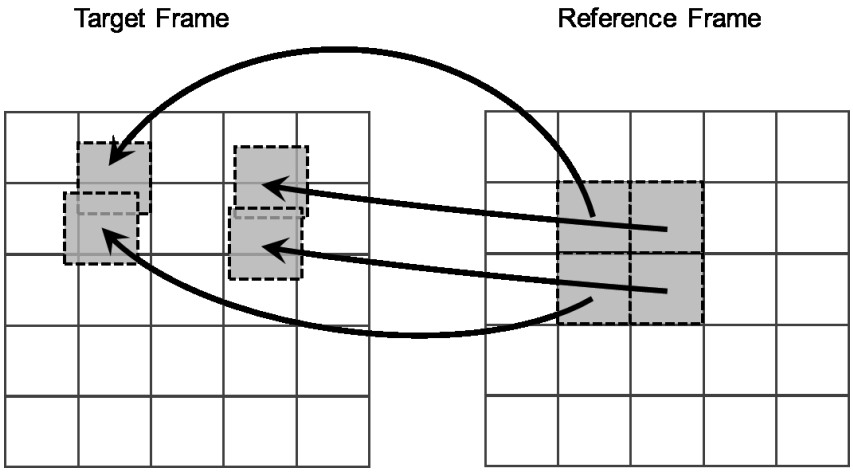

Figure 2-19 Inverse motion transform used in actual implementation

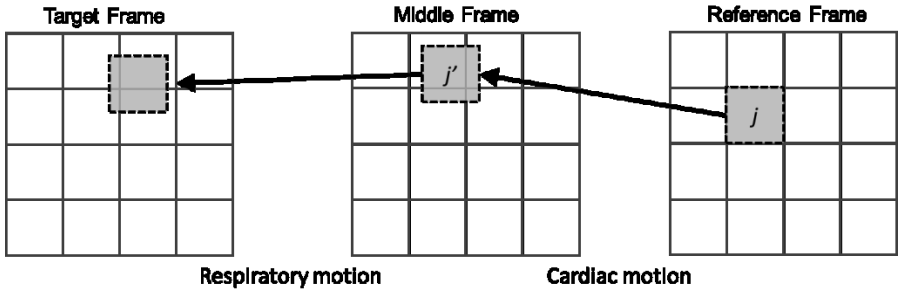

Figure 2-20 The calculation of dual respiratory and cardiac motion based on inverse motion transform.

Method 4: Iterative approach

The iterative approach was an extension to the Four-step approach. The effect of cardiac motion on respiratory motion estimation was also taken into consideration. For each iteration, the following steps were executed:

a) Image-based cardiac motion correction on dual R&C gated images using estimated cardiac motion of each respiratory gate from last iteration, resulting in respiratory gated images with cardiac motion correction.

b) Estimation of respiratory motion based on cardiac motion corrected, respiratory gated reconstructed images.

c) Image-based respiratory motion correction on dual R&C gated reconstructed images using estimated respiratory motion from last step, resulting in cardiac gated images with respiratory motion correction.

d) Estimated of cardiac motion based on respiratory motion corrected, cardiac gated images.

e) Calculation of dual R&C motion, as well as cardiac motion for each respiratory gate.

MOTION ESTIMATION DURING IMAGE RECONSTRUCTION (MEDR)

Unlike MEAR method mentioned in the last section, motion estimation during image reconstruction essentially incorporate motion effects within image reconstruction process that can estimate both activity and motion using the maximum likelihood criteria. Considering the motion effect, the likelihood function for the image reconstruction problem provided by Equation 1-14 can be expressed as:

$$f(\boldsymbol{p}|\boldsymbol{M},\boldsymbol{x}) = \prod_{g}\prod_{i}\left(\left(\sum_{n} K_{i,n}\sum_{j} M_{g,n,j}x_j\right)^{p_{g,i}} \exp\left(-\sum_{n} K_{i,n}\sum_{j} M_{g,n,j}x_j\right)\right).$$

Equation 2-5

Where g is the index of the different cardiac gates, i is the index of projection bins, with total number of I projection bins, j is the index of reconstructed reference image, with total number of J voxels, n is the the index of target frame, with the same total J voxels. $M_{g,n,j}$ is the motion transformation matrix (MTM) that wrap reference frame to the g^{th} frame. R, x_j is the activity of pixel j in the reference frame. $\boldsymbol{K}$ is projection matrix. Both $\boldsymbol{M}$ and $\boldsymbol{x}$ are unknown. The maximum likelihood solution of $\boldsymbol{M}$ is the one that maximize Equation 2-5.

In the above equation, both activity distribution in the reference frame $\boldsymbol{x}$ and MTM $\boldsymbol{M}$ are unknown. To simplify the process and focus on the motion estimation, Equation 2-6 was used to calculate the estimate of $\boldsymbol{x}$ using the gated projection data corresponding to the reference frame p_{ref}, which is basically the conventional approach of calculating gated reconstructions without motion correction.

$$\hat{x}_j^{l+1} = \frac{\hat{x}_j^l}{\sum_i K_{ij}} \sum_i K_{ij} \frac{p_{ref,i}}{\sum_{j'} K_{ij'} \hat{x}_{j'}^l}$$

Equation 2-6

The log of Equation 2-5 with fixed activity distribution in the reference frame from Equation 2-6 is

$$\mathrm{L}(\boldsymbol{M}) = \log\big(f(\boldsymbol{p}|\boldsymbol{M})\big) = \sum_g \sum_i \left(p_{g,i} \log\left(\sum_n K_{i,n} \sum_j M_{g,n,j} \hat{x}_j \right) - \sum_n K_{i,n} \sum_j M_{g,n,j} \hat{x}_j \right).$$

Equation 2-7

The size of MTM is *J* by *J* for a given gate, which is extremely large. The problem of a direct estimation of MTM is underdetermined. However, the matrix $\boldsymbol{M}$ is a sparse matrix which can be represented by 3D MVF. The relationship of the MTM and a corresponding MVF is shown in Figure 3.1. By using MVF as a replacement of $\boldsymbol{M}$, we were able to rewrite the log-likelihood function $\mathrm{L}(\boldsymbol{M})$ as $\mathrm{L}(\boldsymbol{m})$, where $\boldsymbol{m}$ represents the MVF that transform the reference frame to a target frame. Based on the inverse motion rule in the implementation as shown in Figure 2-19, the index of the MVF is the same as the index of the target frame, which is *n*. To maximize the log-likelihood function, its partial derivatives with respect to the MVF for individual voxels were calculated.

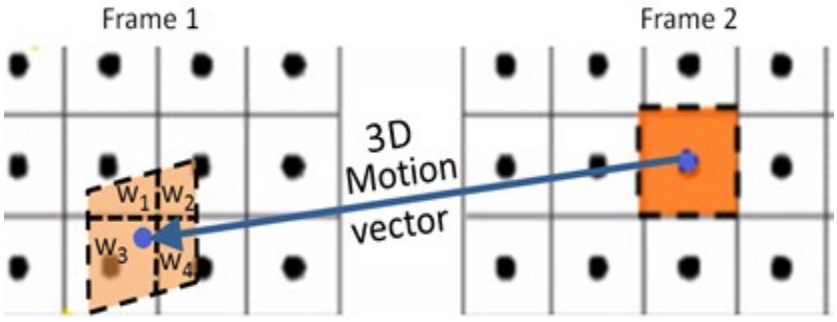

Figure 2-21 The relationship of 3D MVF and motion transformation matrix.

A motion vector represents both the direction and magnitude of the 3D motion. Motion transformation matrix is a discrete representation of the motion using weighted sums.

There are three components for a 3D motion vector of a single voxel, $\boldsymbol{m_{g,n}} = \hat{\boldsymbol{u}} m_{g,n,u} + \hat{\boldsymbol{v}} m_{g,n,v} + \hat{\boldsymbol{w}} m_{g,n,w}$, where $\hat{\boldsymbol{u}}, \hat{\boldsymbol{v}}, \hat{\boldsymbol{w}}$ is the unit vector in three coordinates. Thus for pixel *n,* the derivative of of the log likelihood function with respect to its *u* axis component is:

$$\frac{\partial \log\left(f(\boldsymbol{p}|\boldsymbol{m})\right)}{\partial m_{g,n,u}} = \sum_{j'} \sum_{n'} \frac{\partial \log\left(f(\boldsymbol{p}|\boldsymbol{M})\right)}{\partial M_{g,n',j'}} \frac{\partial M_{g,n',j'}}{\partial m_{g,n,u}}.$$

Equation 2-8

Where

$$\frac{\partial \log\left(f(\boldsymbol{p}|\boldsymbol{M})\right)}{\partial M_{g,n,j}} = \sum_{i} \left(\frac{p_{g,i} K_{i,n} \widehat{x_j}}{\sum_n K_{i,n} \sum_{j'} M_{g,n,j'} \widehat{x_{j'}}} - K_{i,n} \widehat{x_j} \right).$$

Equation 2-9

$\frac{\partial M_{g,n_1',j}}{\partial m_{j,x}}$ represents the relationship of 3D motion transformation matrix and motion vector field, which was calculated numerically. The double summation implies that the change of a motion vector in the target frame affects multiple voxels in both target frame and reference frame used for calculation (Figure 2-22).

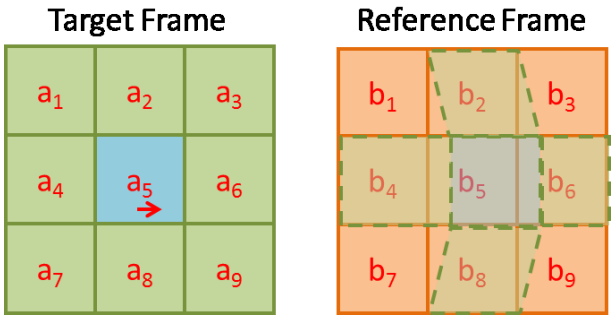

Figure 2-22 Illustration of a small change of motion vector in voxel a_5 in target frame.

The blue overlay in the reference frame represents the corresponding voxel a_5 in target frame, in which case, the intensity of a_5 equals to the weighted sum of b_5 and b_6. The green overlay in reference frame represents the neighboring voxel of a_5 in the target frame. The calculation of the neighboring voxels is also changed, suggesting a single change in the MVF affects multiple voxels in both target and reference frame.

The physical meaning of $\frac{\partial \log(f(\boldsymbol{p}|\boldsymbol{x},\boldsymbol{m}))}{\partial m_{j,x}}$ is to which direction of changing the motion vector will increase the log-likelihood. Given the value of derivatives, a modified steepest descent approach is used to update motion vector for a given voxel.

$$m^{t+1}{}_{j,u} = m^{t}{}_{j,u} + \frac{\partial \log\left(f(\boldsymbol{p}|\boldsymbol{m})\right)}{\partial m_{j,u}} \cdot stepsize.$$

Equation 2-10

The value of $stepsize$ was dynamically updated by comparing iteration *t* and *t*+1. In cases where the sign of $\frac{\partial \log(f(\boldsymbol{p}|\boldsymbol{m}))}{\partial m_{j,u}}$ changed, the value of $stepsize$ was also reduced to accommodate the change. Initial MVF calculated by using MEAR method was used as initial value in Equation 2-10 for better and faster estimation.

MEDR was implemented by modifying the source code of STIR [93] software. Due to its complexity and intensive computation cost, MEDR was only implemented for cardiac motion estimation instead of dual R&C motion estimation.

MOTION ESTIMATION BEFORE IMAGE RECONSTRUCTION (MEBR)

The first question of estimating non-rigid patient motion on the projection data before reconstruction [94] is, with the motion existing in image space, is there a corresponding projection domain motion transformation?

To answer this question, first we model the projection process given the effects of motion in image domain using the following equation:

$$\boldsymbol{p_1} = \boldsymbol{K x_1} = \boldsymbol{K M_{ref \to 1} x_{ref}},$$

Equation 2-11

where $\boldsymbol{x_{ref}}$ is the activity distribution of the reference frame, $\boldsymbol{M_{ref \to 1}}$ is the motion transformation matrixthat transforms the reference frame to frame 1. $\boldsymbol{K}$ is the projection matrix. $\boldsymbol{p_1}$ is the projection data

for frame 1. For a solvable system, $\boldsymbol{K}$ is invertible. By reconstructing the projection data and invert image domain motion transformation in Equation 2-11, the intensity map of the reference frame can be calculated by the following equation:

$$\boldsymbol{x_{ref} = M_{1\rightarrow ref} K^{-1} p_1}.$$

Equation 2-12

By introducing

$$\boldsymbol{N_{1\rightarrow ref} = K M_{1\rightarrow ref} K^{-1}}$$

Equation 2-13

the above equation can be expressed as::

$$\boldsymbol{x_{ref} = K^{-1} K M_{1\rightarrow ref} K^{-1} p_1 = K^{-1} N_{1\rightarrow ref} p_1},$$

Equation 2-14

Equation 2-13 and Equation 2-14 suggested that the projection domain motion transform do exist. Mowever, Equation 2-13 provides us a way to estimation projection domain motion transformation $\boldsymbol{N}$ from projection data. Figure 2-23 showed how the motion in image domain influence the projection data. Because of motion, the same LOR in reference frame was transformed into a curved LOR in target frame. In the reference frame, the LOR was measured in a single detector bin, but in the target frame, the corresponding LOR was shared by multiple detector bins. As illustrated in Figure 2-23 and Equation 2-13, the unique properties of non-rigid motion transformation in projection domain are summarized as: (1) in the projection domain a point is transformed to an area, (2) the transformed area can overlap with each other; (3) the transformation is 2D, with no motion transformation between different angles.

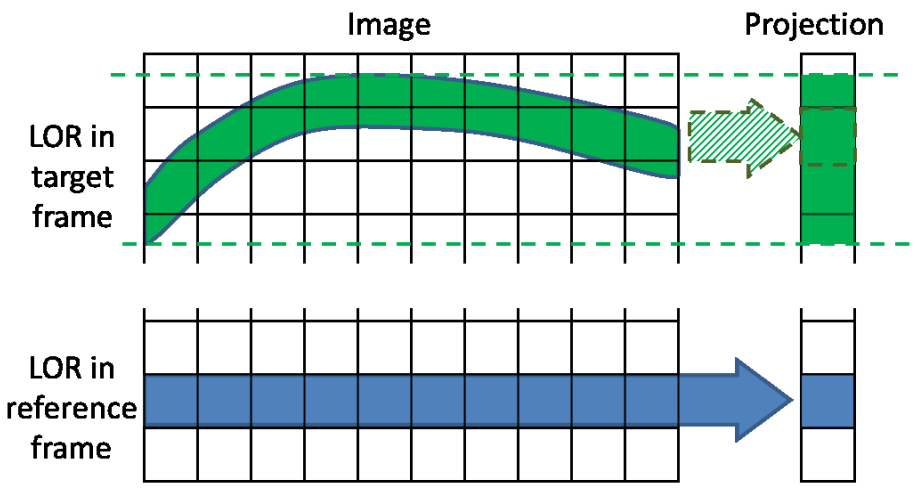

Figure 2-23 Illustration of the effect of motion on LOR and projection data.

In 3D case, motion transformation in projection domain effectively transforms a voxel into an area. The value in the voxel is spread out in the area. The spread-out may not be uniform. The transformation in projection domain is essentially the projections of image domain motion transformation.

Respiratory motion in projection data is approximated using point-to-point transformation instead of point-to-area transformation. The approximation is reasonable for respiratory motion since the direction and magnitude of respiratory motion in adjacent locations inside the body is similar. However, similar approach is not applicable to cardiac motion estimation due to its large spatial variation, as shown in Figure 2-24. Based on this approximation, the motion transformation in sinogram domain was estimated using a 2D image registration algorithm, which is represented by Equation 2-15:

$$n_{1\to ref,\theta} = \text{argmin}_{n_\theta}\left(p_1(\theta, r + n_\theta) - p_{ref}(\theta, r)\right),$$

Equation 2-15

where $n_{1\to ref,\theta}$ is the transformation in projection domain for the θ-th angle that transforms projection frame 1 into reference projection frame.

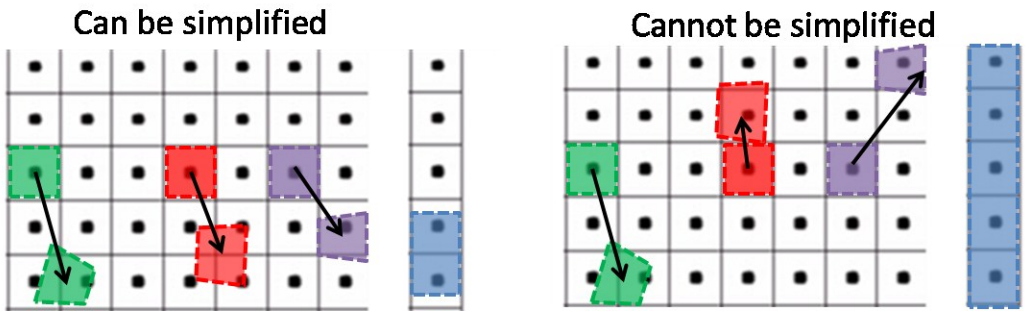

Figure 2-24 Cases where the approximation can be applied and cannot.

As shown in Figure 2-23 and Equation 2-15, the main advantage of the MEBR over MEAR and MEDR is that MEBR corrects motion in the projection domain and therefore does not require any reconstruction at all. The disadvantage of MEBR is the approximation used to derive Equation 2-15 limits its accuracy and prevents its application in cardiac motion estimation.

MOTION ESTIMATION BASED ON OTHER MODALITIES

With the wide use of PET/CT and the emergence of simultaneous PET/MRI, the estimation of patient motion of using the other modality instead of PET is becoming a viable solution. Motion estimation using CT from PET/CT requires additional radiation dose to the patient, which is not desirable. In this study, we focus on the motion estimation from simultaneous PET/MRI.

MOTION ESTIMATION FROM SIMULTANEOUS PET/MRI

MOTION ESTIMATION FROM MRI NAVIGATOR

Respiratory motion is 3D non-rigid motion by nature, but it can be approximated by 1D affine motion along axial direction. MRI pencil beam navigator provides 1D image of the liver-lung boundary, as shown in Figure 2-25, which is essential to calculate the 1D affine motion. It is a known fact that the respiratory motion amplitude at the top of lung is approaching zero. A linear interpolation model was used to derive the 1D respiratory MVF in the lung area based on navigator measurement as shown in Figure 2-26, the respiratory motion amplitude in the liver and lower abdomen was assumed to be the same as the

measurement of navigator. The directions of the vectors in the 1D MVF are along the axial direction as shown in Figure 2-25.

Figure 2-25 Illustration of 1D respiratory motion measured using MRI navigator.

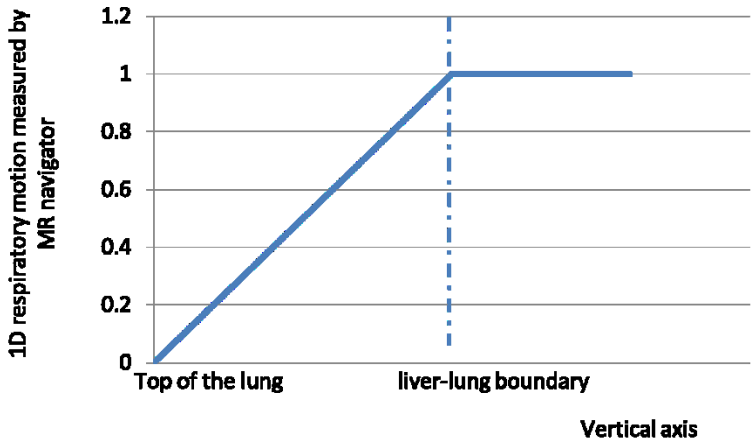

Figure 2-26 Illustration of linear interpolation model used to calculate 1D respiratory MVF.

MOTION FROM 4DXCAT

4D XCAT provides not only 4D phantom images, but also realistic 4D MVF between any two individual frames as shown in Figure 2-27 [95]. The MVF from 4D XCAT was used as truth for phantom studies and was also treated as the best achievable MVF estimated from other modalities such as MRI. Motion generated by 4D XCAT was time-based motion with fixed cardiac and respiratory period, however in real situation, both R&C period are changing over time and are uncorrelated. This results in different dual motion pattern as shown in Figure 2-28. In other words, the motion phases from actual patient scans covered the whole 2D grid in cardiac gate-respiratory gate space, while those from 4D XCAT only covered a band with fixed cardiac and respiratory period.

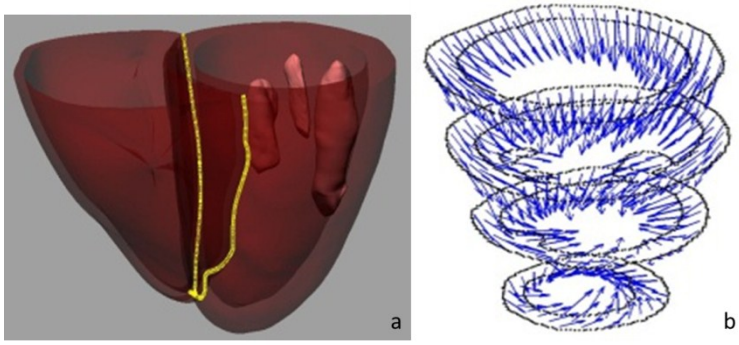

Figure 2-27 Illustration of a) anatomical structure of the heart, b) cardiac motion from 4D XCAT.

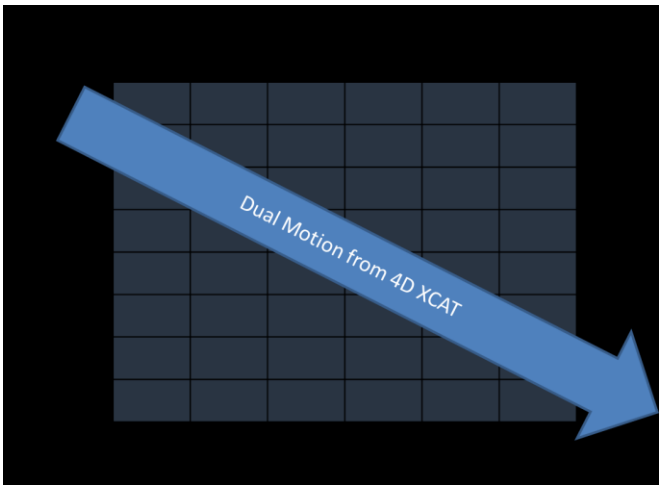

Figure 2-28 The difference of motion phases from actual patient and 4D XCAT.

To generate realistic dual R&C motion, and cover all sampling point shown in Figure 2-28, 4D XCAT were executed multiple times each with a different parameter file. In each parameter file that responsible to generate motion to the i-th cardiac gate and j-th respiratory gate, only the parameters that control respiratory ($Period_{Resp}$) and cardiac motion period ($Period_{Card}$) were different and were set to:

$$\begin{cases} Period_{Resp} = TJ/j \\ Period_{Card} = TI/i \end{cases}$$

Equation 2-16

T is the parameter that determine the output period in the 4D XCAT parameter file. J is the number of respiratory gates and I is the number of cardiac gates. Equation 2-16 suggested that after time T, the phase

of respiratory motion is at *j/J* while the phase of cardiac motion is at *i/I*, i.e. the i-th cardiac gate and j-th respiratory gate.

Respiratory motion generated by 4D XCAT is based on time, but as amplitude-gating is used in this study, extra step was taken to convert time-based respiratory motion to amplitude-based respiratory motion.

Two different choices of reference frames were studied as shown in Figure 2-29. Choice 1: reference frame placed at end-inspiration respiratory and end-diastolic cardiac motion phase. Choice 2: reference frame in the very middle of both R&C motion. Choice 1 resulted in larger absolute motion amplitude and motion from other gates being in the similar direction. The second choice resulted in smaller absolute motion amplitude and balanced motion direction from other gates.

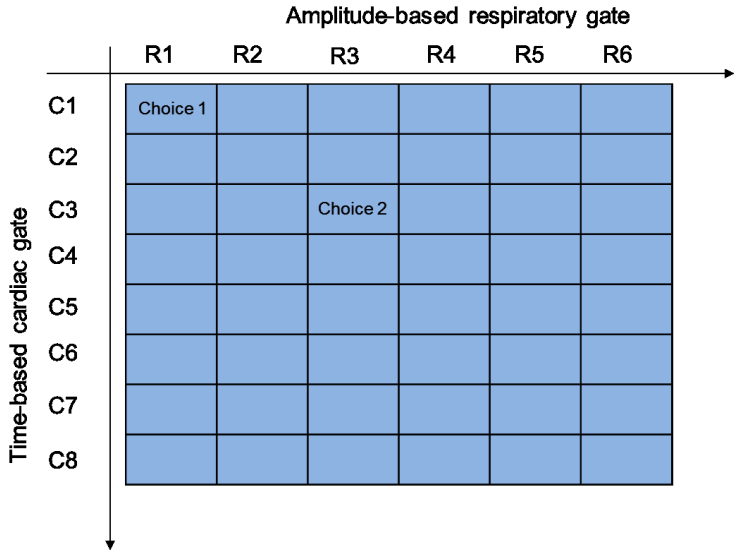

Figure 2-29 Two choices of reference frame for true MVF.

The spatial resolution of generated 4D MVF was much higher than the actual PET data. To study the effects of motion-activity resolution mismatch a second set of 4D MVF was generated with additional Gaussian filter of 6mm standard deviation, which matched the system resolution of simulated PET system.

4. MOTION CORRECTION TECHNIQUES

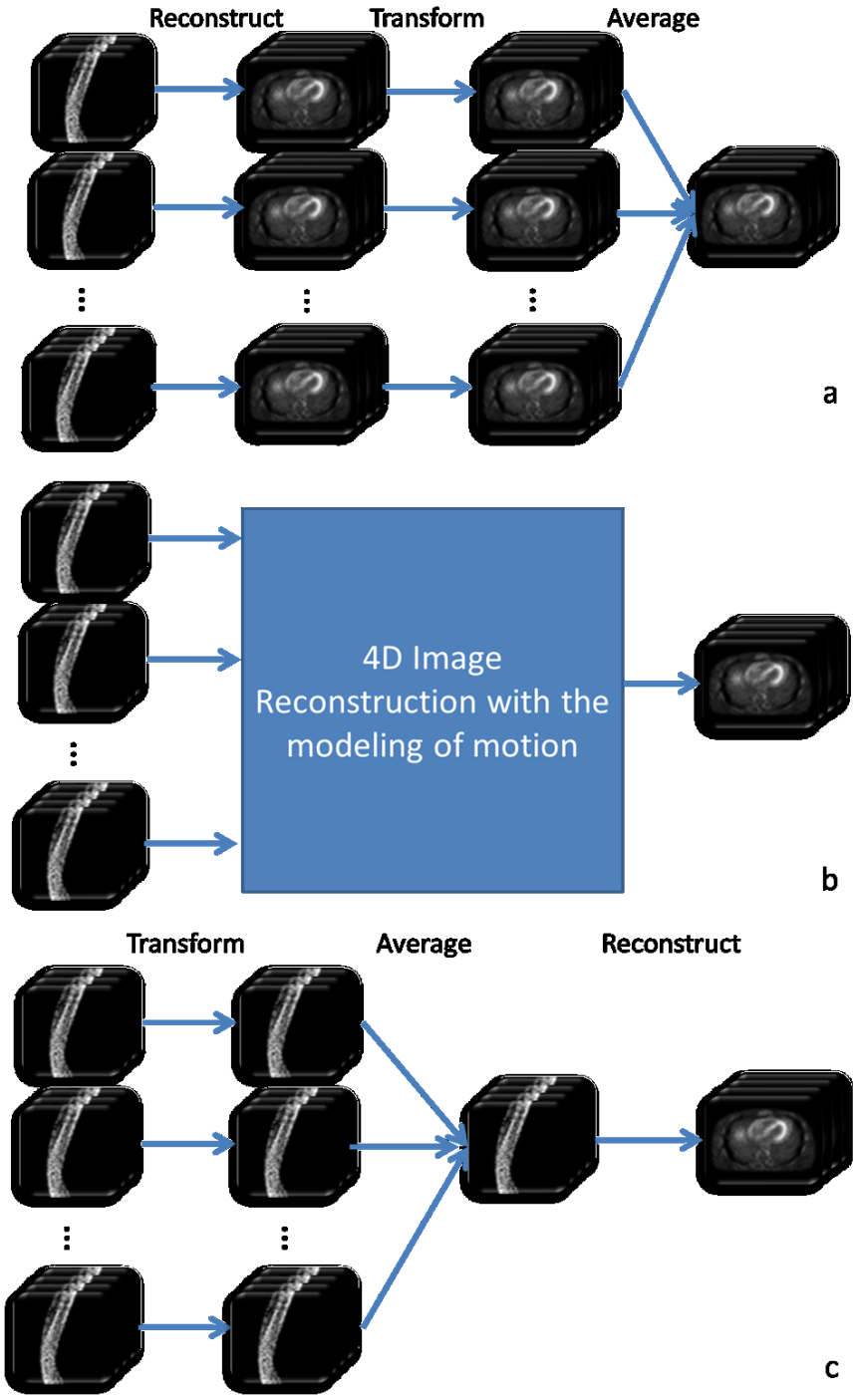

Figure 2-30 General schemes for a) MCAR, b) MCDR, c)MCBR.

With estimated MVF and gated projection data, the final step of 4D image reconstruction with motion correction is to model the motion effects. There are three general approaches to compensate dual R&C

motion, which are motion correction after, during and before reconstruction (MCAR, MCDR, and MCBR). The general schemes for these approaches are shown in Figure 2-30.

DUAL R&C MOTION CORRECTION AFTER RECONSTRUCTION (MCAR)

This approach is similar to the registration-transformation-average (RTA) approach commonly used in respiratory motion correction in which motion correction is performed by transforming all frames to the reference frame. Difference between common RTA approach and our method is that respiratory-gated attenuation map was employed to do a second reconstruction of dual gated sinograms to correct for attenuation effect, which was based on an algorithms previously proposed in [92]. The respiratory gated attenuation maps were generated by transforming the original non-gated attenuation map with the estimated respiratory MVF. Attenuation maps were respiratory-gated only as literature suggested that the effects of cardiac motion on attenuation map were negligible [96]. Scatter was corrected on the projection data before motion correction.

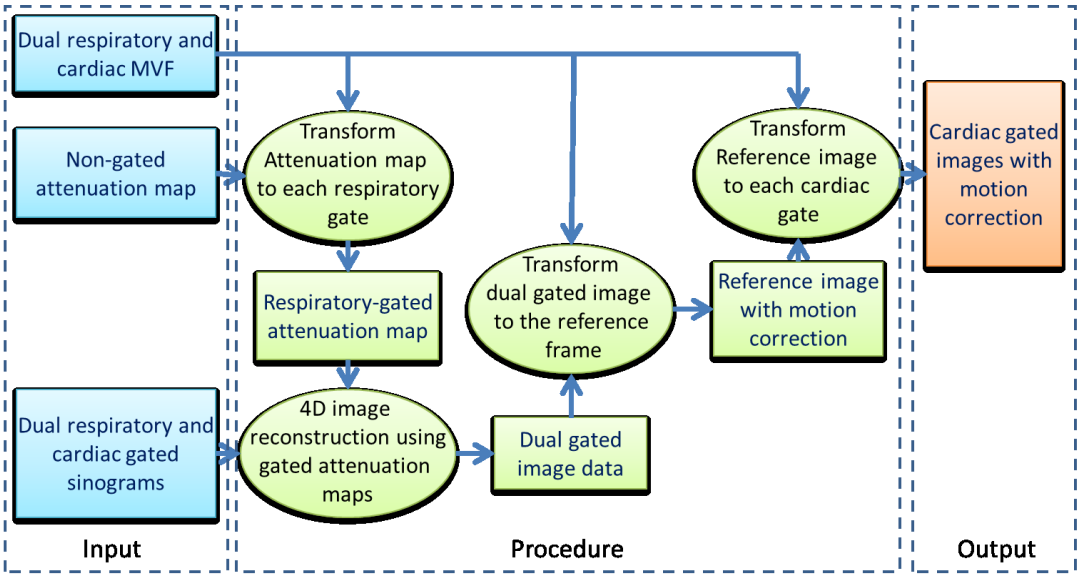

Figure 2-31 Flowchart of MCAR for dual respiratory and cardiac motion.

With respiratory-gated attenuation maps, dual gated projection data were reconstructed using OS-EM image reconstruction algorithm with attenuation correction. Image-based transformation were applied on the dual gated reconstruction and summed into one reference image with reduced motion effect from both

R&C motion without sacrificing image statistics. The reference image was transformed back into each cardiac gate using the estimated cardiac motion to produce final cardiac gated images with motion correction. This process is illustrated in Figure 2-31.

DUAL R&C MOTION CORRECTION DURING RECONSTRUCTION (MCDR)

Our second approach, MCDR [97, 98], incorporates motion into the likelihood function, which is shown in Equation 2-17.

$$f(\boldsymbol{p}|\boldsymbol{x}) = \prod_g \prod_i \left(\left(\sum_n K_{g,i,n} \sum_j M_{g,n,j} x_j \right)^{p_{g,i}} \exp\left(- \sum_n K_{g,i,n} \sum_j M_{g,n,j} x_j \right) \right),$$

Equation 2-17

Similar to Equation 2-5, where g is the index for gate, i is the index for projection bin, and j is the index for the voxel in reconstructed image $\boldsymbol{x}$. M_g is the MTM that transforms the unknown reference frame x to the g-th gated frame, which is known unlike that in Equation 2-5. K_g is the projection matrix that projects gth gated frame to gth gated projection data. Attenuation effect is modeled within K_g. As argued above, the effect of cardiac motion on attenuation coefficient is negligible, thus K_g and $K_{g'}$are only different if and only if g and g' are two different respiratory phase. p_g is the gth gated projection data, which is known. Scatter effects are not modeled in Equation 2-17, as all scatter correction in our approach was accomplished in projection domain before reconstruction.

Using ML-EM approach, the update formula for $(l+1)$th iteration is written in Equation 2-18

$$\hat{x}_j^{l+1} = \hat{x}_j^l \left[\frac{\sum_g \left(\sum_n M_{g,n,j} \left(\sum_i \left(\frac{K_{g,i,n} p_{g,i}}{\sum_n K_{g,i,n} \cdot \left(\sum_{j'} M_{g,n,j'} x_{j'}^l \right)} \right) \right) \right)}{\sum_g \left(\sum_n M_{g,n,j} \sum_i K_{g,i,n} \right)} \right],$$

Equation 2-18

where x_j^l is the j-th voxel value of the reconstructed image after the l-th iteration. This update equation is similar to traditional update equation of the ML-EM approach, but with addition of 4D dataset (p_g) as well as the motion transforms in both projection and back-projection. The term $\sum_j M_{g,n,j} x_j^l$ represents the motion transform of the reference image at l-th iteration to the g-th gated reconstructed image, while the term $\sum_n M_{g,n,j} \cdot$ in the above equation represents the transpose motion transform. The combination of motion transform and transpose motion transform corresponds to the projection and back-projection process, in which case the first one is the forward calculation using the projection matrix $\boldsymbol{K}$, while the later one is the transpose calculation of the projection matrix $\boldsymbol{K}$. The summation over all difference gates implies in the use of whole data set for the calculation of the reference frame, instead of partial dataset in conventional gating approach shown in Equation 2-6.

In the conventional transformation process showed in Figure 2-19 (calculation of reference frame given target frame) and Figure 2-32 (calculation of target frame given reference frame) was used to calculate the voxel value at index j in the reference frame:

$$x_{ref}(j) = \sum_{n=1}^{8} w'_{n,j} x_{target}(n), \qquad \sum_{n=1}^{8} w_{n,j} = 1$$

Equation 2-19

where $w'_{n,j}$ is the intersecting volume of the transformed voxel j with the original voxel grid n as shown in Figure 2-19. The largest number of intersected voxels is 8 as the transform voxel j is still a cube, and the summation of all intersected volume is 1.

During motion transformation process, adjacent voxels may overlap or gaps may be created. The existence of overlaps or gaps in may not be a problem of the calculation of motion transform, such as the image transformation term $\sum_j M_{g,n,j} x_j^l$ that transformed the reference image into target image in Equation 2-18. As shown in Figure 2-32, to calculate the voxel value of the target frame at index n_7, the weighted sum of voxel j_2 and voxel j_7 in the reference frame was required, so for every voxel in that target frame, similar approach guaranteed that all voxels can be calculated. However, in cases where the transpose motion

transform was required such as the term $\sum_n M_{g,n,j} \sum_i K_{g,i,n}$ in Equation 2-18. The summation over index n did not guarantee that every voxel index j in the reference frame has a non-zero value. As shown in Figure 2-32, the value of voxel j_8 is undetermined since it is located in the gap created by motion. Direct use of the conventional motion transform scheme resulted in zero value in sensitivity and back-projected value for certain voxels and certain gates, suggesting that certain voxels in the reconstructed image may only contain a subset of instead of the whole dataset, which is undesirable. As the traditional interpolation scheme does not guarantee to use every voxel for motion transformation process ($\sum_{j'} M_{g,n,j'} x_{j'}^{l}$) and hence the calculated value for applying transpose MTM can be zero additional approximation is unavoidable. Approximations by replacing the transpose of MTM with the inverse MTM to replace were often used [72]. In this work we also studied the difference of using transpose MTM and inverse MTM approximations.

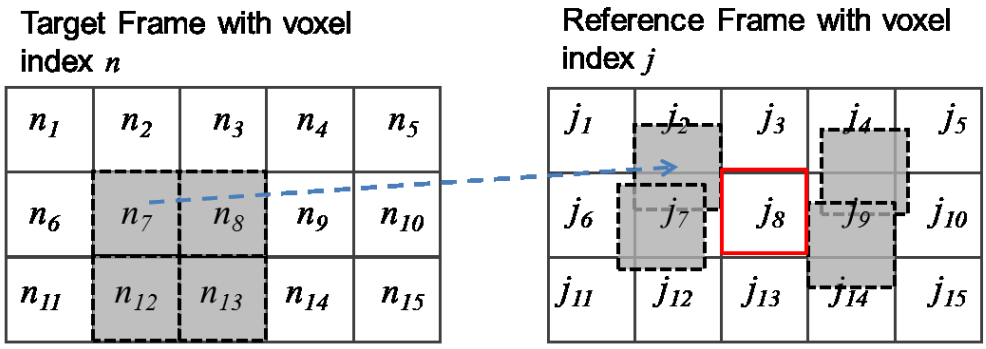

Figure 2-32 The use of conventional motion transform scheme results in inaccurate implementation of transpose motion transform.

To accurately implement the transpose motion transform, a new interpolation scheme for motion transform that allows no gaps or overlaps was developed as shown by Figure 2-33. The major difference is that for given voxel j in the reference frame, the new motion transformation scheme as shown in Figure 2-33. transforms the voxel (3D cube with volume 1) into a 3D shape with volume V_j based on the MVF, while in the old motion transformation scheme (Figure 2-19 and Figure 2-32), each voxel after transformation is still a cube with volume 1 independent of the MVF. A the transformed voxel is no longer a cube in the new approach, the maximum number of intersected volume is unfixed and the summation of all intersected volume ($\sum_{n=1}^{N} w_{n,j}$) is not 1 but V_j as described in Equation 2-20. The resulting motion transformation

matrix is invertible and the inverse (Equation 2-21) or transpose motion transform (Equation 2-22) can be calculated without further approximation. Therefore, unlike that in Figure 2-19, the inverse motion transform is not necessary in the new approach.

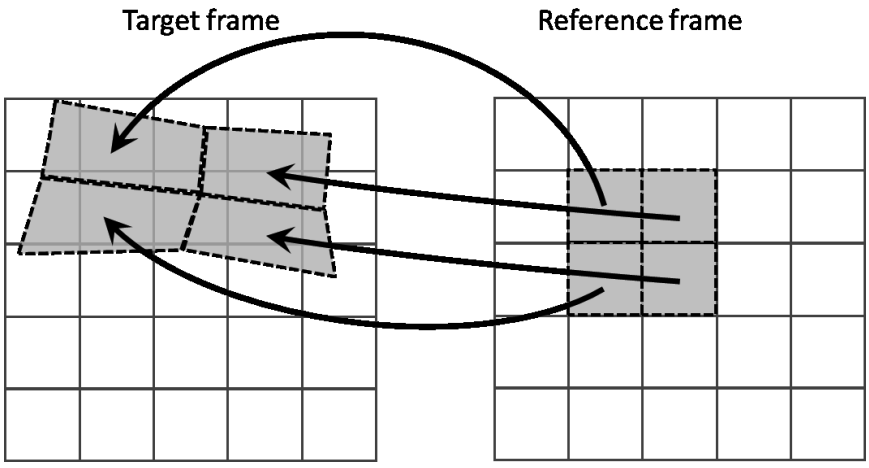

Figure 2-33 2D illustration of new interpolation method for motion transformation.

$$x_{ref}(j) = \sum_{n=1}^{N} w_{n,j} x_{target}(n), \qquad \sum_{n=1}^{N} w_{n,j} = V_j \,, \sum_{j=1}^{J} w_{n,j} = 1$$

Equation 2-20

$$x_{target}(n) = \sum_{j=1}^{J} \frac{w_{n,j}}{V_j} x_{ref}(n),$$

Equation 2-21

$$x_{target}(n) = \sum_{j=1}^{J} w_{n,j} x_{ref}(n),$$

Equation 2-22

Compared with the conventional interpolation scheme, the new approach as shown by Equation 2-20, Equation 2-21, and Equation 2-22 is inherently activity preserving without external constrain. Activity preserving implies that both global and local activity preserves but not voxel intensity during the transform, therefore an expansion would result in reduced voxel intensity and compression increased voxel intensity.

Non-activity preserving transform, on the other hand, do not preserve activity globally while the voxel intensity remains unchanged regardless of expansion or compression. Non-activity preserving motion transform for new motion transformation scheme is implemented in Equation 2-23 by further dividing the total volume in target frame for each voxel. The transpose motion transform for non-activity preserving transform turns out to be the same as the activity preserving inverse motion transform in Equation 2-21. Similarly, the inverse motion transform for non-activity preserving transform is the same as the transpose motion transform in activity preserving scheme described in Equation 2-22. The conventional interpolation scheme is not inherently activity preserving but can be modified by adding Jacobian matrix [79].

$$x_{ref}(j) = \frac{1}{V_j}\sum_{n=1}^{N} w_{n,j} x_{target}(n), \qquad V_j = \sum_{n=1}^{N} w_{n,j}$$

Equation 2-23

The transformation in Equation 2-18 was done by applying both activity-preserving and non-activity-preserving motion transformation with estimated R&C motion. The advantage of activity-preserving motion transform is that it models not only possible activity change due to tissue compression but also the activity change due to partial volume effects (PVE). In cardiac gated images, different gates have different myocardium wall thickness. The myocardium intensity changes as the heart contract or relax, and the PVE will further reduce the intensity of myocardium boundaries, leading to inaccurate quantitation. Thus an activity-preserving motion transformation is required. Compared with other activity-preserving motion transformation models such as transformation with the modeling of Jacobian matrix, our activity-preserving approach has no discretization error therefore was very accurate.

Similar to MCAR, the cardiac gated images with motion correction were generated by transforming the reconstructed reference frame back to each individual cardiac gate.

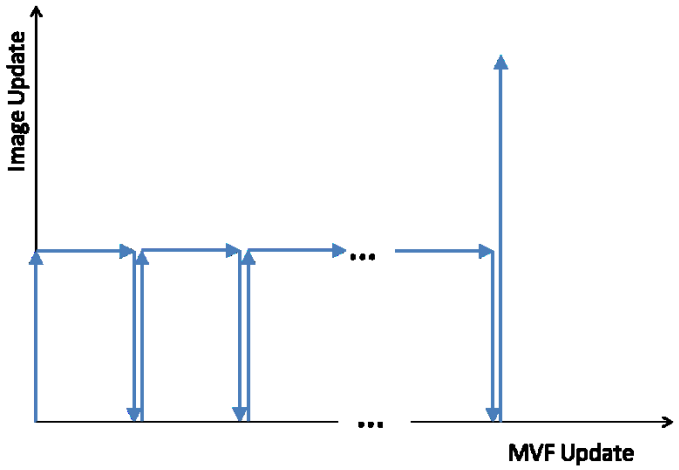

Figure 2-34 Update scheme for simultaneous activity and motion estimation.

With the combination of Equation 2-10 and Equation 2-18, simultaneous estimation of activity and motion was achieved. There are nearly infinite ways to achieve certain iteration point for both activity and motion, a scheme shown in Figure 2-34 was used so that the image updating process was not affected by inaccurate motion estimation. This simultaneous estimation approach was not implemented for dual R&C correction because of the computational complexity of MEDR.

DUAL R&C MOTION CORRECTION BEFORE RECONSTRUCTION (MCBR)

Both MCAR and MCDR require huge amount of computation time when applied for dual R&C motion correction process. The first method demands individual reconstructions for each dual gated dataset while the later uses all gated projections in one reconstruction which requires multiple projection and backprojection process in each iteration. Motion correction on projection data before reconstruction as shown in Figure 2-30c does not have the above problem; but since both R&C motion exists in image domain, transforming projection data is not a straightforward approach. Rigid respiratory motion correction that approximate respiratory motion as simple shifting and rotation was often used for MCBR [82]. However, the both respiratory motion and cardiac motion are in fact non-rigid, with the later more heterogeneous than the former. We developed a method and theory for estimating and applying non-rigid R&C motion correction on the projection data as well as the listmode event before reconstruction given image domain dual R&C MVF [94].

Equation 2-14 suggests that motion correction can be done first in projection domain and then do a normal reconstruction to get the final image. Equation 2-13 showed the existence of projection domain motion transformation and its relationship with image domain motion transformation. As a direct inverse of $\boldsymbol{K}$ is almost impossible, using Equation 2-13 for calculating projection domain motion transform is very difficult. The use of iterative image reconstruction approach to find $\boldsymbol{K}^{-1}$ defeats the purpose of speeding motion correction by applying it on the projection data. Although we proved that motion correction in projection domain is possible, how to find the projection domain motion transformation is still a problem.

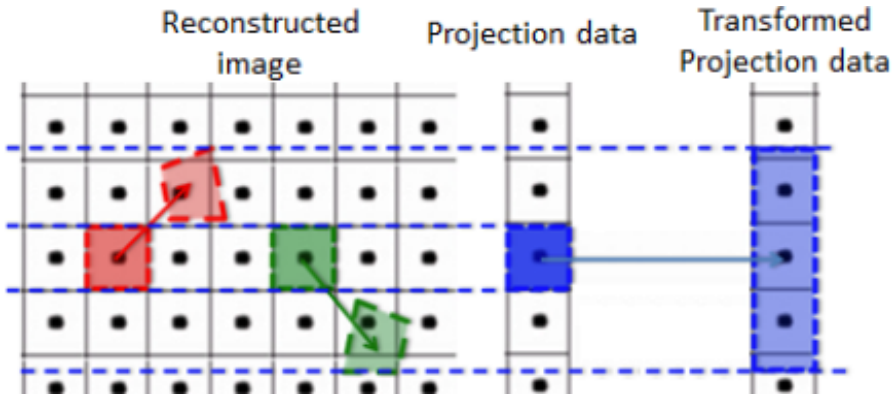

Figure 2-35 The 2D illustration of effects of image domain motion in projection domain.

In 3D case, motion transformation in projection domain effectively transforms a voxel into an area. The value in the voxel is spread out in the area. The spread-out may not be uniform. The transformation is the results of projections of image domain motion transformation.

Figure 2-35 provided another approach to calculate motion transform in projection domain from motion transform in image domain. Without the effects of motion, the value of LOR i is determined from the following equation:

$$p_i = \sum_j K_{i,j} x_j$$

Equation 2-24

For each LOR h with unit vector $\hat{\boldsymbol{l}}_h$, the effect of imaged domain based motion of voxel j on the projection domain was calculated by project its motion vector $\boldsymbol{m}_j$ along the direction of $\hat{\boldsymbol{l}}_h$, by Equation 2-25 shown in Figure 2-36.

$$\boldsymbol{m'}_{h,j} = \boldsymbol{m}_j - (\boldsymbol{m}_j \cdot \hat{\boldsymbol{l}}_h)\hat{\boldsymbol{l}}_h$$

Equation 2-25

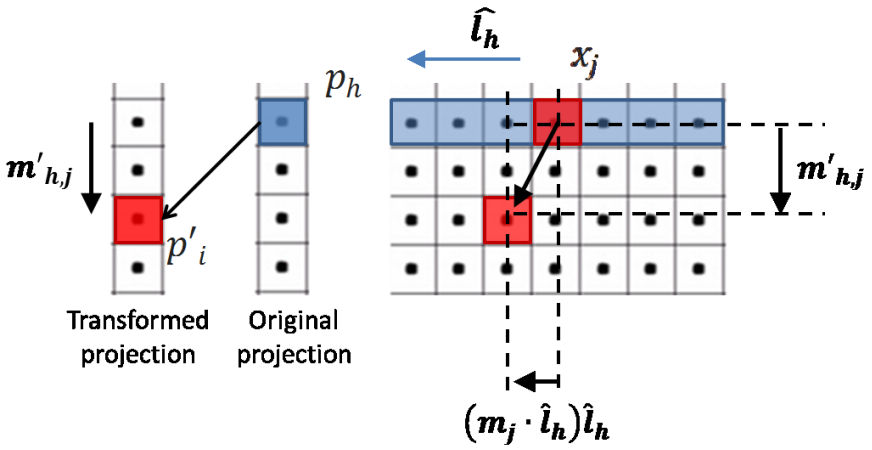

Figure 2-36 Projection of image domain motion vector.

where $(\boldsymbol{m}_j \cdot \hat{\boldsymbol{l}}_h)\hat{\boldsymbol{l}}_h$ is the component of $\boldsymbol{m}_j$ along the direction of LOR h. This component does not contribute to the change in projection domain, as the acquired projection data is an integral along the direction of LOR i. $\boldsymbol{m'}_{h,j}$ is the component in $\boldsymbol{m}_j$ that is perpendicular to the direction of LOR h, i.e. the effective contribution of the image domain motion in voxel j to the motion in projection domain. Given a certain detected event from LOR h, the probability that this event comes from voxel j is given by:

$$Prob(j|LOR\ h) = \frac{K_{h,j}x_j}{p_h}$$

Equation 2-26

In Equation 2-26, p_h is the accumulated value of all events in LOR h, i.e. projection data at detector bin h. x_j is the activity distribution at voxel j, which is unknown. To calculate the probability, an estimated of x_j was used instead by using a scout reconstructed image without motion correction.

Knowing the contribution of image domain motion at voxel *j* (Equation 2-25) and the probability that it is emitted at voxel j (Equation 2-26), the contribution of LOR h to a neighboring LOR $h + \boldsymbol{m'}_{h,j}$, which is $p_{h,h+\boldsymbol{m'}_{h,j}}$,can be calculated using the following equation:

$$p_{h,h+\boldsymbol{m'}_{h,j}} = Prob(j|LOR\ h)p_h$$

Equation 2-27

The projection domain motion transformation that transform LOR in target projection to LOR *i* in reference projection data is derived by summing all possible outcomes from Equation 2-27:

$$p'_i = \sum_h \sum_j \frac{K_{h,j} x_{g,j}}{p_{g,h}} \cdot \delta\left(h\left(\boldsymbol{m'_{h,j}}\right) - i\right) p_{g,h}$$

Equation 2-28

where $\frac{K_{h,j} x_{g,j}}{p_{g,h}}$ is the probability that the event recorded in LOR *h* at gated frame g is from voxel *j*. $\boldsymbol{m'_{h,j}}$ is the component of the motion vector at voxel *j* that is perpendicular to the direction of LOR *h*. The value of $\delta\left(h\left(\boldsymbol{m'_{h,j}}\right) - i\right)$ takes value 1 if and only if the image domain motion at voxel *j* ($\boldsymbol{m'_{h,j}}$) transforms LOR *h* to LOR *i*. Since the activity distribution at frame g $x_{g,j}$ is unknown, an estimator from a scout reconstruction using un-gated projection data was implemented and used in to replace the probability $\frac{K_{h,j} x_{g,j}}{p_{g,h}}$ to derive Equation 2-29

$$p'_i = \sum_h \sum_j \frac{K_{h,j} \hat{x}_j}{\hat{p}_h} \cdot \delta\left(h\left(\boldsymbol{m'_{h,j}}\right) - i\right) p_{g,h}$$

Equation 2-29

where $\hat{p}_h = \sum_j K_{h,j} \hat{x}_j$ is also calculated using the estimated $\hat{x}_j$. The above equation did not consider the interpolation process of the motion transforming process. In actual implementation, AP motion transform illustrated effectively changed the possible value of $\delta\left(h\left(\boldsymbol{m'_{h,j}}\right) - i\right)$ from 0 or 1 to a weighting factor ranging from 0 to 1.

As shown in both Equation 2-29 and Figure 2-35, projection domain transformation is no longer a point-to-point transformation but a point-to-area transformation. The use of approximation is the major contribution of error, but it also effectively avoids the calculation of $\boldsymbol{K}^{-1}$ in Equation 2-13. Thus, for each transformation, only forward projection process is required, which is much faster than reconstruction.

The above approach requires known image domain MVF. In cases where projection domain MVF was known from MEBR, to transform a target projection data to the reference projection data, a much simpler projection domain motion transform was used:

$$\boldsymbol{p}_{ref} = \boldsymbol{p}_{\boldsymbol{target}}(\theta, r + n_\theta)$$

Equation 2-30

In Equation 2-30, n_θ is the estimated projection domain motion, and implementation of 3D MCBR was similar to that of image-domain 2D MCAR.

After motion transformation on the projection domain using either $p'_i = \sum_h \sum_j \frac{K_{h,j} x_{g,j}}{p_{g,h}} \cdot \delta\left(h\left(\boldsymbol{m}'_{\boldsymbol{h,j}}\right) - i\right) p_{g,h}$

Equation 2-28 or its simplified version Equation 2-30, the transformed projection data were summed as shown in Figure 2-30c. Only one reconstruction was required unlike that in MCAR and MCDR to generate dual R&C corrected image. Similar to MCAR and MCDR, the cardiac gated images with motion correction were generated by transforming the reference frame back to individual cardiac gate.

The advantage of motion correction before image reconstruction is that it is not only much faster compared with other methods, but also make it practically possible to correct for intra-frame motion and even allows event-by-event correction using listmode data. The disadvantage is that with the use of the estimated activity distribution, this motion correction method is an approximation.

5. EVALUATION TECHNIQUES

Quantitative evaluation approaches were developed and used in our study to compare the performances of different methods beside visual observation. Both accuracy of motion estimation and image qualities were included in our evaluation. Two sets of evaluation approaches were developed based on known truth (XCAT phantom study) and unknown truth (patient study).

STUDIES WITH KNOWN TRUTH

ROOT MEAN SQUARE ERROR FOR MVF-BASED EVALUATION

To evaluate the estimation accuracy of MVF, root mean square error (RMSE) for MVF was used. The RMSE for MVF inside certain volume of interest (VOI) is defined as:

$$RMSE = \frac{\sqrt{\sum_{VOI} \|\boldsymbol{m}_{Error}\|^2}}{\sum_{VOI} 1},$$

Equation 2-31

where $\boldsymbol{m}_{Error}$ is calculated by vector subtraction of the estimation and truth as shown in Figure 2-37.

The percentage RMSE of the estimated MVF was also calculated and is defined as:

$$Percentage\ RMSE = \sqrt{\frac{\sum_{VOI} \|\boldsymbol{m}_{Error}\|^2}{\sum_{VOI} \|\boldsymbol{m}_{Truth}\|^2}},$$

Equation 2-32

RMSE represents the average length of the error vector in terms of mm, and Percentage RMSE represents the average percentage error.

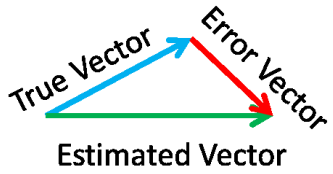

Figure 2-37 Calculation of the error vector.

ROOT MEAN SQUARE ERROR RATIO FOR IMAGE-BASED EVALUATION

Root mean square error ratio RMSER of the image intensity for a certain VOI was calculated to compare overall quantitative accuracy. The definition of RMSER is provided in Equation 2-33, where x_{Est} is the voxel value of the reconstructed image with motion correction, x_{truth} is the voxel value of the same location from actual phantom.

$$RMSER = \frac{\sqrt{\sum_{VOI}(x_{Est} - x_{truth})^2}}{\sum_{VOI} x_{truth}}$$

Equation 2-33

FULL-WIDTH-HALF MAXIMUM OF THE MYOCARDIUM WALL

Full width at half maximum (FWHM) of the myocardium wall (green line in Figure 2-38) was also measured to compare the performance of different methods on reduction of motion blurring effects. To reduce possible influence of image noise, multiple measurements of FWHM were taken.

Figure 2-38 Measurement of myocardium FWHM.

BIAS-NOISE CURVE

Bias-noise curve included the effects of different iteration number in the iterative reconstruction approach. With the increase of iteration number, the image bias is reduced at the cost of increasing image noise. For general imaging purpose, there is no optimum noise-bias point as different tasks may require different bias-noise trade off. In many cases, different methods have different convergence speed, therefore a comparison for single iteration number is insufficient and the comparison of bias-noise curve is required.

In our study, two different definitions of noise and bias were used.

Definition A:

Bias was estimated as the RMSER in the almost noise free case in a certain VOI, while noise was estimated as the standard deviation of the image intensity in a certain VOI over the mean value of the same VOI, i.e. image-based noise estimation.

$$Noise = \frac{1}{\sum_{j\in VOI} x_{Truth}(j)} \sqrt{\sum_{j\in VOI} \left(x(j) - \frac{\sum_{j\in VOI} x(j)}{\sum_{j\in VOI} 1} \right)^2}$$

Equation 2-34

Definition B:

A total of 100 noise realizations were required for this definition. The noise and bias for voxel *j* were calculated by Equation 2-35, i.e. ensemble-based noise estimation. The noise and bias for a certain VOI was calculated by averaging the calculated voxel based bias and noise inside that VOI.

$$\begin{cases} Bias(j) = \left(\sum_{n=1}^{N} x_n(j)/N \right) - x_{Truth}(j) \\ Noise(j) = \frac{1}{x_{Truth}(j)} \sqrt{\sum_{n=1}^{N} (x_n(j) - x_{Mean}(j))^2/N} \end{cases}$$

Equation 2-35

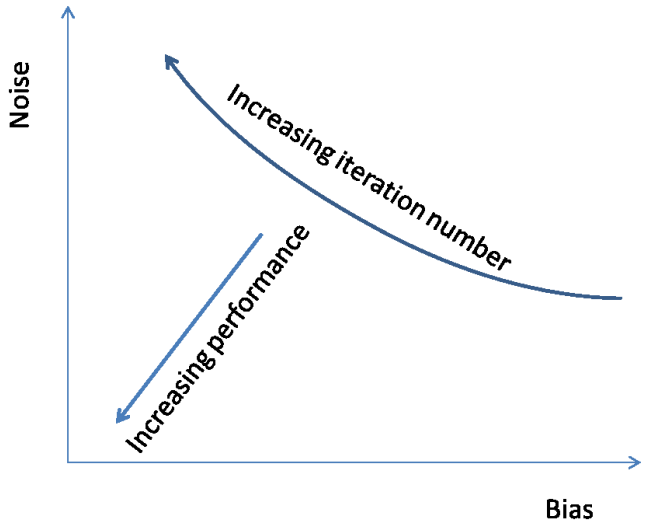

Figure 2-39 A typical look of the bias-noise curve

Definition B is accurate but requires multiple noise realizations, which takes long time to calculate. Definition A is an approximation with the assumption that the voxel value within a certain VOI is uniform and there are no spatial correlations among the voxels, which may not be true. The advantage is that it does not require multiple noise realizations and are easy to calculate.

STUDIES WITHOUT KNOWN TRUTH

DIFFERENCE IN REFERENCE FRAMES.

In cases where true MVF is not available, to evaluate the accuracy of estimated MVF, an indirect comparison of the MVF were used.

Reconstructed image from a certain gate was transformed into the reference image using estimated MVF. Differences among the transformed images were evaluated as an indication of the accuracy of MVF. RMSER and the COM of the heart were used to determine the difference of the images.

The correlation coefficient (CC) is of used in literature [78] to evaluate the performance of motion estimation. CC is defined as:

$$cc = \frac{\sum_i (x_i - X)(y_i - Y)}{\sqrt{\sum_i (x_i - X)^2 \sum_i (y_i - Y)^2}}$$

Equation 2-36

where x_i is the intensity values from the reference frame, while y_i is the intensity values from the target frame transformed using estimated motion. X, Y are the mean value of the image intensity.

Since our target organ is the myocardium, CC was only calculated on the mask region shown in Figure 2-14, as the use of a larger VOI will results in larger CC therefore smaller range to compare different methods.

CC is also very sensitive to noise, to reduce the noise influence, almost noise free simulation data was used to replace the noisy data, and therefore CC was only affected by the inaccuracy of motion estimation from noisy data.

CONTRAST-NOISE CURVE

Contrast-noise curves (Figure 2-40) were used to replace bias-noise curves when no truth is available. Similar to the bias-noise curve, multiple iterations were required to calculate a contrast-noise curve. Image contrast is defined as $(A_m-A_b)/(A_m+A_b)$, where A_m and A_b are the activity levels in a VOI over the myocardium region and a VOI over the blood pool region, respectively. Noise is defined as the standard deviation over mean in the blood pool VOI.

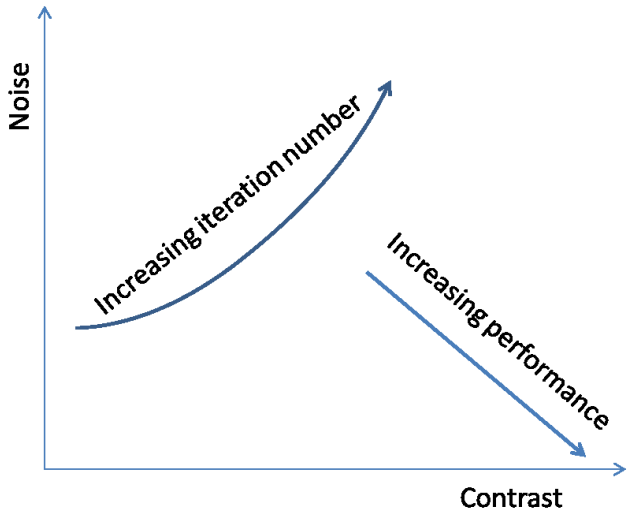

Figure 2-40 A typical look of the contrast-noise curve.

NOISE AT FIXED CONTRAST

Noise at fixed contrast was used to simplify contrast-noise curve. It provided accurate ranking of methods when there was no crosses of contrast-noise curves among different methods. Figure 2-41 shows the noise to contrast plot of two methods. Obviously, Method 2 has better performance than Method 1.

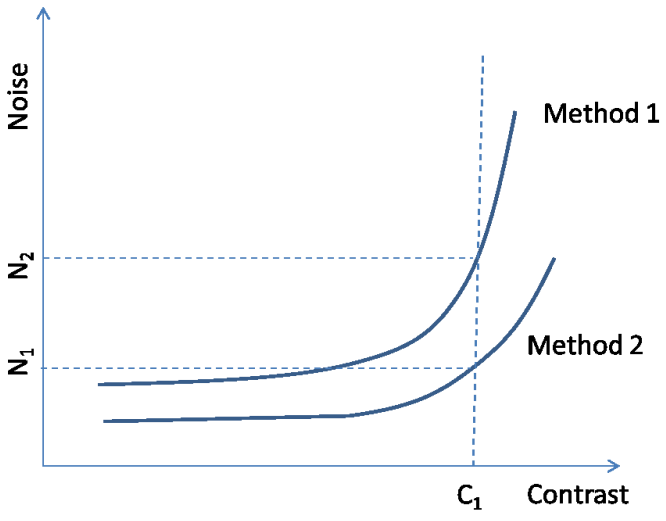

Figure 2-41 Illustration of noise at fixed contrast.

CHAPTER 3. RESULT

1. REALISTIC MONTE CARLO SIMULATION

Uniformity correction was done on the projection data with uniformity map (Figure 2-6c) to eliminate the effects of detector non-uniformity and detector gaps, the corrected sinogram is shown in Figure 3-1(b,d).

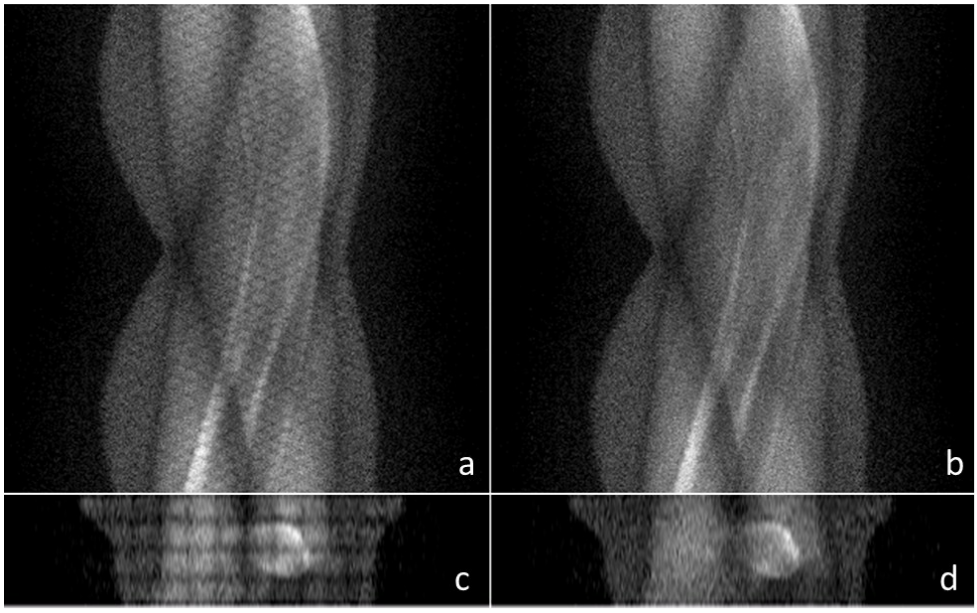

Figure 3-1 4D projection data before (a, c) and after (b, d) uniformity correction.
(a, b) detector bin/angle plane, (c, d) detector bin/z plane. The axis are shown in Figure 1-5.

Dual R&C gating scheme consisted of 6 equal-count amplitude-gates of respiratory motion and 8 equal-time gates of cardiac motion were generated from simulated original projection data, which consisted of 24 equal-time respiratory gates and 48 equal-time cardiac gates. To generate 6 equal-count amplitude gates from the 24 equal-time respiratory gates, the COM of the myocardium region based on Equation 2-3 were measured from the projection data and a gating scheme based on Figure 2-11 were used. The results were shown in Figure 3-2. The resulting dual gated projection data are shown in Figure 3-3 (8 cardiac gates at respiratory gate = 1) and Figure 3-4 (6 respiratory gates at cardiac gate = 1).

Four additional noise levels were generated based on the count level of clinical patient study using the same GE RX scanner. The count levels are shown in Table 3-1, where “center counts” stands for the total counts

in the middle slices across the myocardium region for all angles, segments and gates, and normalized by slice thickness (6.54mm), and "total counts" stands for the summation of all counts from the projection data with axial span of 15 cm. The dual gated projection data of different noise level are shown in Figure 3-5.

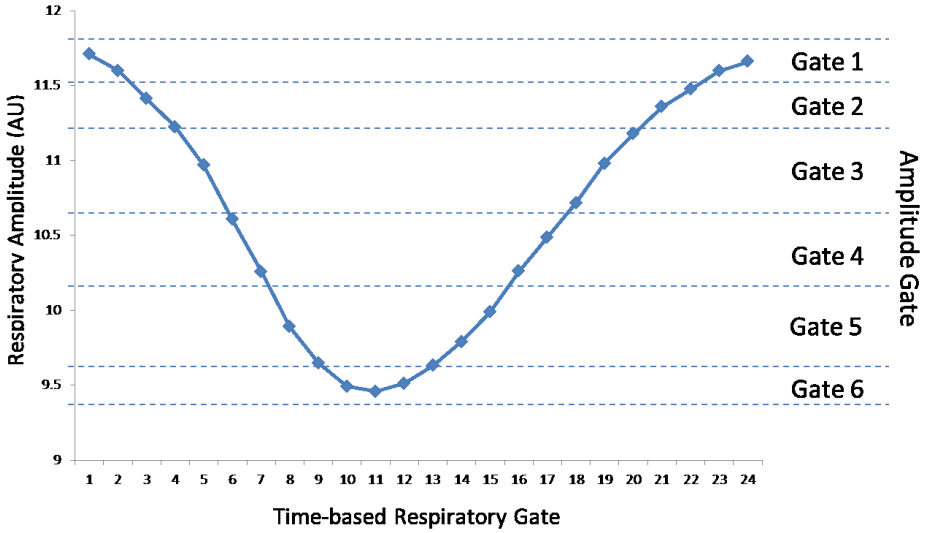

Figure 3-2 Conversion to equal-counts amplitude gating from time-based gating of respiratory motion.

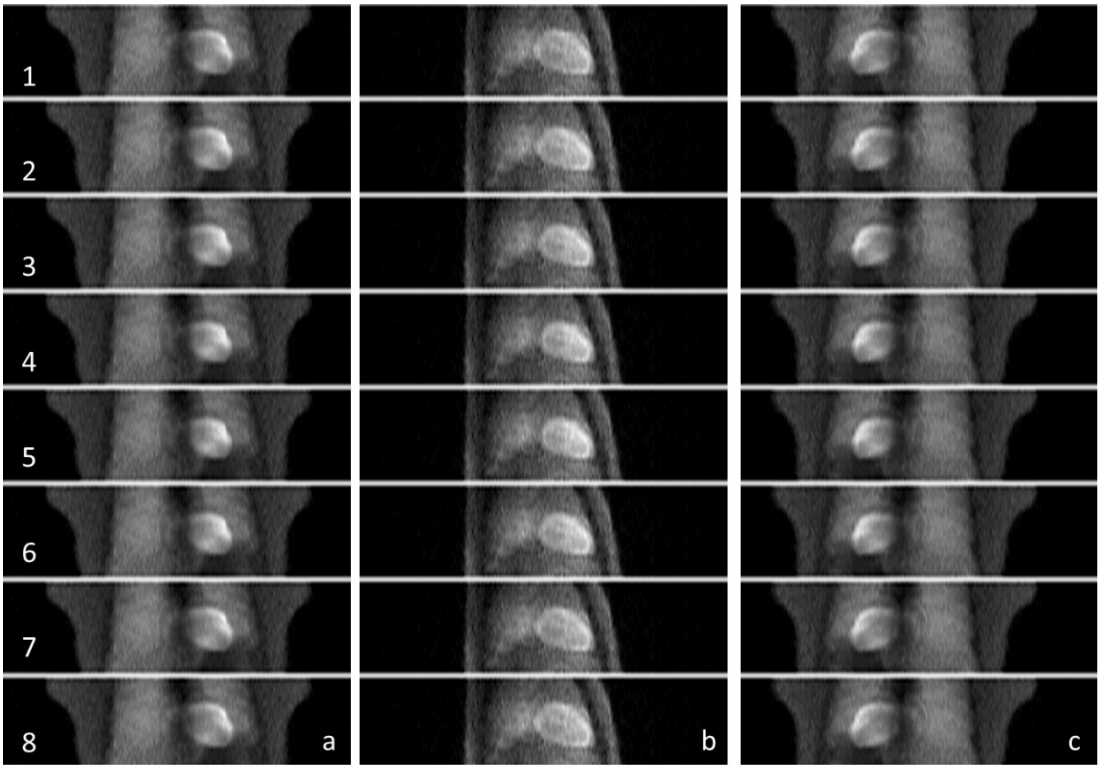

Figure 3-3 Eight Cardiac gated projection data with three different angles.

(a): 0 degree, (b) 90 degree, (c) 180 degree.

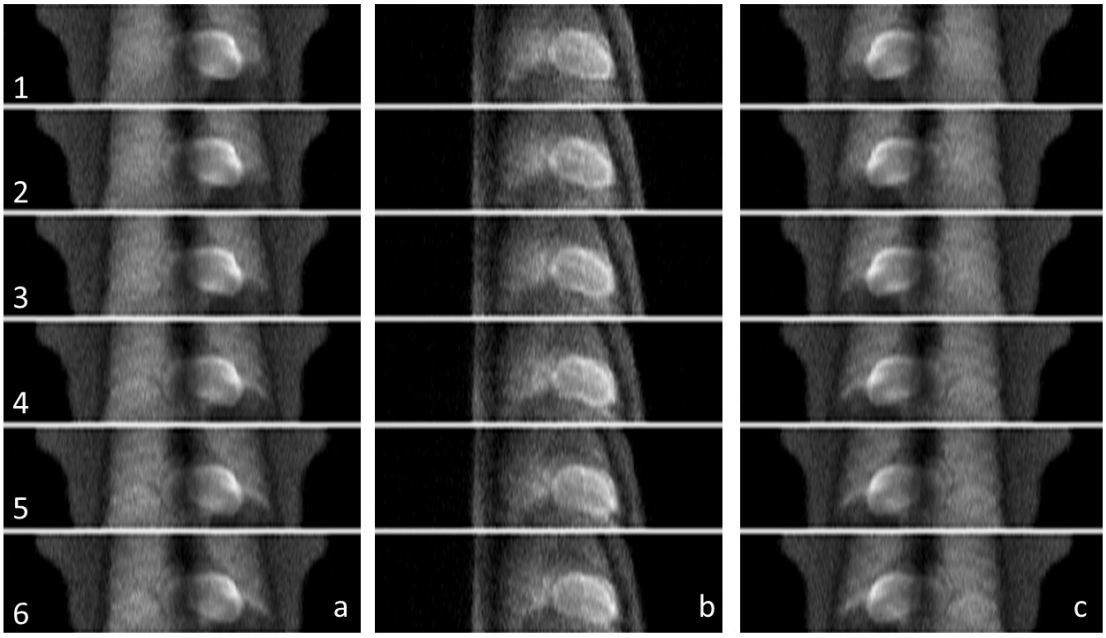

Figure 3-4 Six Respiratory gated projection data with three different angles.

(a): 0 degree, (b) 90 degree, (c) 180 degree.

Table 3-1 Total counts in the center slice for different noise levels.

	Almost noise free	**20 minutes scan**	**10 minutes scan**	**5 minutes scan**	**3 minutes scan**
Center counts (10^3/mm)	--	271	136	68	41
Total counts (10^6)	--	880	440	220	130

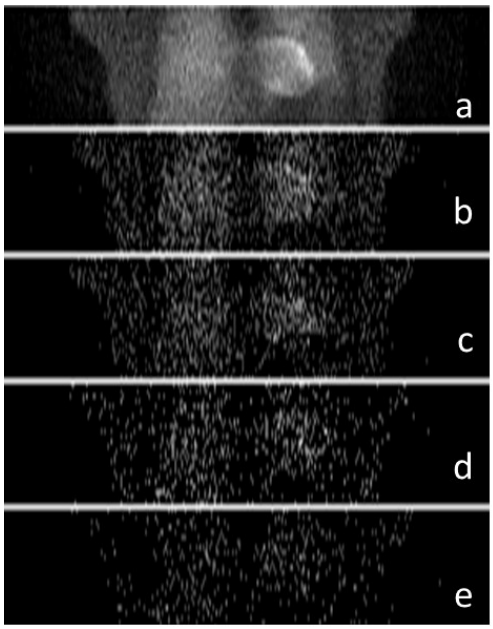

Figure 3-5 Dual gated projection data of five different noise levels.

a), almost noise free, b) 20 minutes scan, c) 10 minutes scan, d) 5 minutes scan, e) 3 minutes scan.

2. GATING TECHNIQUES

DATA-DRIVEN RESPIRATORY GATING

The use of a mask for COM as shown in Figure 2-9 was shown to improve the detection of respiratory signal. Figure 3-6(a) shows in one of the patient cases, the respiratory signal was not visible and was buried with noise when the whole FOV was used for calculation, Figure 3-6(b) shows that with the use of mask, the amplitude of respiratory motion signal was boosted. The reason that a mask was able to improve the detection was that by removing the unnecessary background activity, the contrast of the signal was improved.

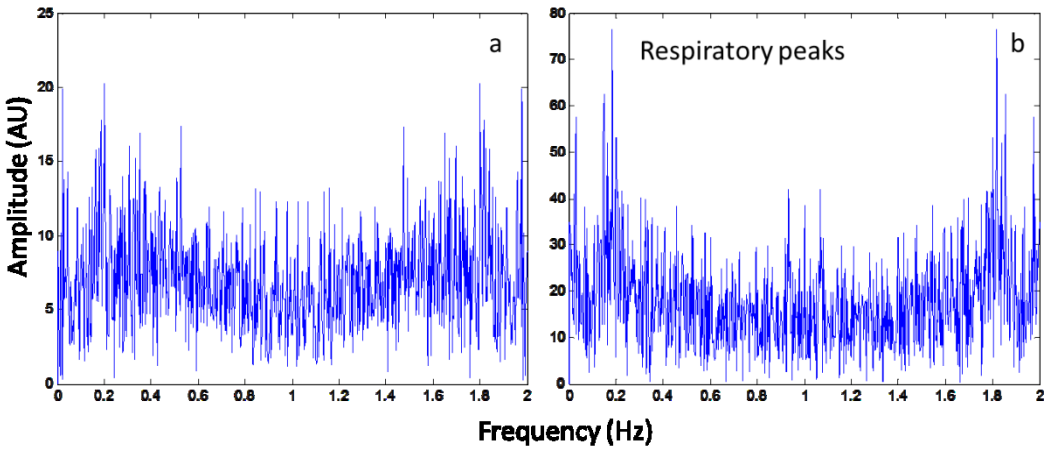

Figure 3-6 Measured center-of-mass signal in frequency domain from a noisy patient scan.

(a) whole FOV was used, (b) only volume within mask was used for measurement.

Even with the use of mask, COM measurement of the respiratory signal was not always working due to extremely low contrast in the myocardium for the PET data (Patient M005, V002, P030, M014, M024, and P008) (Figure 3-7(b)). More sophisticated approaches were developed and to extend the data-driven method for low signal cases. Those methods were not included in this study.

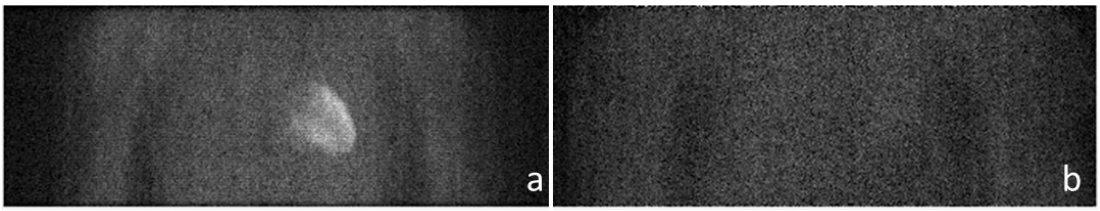

Figure 3-7 Sample patient data used for data-driven respiratory gating .

(a) High myocardium activity (V001), (b) Extremely low myocardium activity (M005), in which case COM measurement was failed.

MRI NAVIGATOR DRIVEN RESPIRATORY GATING

MRI-navigator driven respiratory gating was successfully performed in patient studies with both high myocardium uptakes (Figure 3-7(a)) and low myocardium uptakes (Figure 3-7(b)). The patient data used in this section is listed in Table 3-2. For patient studies with high myocardium uptakes (sinogram contrast >1.7), good match between data-driven method and navigator gating was observed as shown in

Figure 3-8. For patient data with reduced myocardium uptakes (sinogram contrast <1.7), only MRI navigator driven method was applied as PET data-driven respiratory gating failed.

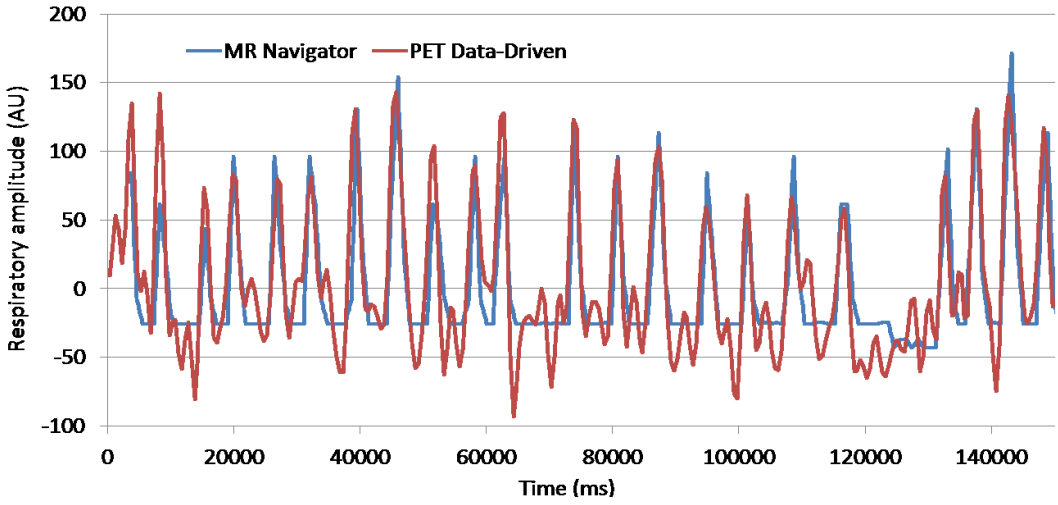

Figure 3-8 Good match between Data-Driven gating and navigator gating for patient P053.

Table 3-2 List of patient used in comparing PET data-driven and MRI navigator gating.

Patient ID	**M005**	**V002**	**P030**	**M024**	**M014**	**P008**	**P053**	**P055**	**M007**	**P057**
Sinogram contrast	1.20	1.30	1.30	1.40	1.48	1.66	1.84	1.87	2.33	2.37
Center counts (1/mm)	77k	56k	30k	18k	55k	45k	44k	45k	20k	46k

Respiratory gating based on MRI navigator was applied on all the patients and data-driven respiratory gating was employed on cases where the sinogram contrast was larger than 1.7. Figure 3-9 shows the respiratory gated reconstructed coronal images for patients with low sinogram contrast using only MRI navigator gating. The patients were ordered from top to bottom with increased sinogram contrast. No attenuation correction was applied as the attenuation map did not contain any motion information. The dash lines were drawn on the upper boundary of the heart region with activity uptake through the first respiratory

gate to the last one in order to demonstrate patient respiratory motion. The respiratory motion can be seen in M024, M014, and P008 where the myocardium uptake was significantly higher than the other. Respiratory gated reconstructed images for patient with high myocardium uptake using both methods are shown in Figure 3-10, in which case similar respiratory motion amplitude were observed in both PET data-driven and MRI navigator methods. 10 iteration was used for reconstructed images shown in Figure 3-9 and Figure 3-10.

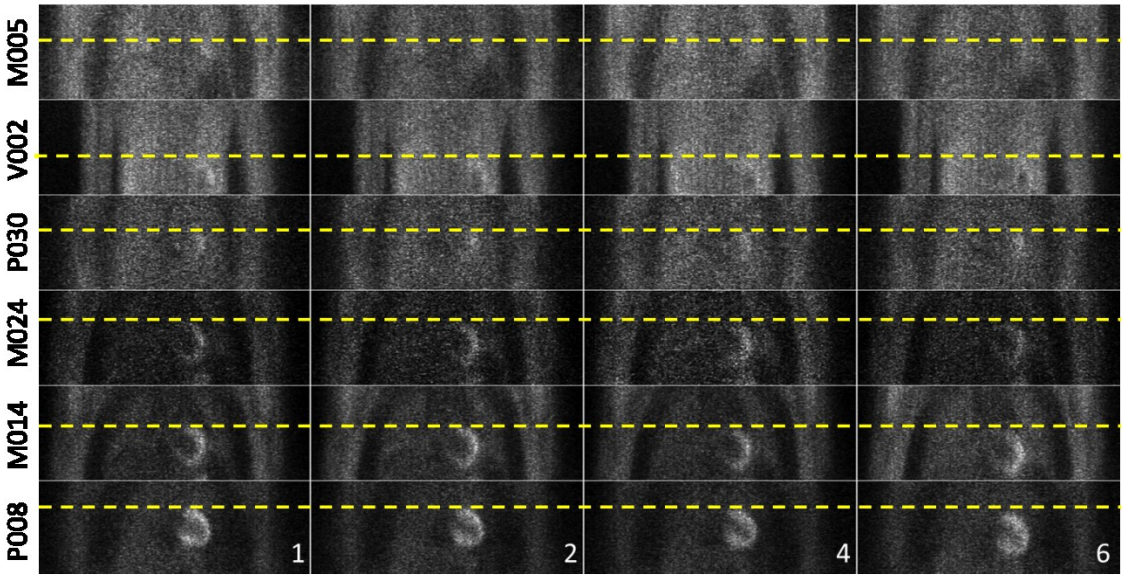

Figure 3-9 Respiratory gated reconstructed images for patients with low myocardium uptakes. From left to right: respiratory gate 1, 2, 4 and 6.

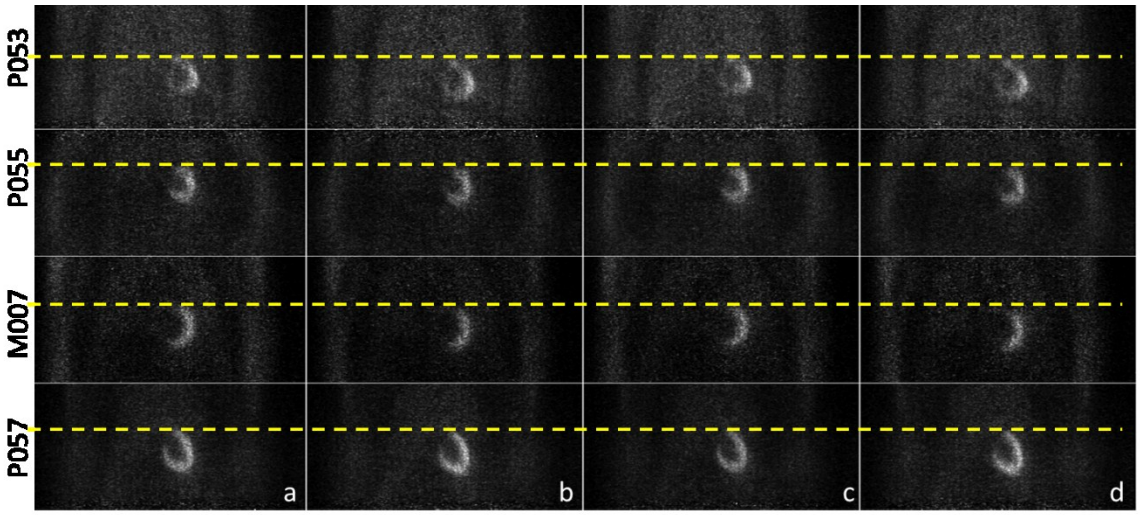

Figure 3-10 Respiratory gated reconstructed images for patients with high myocardium uptakes. a) MRI-navigator based respiratory gate 1 b) MRI-navigator based respiratory gate 6, c) PET data-driven respiratory gate 1 d) PET data-driven respiratory gate 6.

Respiratory and dual R&C motion correction using MEAR and MCAR were applied on patient data to evaluate both PET data-driven gating method and MRI navigator gating method. MEAR failed on patient with extremely low myocardium contrast (<1.35) therefore only 7 patients were used.

Figure 3-11, Figure 3-12, and Figure 3-13 shows the reconstructed cardiac gated images in short axis view for patients P008, M014, and M024, those who had reduced myocardium uptakes with (a) no motion correction, (b) respiratory motion correction only and (c) dual R&C motion correction. It demonstrated the feasibility of using MRI navigator for motion correction when data-driven method failed due to low sinogram contrast. 40 Iteration number was used and no post smoothing filter was applied. Figure 3-13 (patient M024) also demonstrated the worst image quality in terms of contrast and noise level for MEAR and MCAR to work.

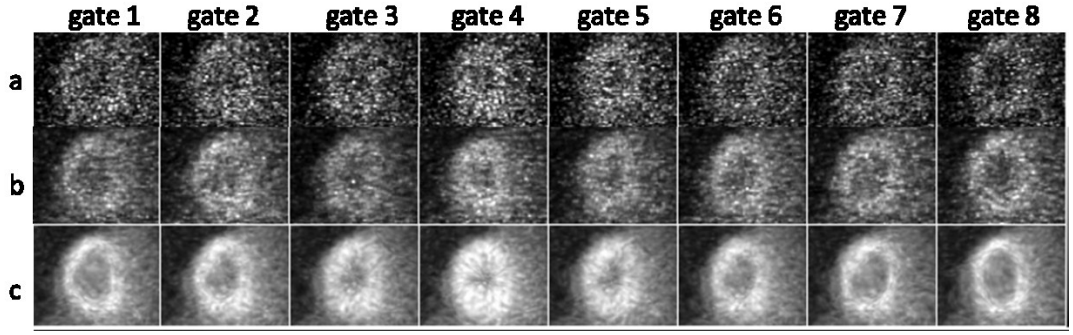

Figure 3-11 Reconstructed cardiac gated for patient P008.

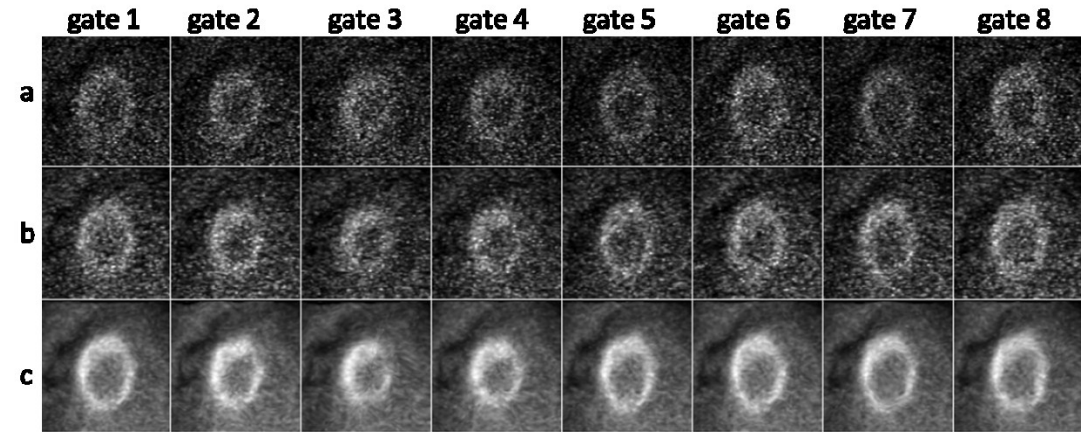

Figure 3-12 Reconstructed cardiac gated for patient M014.

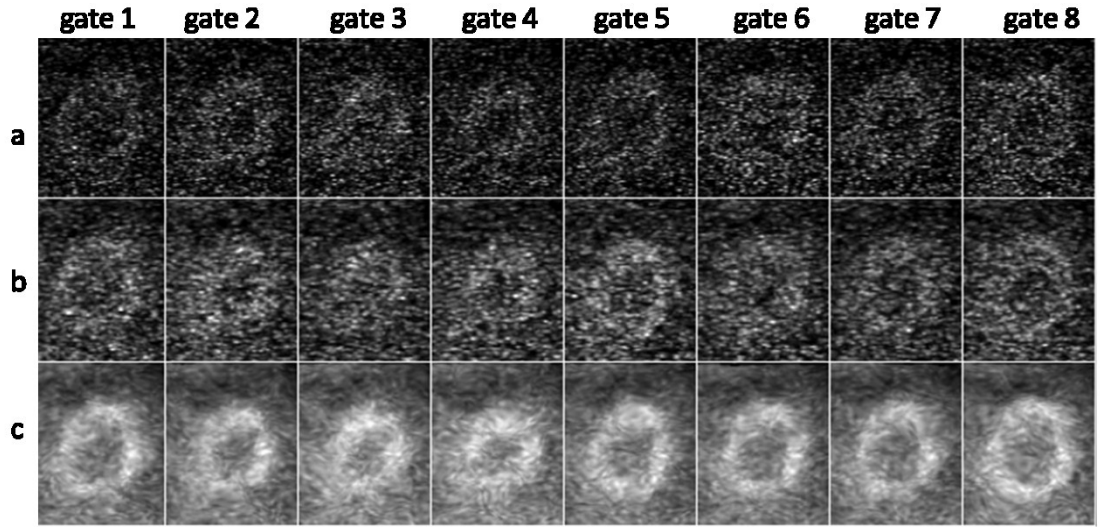

Figure 3-13 Reconstructed cardiac gated for patient M024.

Figure 3-14, Figure 3-15, Figure 3-16, and Figure 3-17 shows the results of reconstructed, cardiac gated images in short axis view using both methods for patient studies with high sinogram contrast. In those images (a) no motion correction, (b) MRI-navigator based respiratory motion correction, (c) PET data-driven based respiratory motion correction, (d) MRI-navigator based dual R&C motion correction, and (d) PET data-driven based dual R&C motion correction were used. The visual difference of using MRI navigator based gating and PET data-driven gating was small.

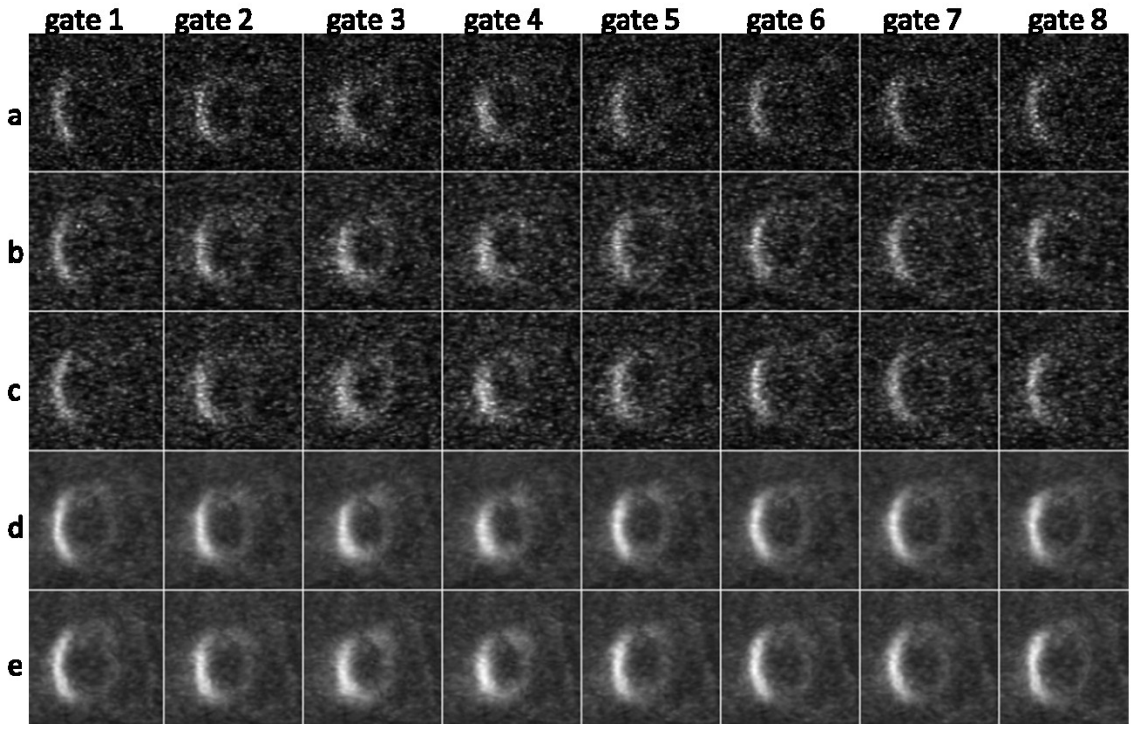

Figure 3-14 Reconstructed cardiac gated images for patient P053.

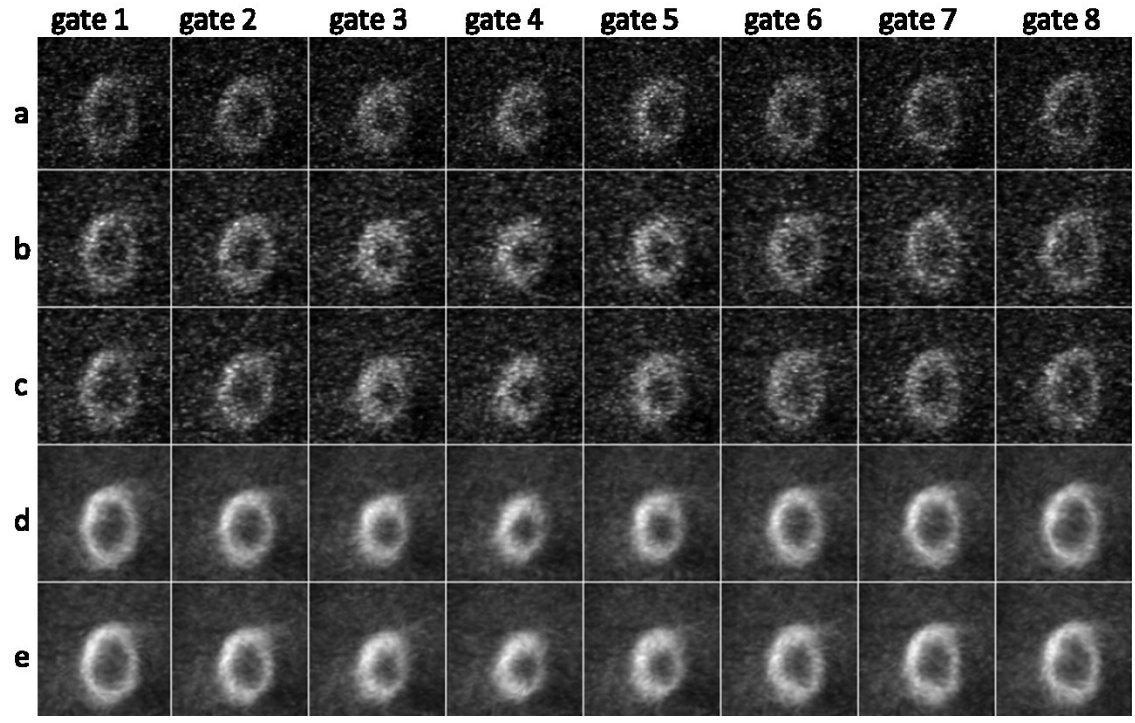

Figure 3-15 Reconstructed cardiac gated images for patient P055.

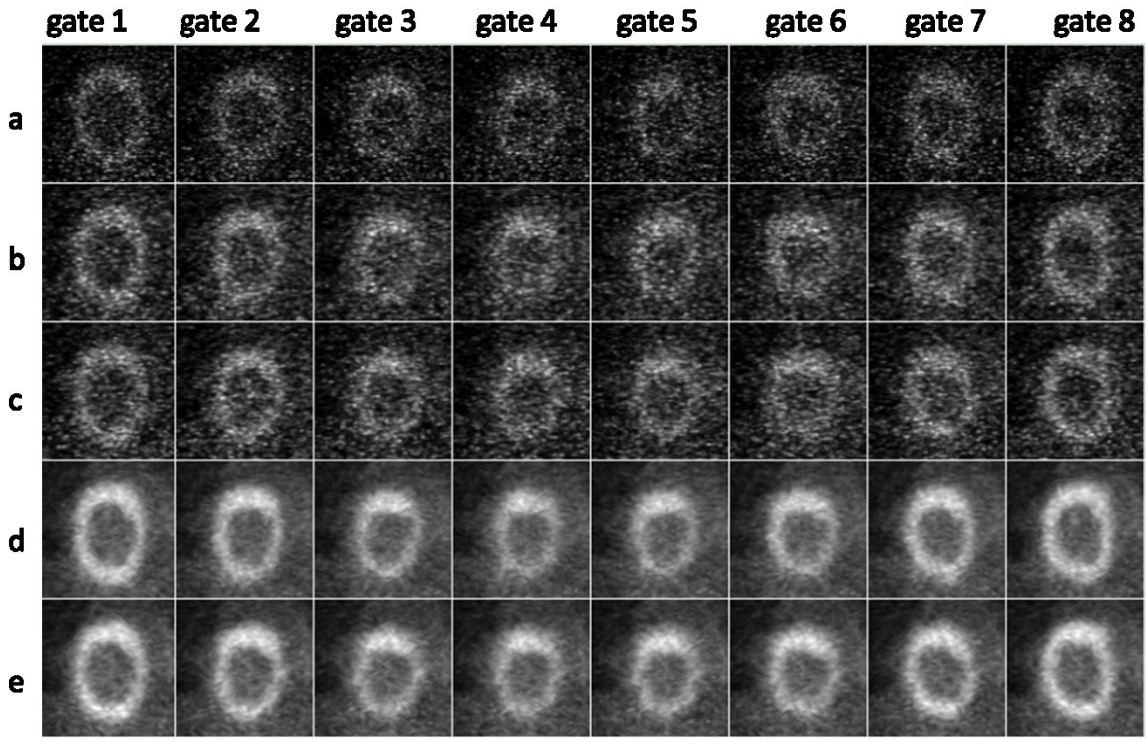

Figure 3-16 Reconstructed cardiac gated images for patient M007.

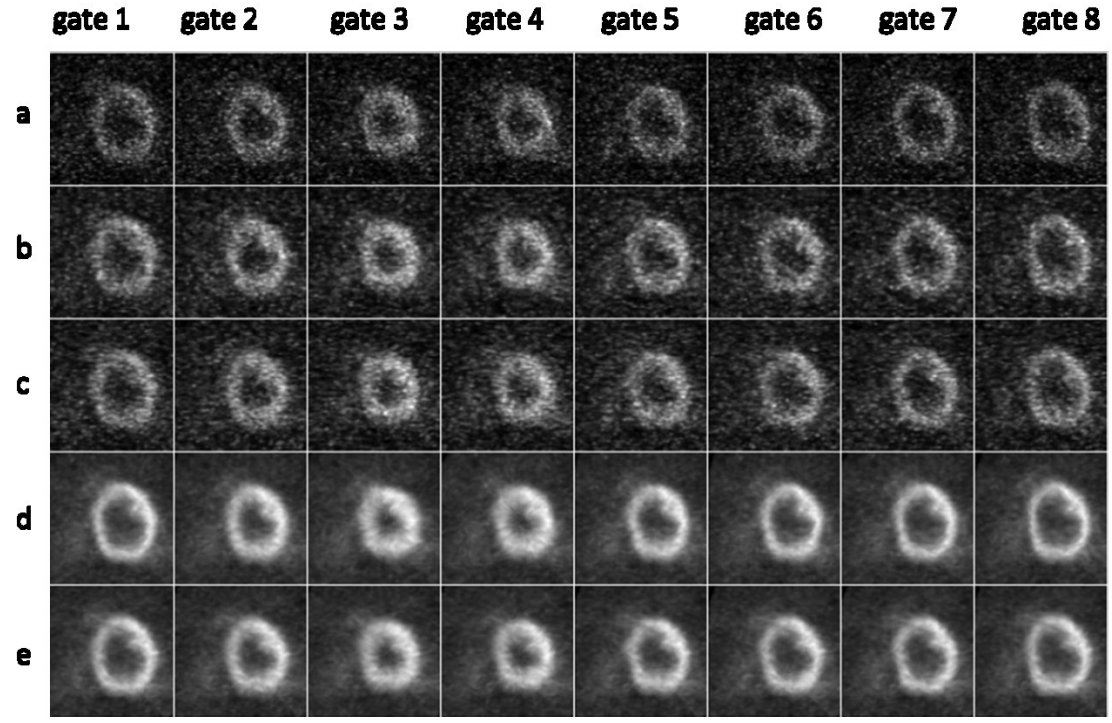

Figure 3-17 Reconstructed cardiac gated images for patient P057.

Contrast-noise curves of the reconstructed images were measured for quantitative evaluation. Figure 3-18 shows a typical example of patient with reduced myocardium update using MRI navigator based gating, in which case the result of using respiratory motion correction outperformed result without, and result with dual R&C motion correction outperformed the other two. Figure 3-19 shows another case where both data-driven gating and MRI navigator gating were used. The performance of data-driven based respiratory and dual R&C motion correction was comparable to those of using MRI navigator, suggesting that in cases when there was high myocardium update in the PET data; both gating approaches were capable for motion correction purpose.

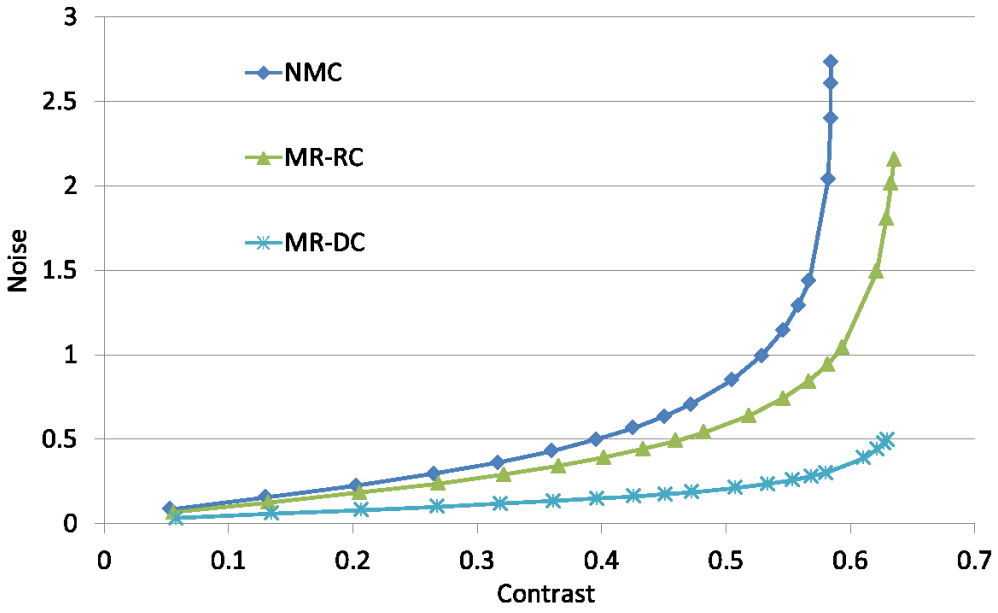

Figure 3-18 Contrast-noise curve for patient M024 with reduce myocardium uptake.

Maximum iteration number for all three methods: 60.

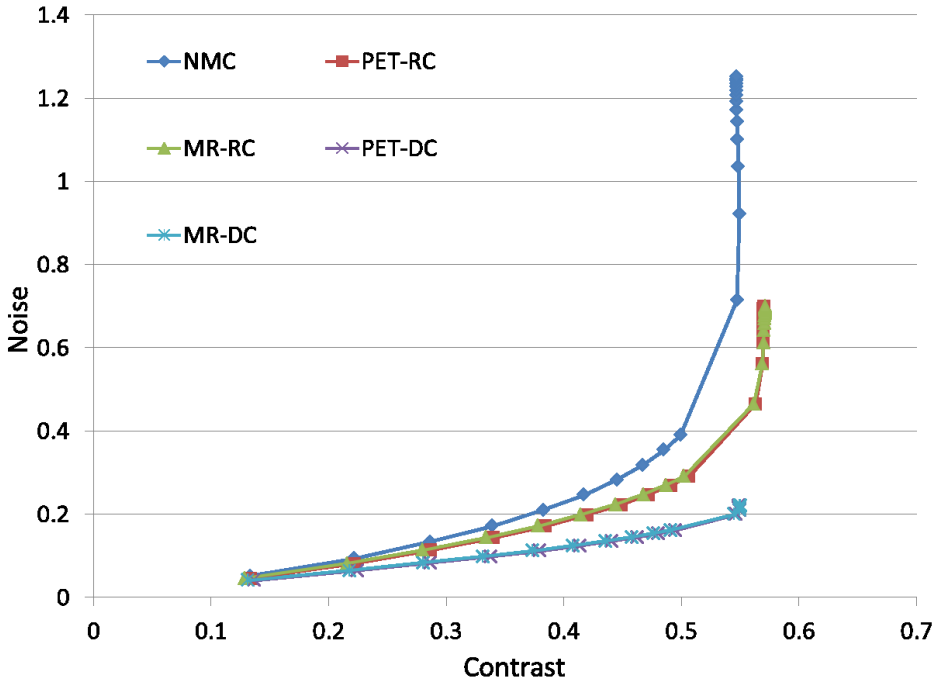

Figure 3-19 Contrast-noise curve for patient with high myocardium uptake.

Maximum iteration number for all five methods: 150.

To further support the above conclusion. Noises at fixed contrast were measured for all patient data. Table 3-3 shows the results of fixed contrast at 50% of the maximum contrast, and Table 3-4 shows the results of fix contrast equals 80% of the maximum contrast. The maximum contrast is the highest contrast level achieved in the contrast-noise curves as shown in Figure 3-18 and Figure 3-19. NMC stands for cases using no motion correction; MRI-RC/PET-RC stands for respiratory motion correction using MRI-navigator/PET data-driven method. MRI-DC/PET-DC stands for dual R&C motion correction using MRI-navigator/PET data-driven method. In both tables, for each patient data, dual R&C motion correction using either MRI-navigator based gating or PET data-driven gating showed consistently the best result, and respiratory motion correction using either MRI-navigator based gating or PET data-driven gating showed reduce noise level compared with result without motion correction. The difference between PET data-driven and MRI navigator was small and insignificant.

Table 3-3 Noise at fixed contrast = 50% maximum.

Patient ID	NMC	MRI-RC	PET-RC	MRI-DC	PET-DC

M014	0.313	0.232	fail	0.101	fail
M024	0.150	0.110	fail	0.064	fail
P008	0.173	0.118	fail	0.071	fail
P053	0.202	0.142	0.138	0.066	0.077
P055	0.200	0.155	0.120	0.099	0.080
M007	0.183	0.132	0.118	0.072	0.070
P057	0.175	0.150	0.146	0.102	0.100

Table 3-4 Noise at fixed contrast = 80% maximum.

Patient ID	NMC	MRI-RC	PET-RC	MRI-DC	PET-DC
M014	0.525	0.347	fail	0.136	fail
M024	0.277	0.196	fail	0.096	fail
P008	0.336	0.193	fail	0.093	fail
P053	0.343	0.238	0.228	0.087	0.106
P055	0.339	0.245	0.179	0.136	0.110
M007	0.335	0.240	0.207	0.105	0.093
P057	0.317	0.246	0.242	0.149	0.147

3. MOTION ESTIMATION TECHNIQUES

MOTION ESTIMATION BASED ON PET DATA

MOTION ESTIMATION AFTER IMAGE RECONSTRUCTION

The performance of four motion estimation methods using 3 different simulated noise levels shown in Table 3-1was evaluated using the percentage RMSE of MVF defined by Equation 2-32 and plot in Figure

3-20. For Method 2, only 2 iterations were used as additional iteration did not further reduce the RMSE. RMSE was averaged in the myocardium VOI and all dual R&C gated frames. It is within expectation that the motion estimation error of all the methods increase with lower counts. Overall speaking, method 4 has the smallest motion estimation error at all three count levels, and method 3 is comparable with Method 4, especially when the noise is increased. Method 1 performs better than Method 2 only in noise-free case; its accuracy degrades significantly as the noise increases. The influence of count level is the most significant for Method 1 than for other methods since each of the 48 dual gated frames in Method 1 has much higher noise than the 8 cardiac frames or 6 respiratory frames used in motion estimation by Method 2~4.

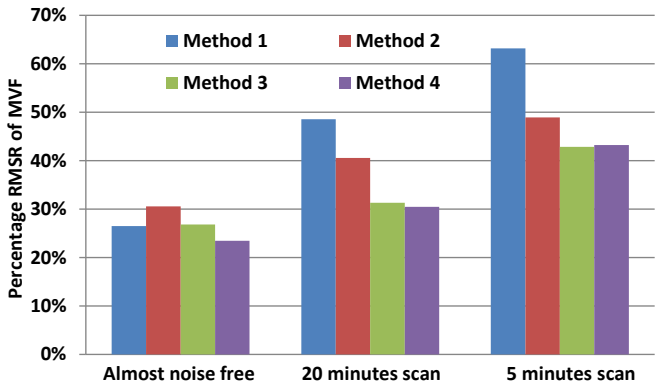

Figure 3-20 The percentage RMSE of dual R&C MVF in myocardium using four motion estimation methods at three different noise levels.

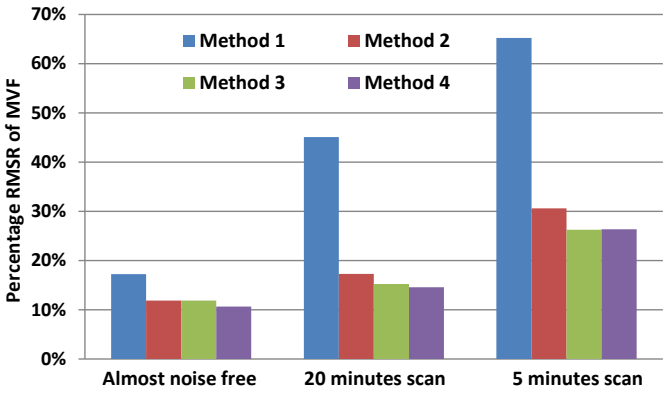

Figure 3-21 The percentage RMSE of respiratory MVF in myocardium using four motion estimation methods at three different noise levels.

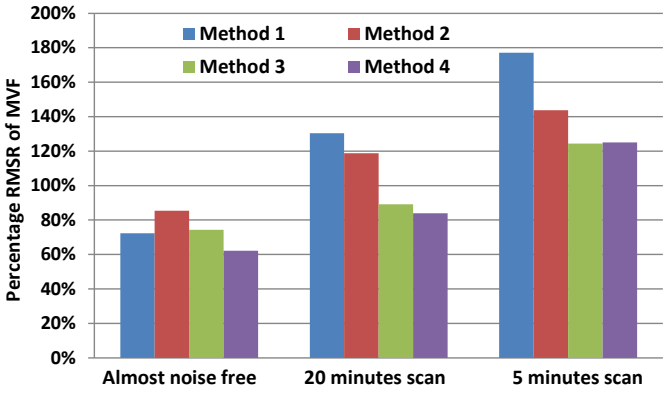

Figure 3-22 The percentage RMSE of cardiac MVF in myocardium using four motion estimation methods at three different noise levels.

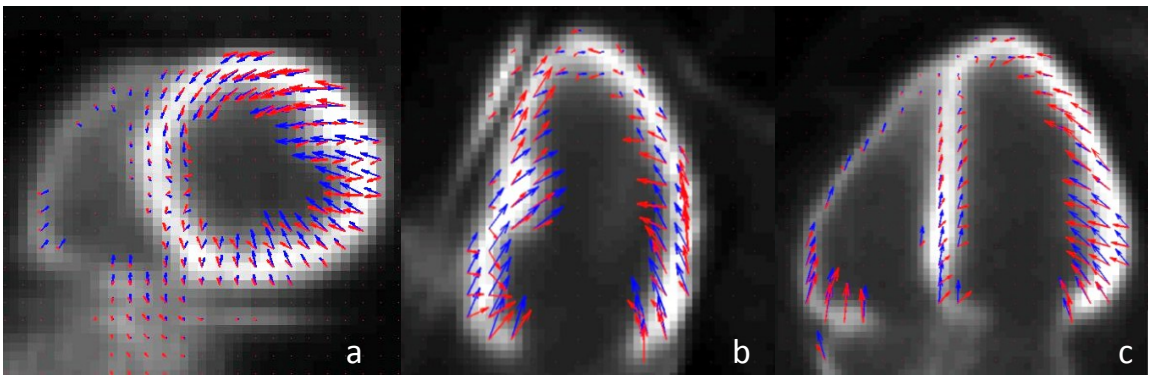

Figure 3-23 The comparison of true MVF (blue) and estimated MVF (red) using Method 3 and almost noise free image data in (a) short axis view. (b) vertical long axis view and (c) horizontal long axis view.

Percentage RMSR of respiratory MVF was calculated from 6 respiratory gates at cardiac gate 1 out of 48 dual gated images. (Figure 3-21) and cardiac MVF (Figure 3-22) was calculated using 8 cardiac gates at respiratory gate 1 out of 48 dual gated images. Same conclusion with the total motion estimation was observed in motion estimation error in respiratory or cardiac motion alone. Although cardiac motion is smaller than respiratory motion in amplitude, estimated cardiac motion had much higher inaccuracy than estimated respiratory motion. Figure 3-23 shows the illustration of estimated cardiac motion (red) and the true motion (blue) from ED to ES using Method 3 with almost noise free reconstructed images at the same respiratory phase. The reason for the inaccuracy is the aperture problem, i.e., the images do not provide any useful information for motion components along the uniform intensity within the myocardium. The motion

estimation algorithm cannot distinguish the longitudinal motion from radio motion and cannot provide accurate estimation of twisting motion, which is consistent with finding from literature.

The regional percentage RMSE of the dual R&C MVF was also calculated and shown in the bull's eye plot in Figure 3-24. The result suggested that Method 2 resulted in larger regional error while Method 1 showed higher global error. The bull's eye plot of the motion estimation error from different methods at different noise level has similar pattern, though the magnitude is different. This indicates that the motion estimation error is closely related to the motion at local region.

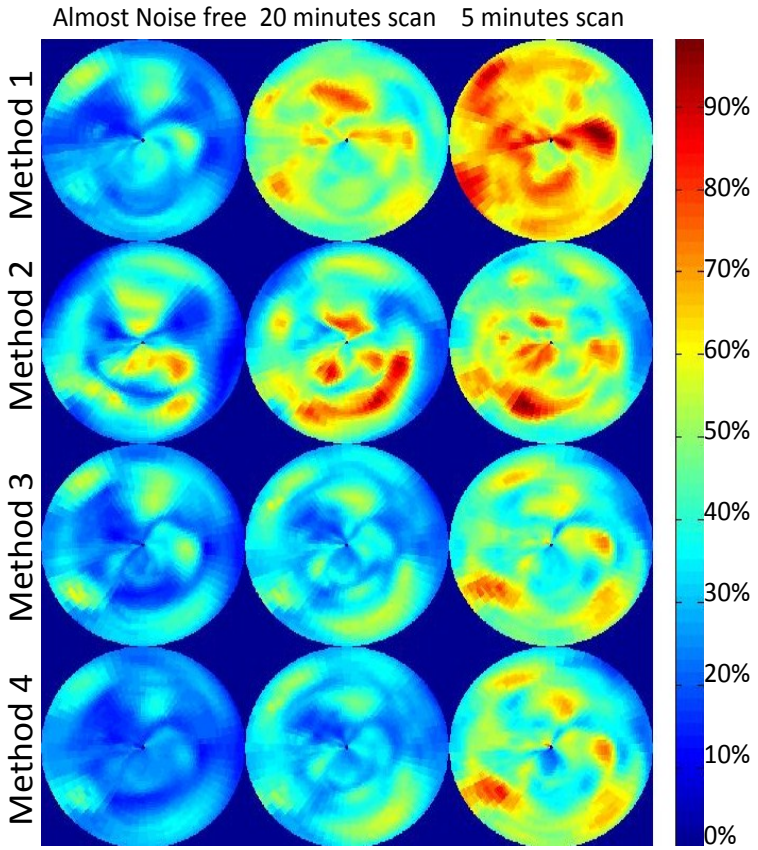

Figure 3-24 . The percentage RMSE of dual R&C MVF in each voxel in the heart plotted in bull's eye plot.

The CC defined in (3) provides another way to evaluate the performance of motion compensation methods. Two different ways of calculating CC were implemented. The first one used the MVF estimated from PET reconstruction images of different noise level to transform the same noisy images, and the CC was calculated between the images before and after transformation. This approach was used in literature as

almost noisy free image was not always available especially in clinical situation. However, with the use of noisy images, it is impossible to distinguish the inaccuracy of motion estimation from the effect of image noise. The second one applied the same MVF estimated from images of different noise levels on almost noise free images, and the CC was calculated between the noise-free images with and without motion compensation. By doing this, the resulting CC value will not be influenced by the contribution of image noise.

Table 3-5 Correlation coefficient using noisy image and estimated MVF.

Estimated MVF	ORIGINAL	Method 1	Method 2	Method 3	Method 4	Truth
Noise Free	0.62	0.96	0.95	0.97	0.97	0.95
20 minutes	0.31	0.57	0.53	0.54	0.54	0.52
5 minutes	0.11	0.24	0.19	0.19	0.19	0.18

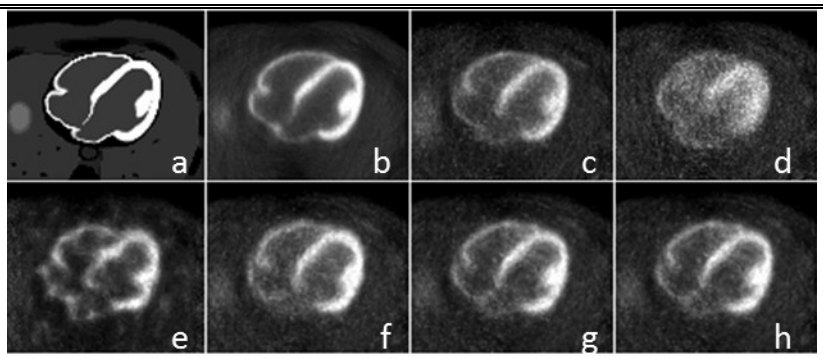

Figure 3-25 Transverse view of the myocardium region using
(a) phantom image (b) reference frame from almost noise free reconstruction, (c-h) averaged noisy reconstructed image after motion transformation using (c) true MVF, (d) no motion transformation (original image), (e) MVF from Method 1, (f) MVF from Method 2, (g), MVF from Method 3, and (h) MVF from Method 4.

The average CC for all dual R&C gated images using the first approach was shown in Table 3-5. The CC of the original reconstructed images without motion transformation was also calculated to demonstrate the improvements of image correlation after applying motion compensation. For comparison, true MVF from XCAT was also used to transform both noisy images and almost noise free image to calculate CC. The results of using almost noise free data suggested that even true MVF did not resulted in perfect match of

images. Possible reason are: 1) The almost noise free simulation data still contain noise as it is impossible to completely remove image noise from Monte Carlo simulations. 2) Reconstructed images have reduced resolution because of partial volume effects while the true MVF was for phantom image without partial volume effects. With the increase of image noise, CC decreased dramatically and all three motion estimation approaches demonstrated improved image correlation when compared with the original gated images without motion compensation. However, unlike the results showed in Figure 3-20, Method 1 demonstrated consistently higher CC in noisy case than the other three methods. Averaged images after motion transformation were generated to explain this phenomenon. Noisy reconstructed images using 5 minutes simulation study were used to demonstrate the effect of image noise on motion estimation. Figure 3-25(e-h) shows the averaged image after transformation using all four methods, the phantom image (Figure 3-25(a)), almost noise free reference frame (Figure 3-25 (b)), averaged after transformation using true MVF (Figure 3-25 (c)), and the original image without motion transformation (Figure 3-25 (d)). Even though Figure 3-25 (e) showed much higher contrast than Figure 3-25 (d), it also showed more severe artifacts than all other methods, which was consistent with Figure 3-20. Figure 3-25 suggested that the reason why Method 1 had higher CC value was because it mistreated noise pattern as real motion. This results suggested that the CC index or similar image motion evaluation methods used in the literature was incapable of evaluating the accuracy of motion estimation.

Table 3-6 Correlation coefficient using almost noise free image and estimated MVF.

Estimated MVF	ORIGINAL	Method 1	Method 2	Method 3	Method 4	Truth
Noise Free	0.62	0.96	0.95	0.97	0.97	0.95
20 minutes	0.62	0.95	0.93	0.96	0.96	0.95
5 minutes	0.62	0.89	0.91	0.95	0.95	0.95

The second approach uses almost noise free image to replace noisy images used in the first approach. The average CC of all dual R&C gated frames using the second approach was shown in Table 3-6. With the reduction of the effects of image noise, it suggested similar ranking orders of all four methods as evaluated with percentage RMSE of the MVF.

Analytical simulations using 4D XCAT phantom were used for the evaluation of MEDR [99]. Due to the computational complexity, only cardiac motion was studied and cardiac gated projections were simulated. No respiratory motion effects were included in the simulation. Both noise free and noisy projections were generated.

Although there was no guarantee of convergence from Equation 2-10, convergence was enforced by decreasing the value of $stepsize$ as shown in Figure 3-26.

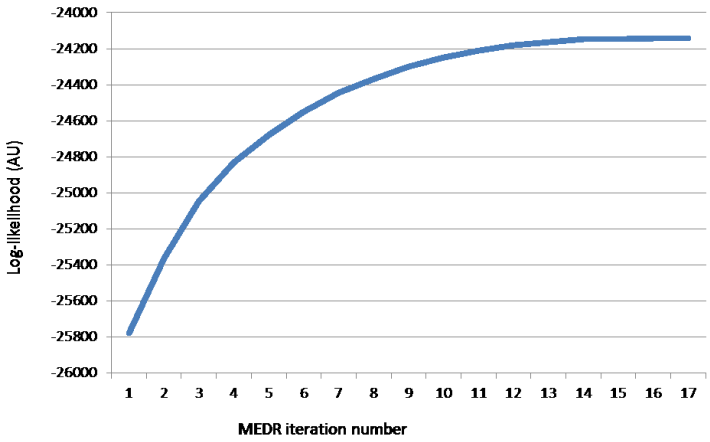

Figure 3-26 Convergence curve of MEDR.

To evaluate the performance of MEDR, image based motion estimation (MEAR) on the same data were performed on the same datasets. Figure 3-27 shows the estimated MVF that transformed the frame end systole to end diastole using noise free data on the myocardium region. Both MEDR and MEAR were used and the resulting 3D MVF were projected on transaxle plane, blue arrow was the MVF from 4D XCAT, used as ground truth, green arrow was the result from MEAR, and red arrow was the results from MEDR. Part of the left ventricle was enlarged for better comparison as shown Figure 3-27b. Estimated MVF using MEDR showed improved accuracy visually.

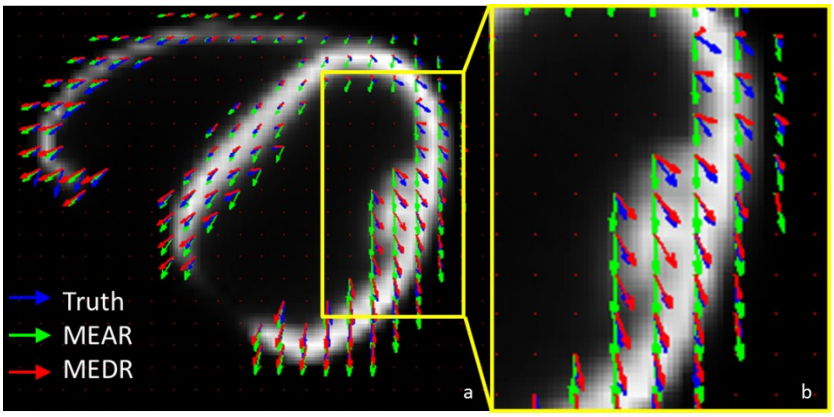

Figure 3-27 MEDR and MEAR from end systole to end diastole, using noise-free projection data.

Noisy simulations were also carried out and Figure 3-28 shows both images before (a) and after correction (b) as well as estimated 3D MVF (c, d). Similar conclusion was observed as Figure 3-27.

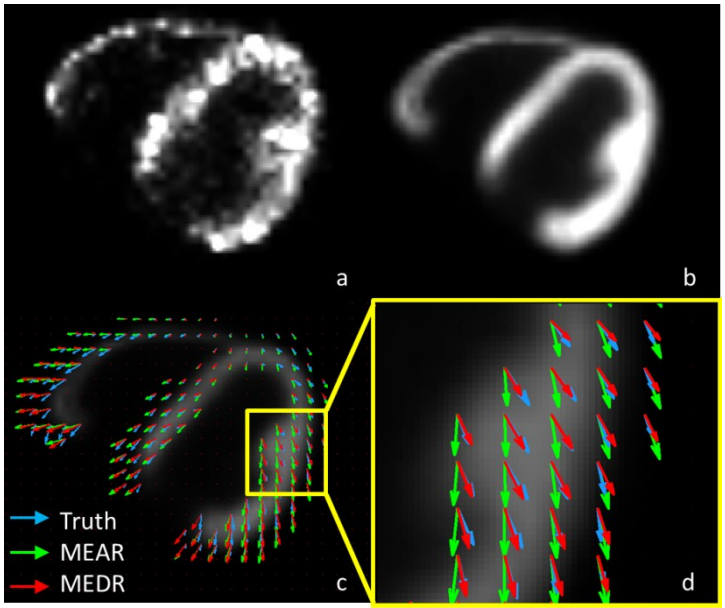

Figure 3-28 Motions estimation from ES to ED using clinical noise level 3D PET projection data. a) cardiac gated image at ED without motion correction, b) cardiac gated image at ED with motion correction, c) estimated 3D MVF using both MEAR and MEDR, d) enlarged region.

Quantitative analysis of the noise simulation using percentage RMSR also indicated that the MEDR had better performance than that of MEAR. The results of percentage RMSR of using all 8 cardiac gates were shown in Figure 3-29, in which case the first cardiac gate was chosen as the reference frame.

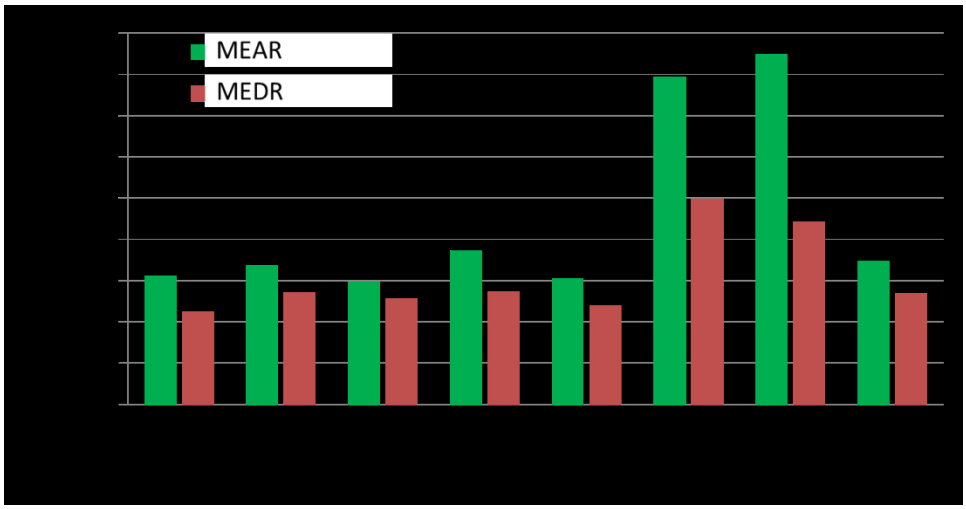

Figure 3-29 Percentage RMSE of 3D MVF estimation from different frames using noisy data.

The percentage RMSR in Figure 3-29 only have the magnitude information, but for vectors, both magnitude, and direction are important. Figure 3-30 shows angle distribution of total percentage RMSR of using noisy data. Angle difference means the angle difference of estimation and true MVF for a certain voxel. Y axis means the normalized percentage RMSR for a certain angle difference. The result suggested that MEDR yielded smaller percentage RMSR than that of MEAR, especially when the deviation angle is large.

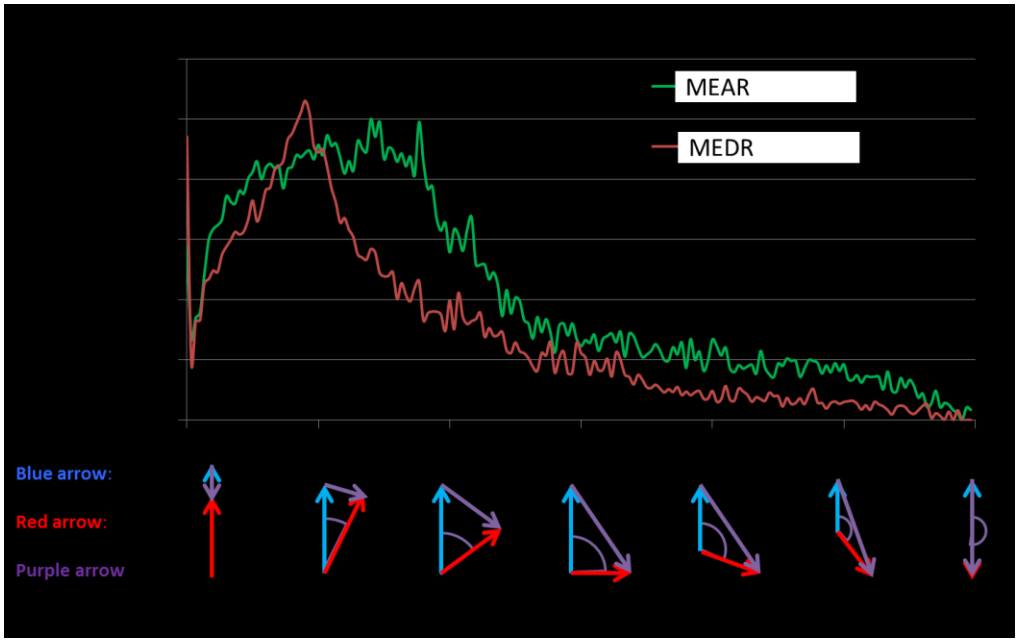

Figure 3-30 Angle distribution of total Percentage RMSE of using noisy data.

MOTION ESTIMATION BEFORE IMAGE RECONSTRUCTION

Using the simplified model in Equation 2-15, respiratory motion estimation using projection data was done on the almost noise-free simulation data. As the result from MEBR was projection domain MVF, a direct comparison with image domain MVF was not available. Therefore indirect comparison of reconstructed images was used to compare with MEAR with respiratory motion. In which case the reconstructed images of using MEBR was generated using the simplified MCBR and images of using MEAR was generated with MCAR. While only one image reconstruction is needed for the combination of MEBR and MCBE, for evaluation purpose, multiple image reconstructions for motion corrected sinograms were done without summing up in the projection domain.

The boundary of live and lung was measured as shown in Figure 3-31. Profiles of motion corrected and uncorrected reconstructed images are shown in Figure 3-32. Results in Figure 3-32(a) and Figure 3-32(b) show that this MEBR reduces the motion blurring effects. Results in Figure 3-32(c) shows that MEBR was comparable with MEAR.

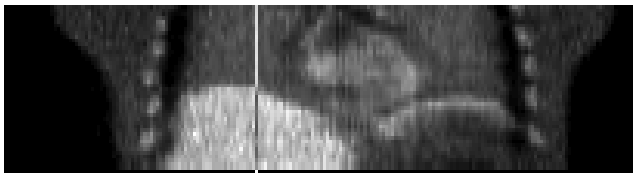

Figure 3-31 Colonial view of the reconstructed image for one respiratory gate.
Profiles along the line were measured for 6 respiratory gates with and without motion correction.

The COM of a VOI around the heart region as shown in Figure 3-33 was measured for each gate without and with motion corrections. The results are shown in Figure 3-34. The relative heart displacement without motion correction measured using COM was ~10 mm. The relative heart displacement using MEBR was ~1mm without the first gate and ~2 mm with the first gate. The relative motion using MEAR was ~1mm. The absolute value of COM was not reliable as the non-moving background was also contributed to the final measurement, but the relative change of COM was able to show that MEBR was able to reduce respiratory motion in the heart region.

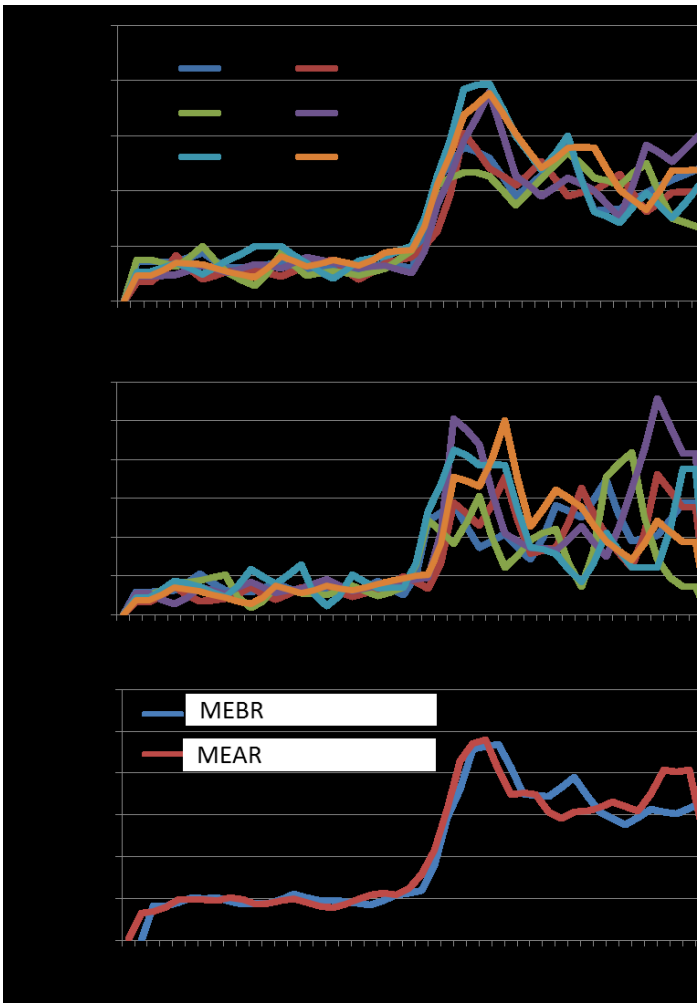

Figure 3-32 Profiles from different respiratory gated frames using (a) without motion correction, (b) motion correction using MEBR, and (c) averaged motion corrected frame using both MEBR and MEAR.

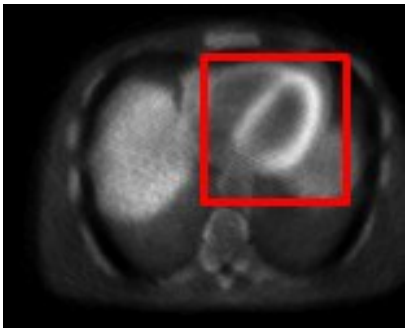

Figure 3-33 3D VOI around the heart used for measuring the change of COM due to respiratory motion. The change of COM among different gates were used as a quantitative measurement for respiratory motion and the effects of correction.

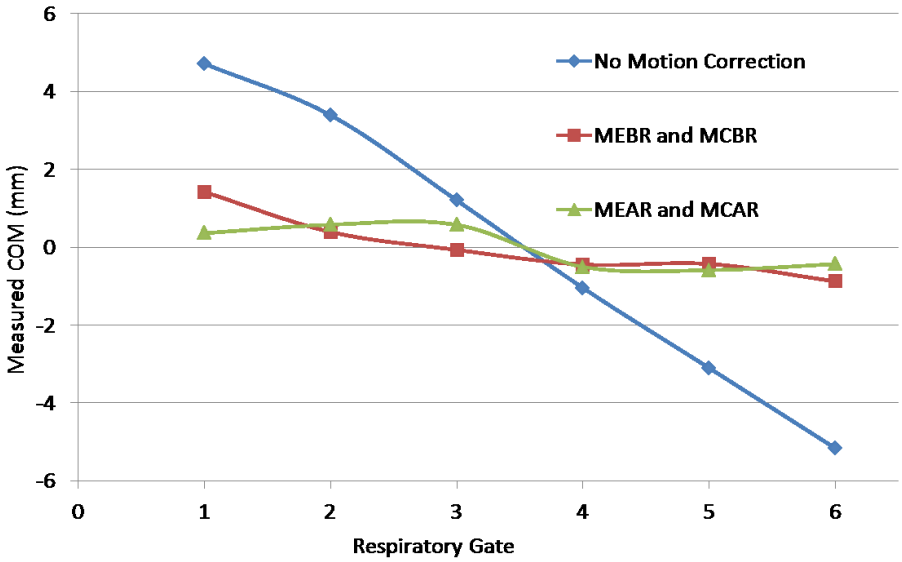

Figure 3-34 The relative motion along vertical axis measured using the COM of the heart region. Motion along vertical axis is a main component of the respiratory motion and was used for measuring the magnitude of respiratory motion.

MOTION ESTIMATION BASED ON OTHER MODALITIES

MOTION ESTIMATION FROM SIMULTANEOUSLY PET/MRI

MOTION ESTIMATION FROM MRI NAVIGATOR

One dimensional affine respiratory estimated from MRI navigator was used for respiratory motion correction. To evaluate this method, MCAR using both respiratory motion from 1D MRI navigator (NAV) and MEAR was applied on the patients list shown in Table 3-2. MRI navigator based gating was used for both methods. For patient with extremely low sinogram contrast (sinogram contrast < 1.35), MEAR failed due to extremely low signal. Figure 3-35 shows a sample reconstructed images using both estimated motion as well as the original data without motion correction (NMC). No cardiac gating or cardiac motion correction was applied. The image differences were not visually significant. Contrast-noise curves were

also calculated for the same patient and Figure 3-36 shows the curves from one patient, in which case images using MEAR outperformed images using motion from navigator.

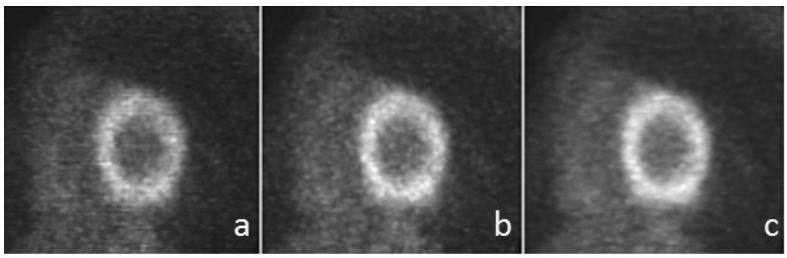

Figure 3-35 Short axis view for patient P057 without cardiac gating and cardiac motion correction a) No motion correction, b) respiratory motion correction using motion from navigator, c) respiratory motion correction using MEAR from PET images.

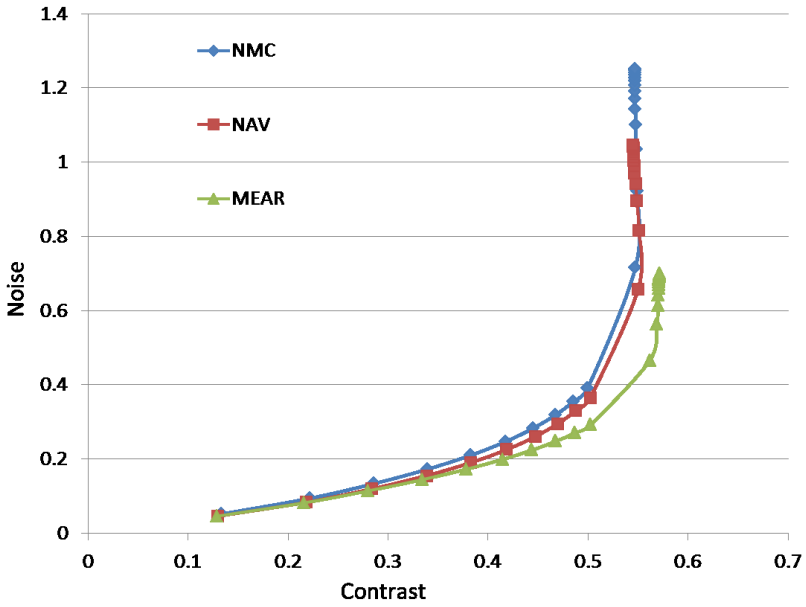

Figure 3-36 Contrast-noise curve for comparing navigator based motion and MEAR

Noises at fixed contrast were calculated as well. Table 3-7 shows the results for contrast at 50% maximum and Table 3-8 shows the results for contrast at 80% maximum. Results showed that both methods reduced noise than that without motion correction, and when the sinogram contrast was high, MEAR consistently outperformed 1D motion from navigator. However, for patients with low sinogram contrast, MEAR failed to work and motion from 1D navigator provided a viable option for improving signal or decreasing noise.

Table 3-7 Noise at fixed contrast = 50% maximum.

Patient ID	M005	V002	P030	M014	M024	P008	P053	P055	M007	P057
NMC	0.136	0.241	0.407	0.313	0.150	0.173	0.202	0.200	0.183	0.175
NAV	0.113	0.221	0.326	0.262	0.133	0.140	0.177	0.195	0.164	0.158
MEAR	fail	fail	fail	0.232	0.110	0.118	0.142	0.155	0.132	0.150

Table 3-8 Noise at fixed contrast = 80% maximum.

Patient ID	M005	V002	P030	M014	M024	P008	P053	P055	M007	P057
NMC	0.271	0.339	0.639	0.525	0.277	0.336	0.343	0.339	0.335	0.317
NAV	0.217	0.320	0.485	0.393	0.247	0.231	0.303	0.326	0.314	0.290
MEAR	fail	fail	fail	0.347	0.196	0.193	0.238	0.245	0.240	0.246

TRUE MOTION FROM XCAT

Dual R&C motion from 4D XCAT was used as true MVF and best possible estimated motion. However, as the resolution of simulated PET data is much worse than 4D XCAT phantom. To study the effects of resolution mismatch, MCDR without activity-preserving motion transform using both original 4D XCAT MVF and smoothed MVF were applied on almost noise free simulation data, and Figure 3-37 shows the short axis view of the motion corrected images using both original MVF and smoothed MVF compared with phantom image. 120 iterations with 1 subset were used in the reconstruction methods in Figure 3-37. The over-sharpness of the papillary muscle can be seen in the red circle in the original MVF but not the smoothed MVF, and is caused by the resolution mis-match of MVF and activity distribution.

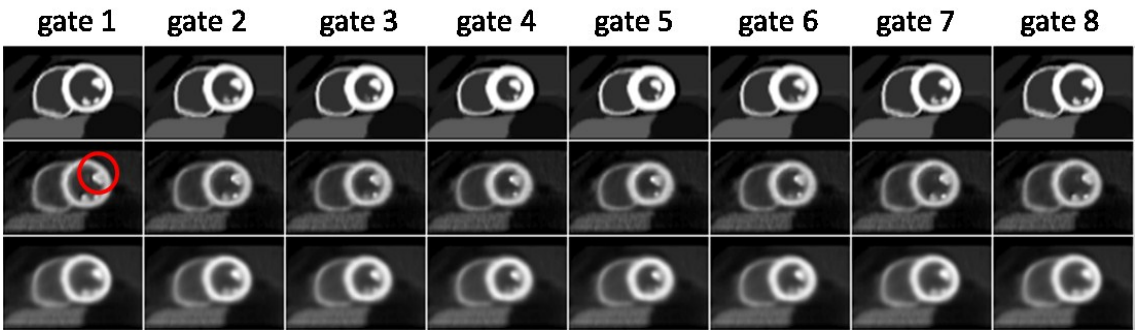

Figure 3-37 MCDR using original 4D XCAT MVF (second row) and smoothed 4DXCAT MVF (Third row) compared with the original phantom (first row).

The resolution mis-match artifacts shown in Figure 3-37 is only obvious in high update number. A study of using different iteration number is shown in Figure 3-38. The resolution mis-match started to show up at iteration 40, which is often used in clinical situations. The results of using smoothed MVF from 4DXCAT for multiple iteration number is shown in Figure 3-39; no resolution mis-match artifact was present in any of the iteration numbers.

The results suggested that in cases where patient motion with better resolution can be acquired using other system such as MRI, additional low pass filtering may be necessary to reduce artifacts caused by resolution mismatch. The smoothed R&C MVF from 4D XCAT is used as the true MVF in this work unless otherwise noted.

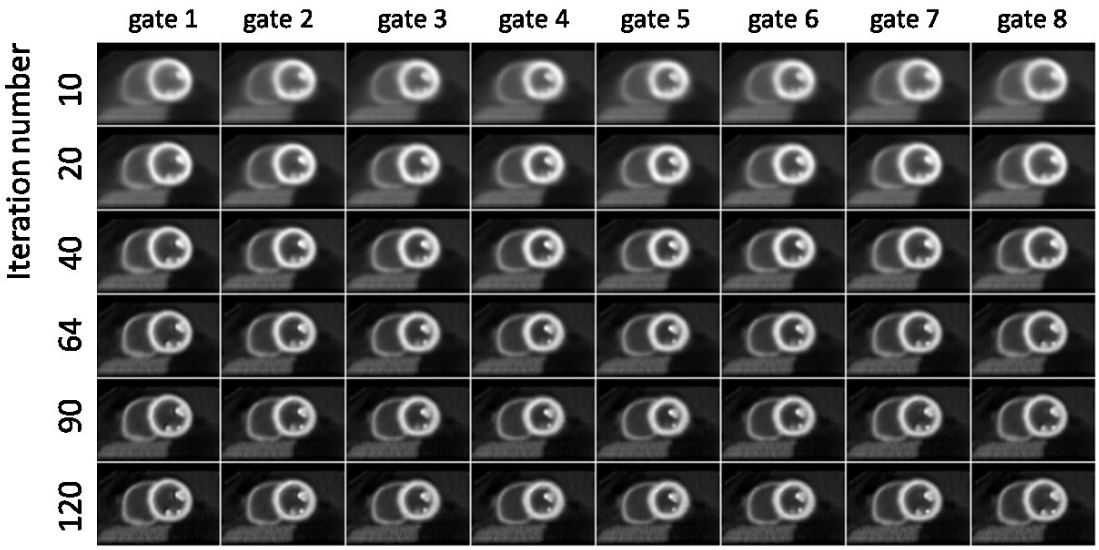

Figure 3-38 Cardiac gated images of multiple iteration using R&C MCDR with unsmoothed MVF from 4D XCAT.

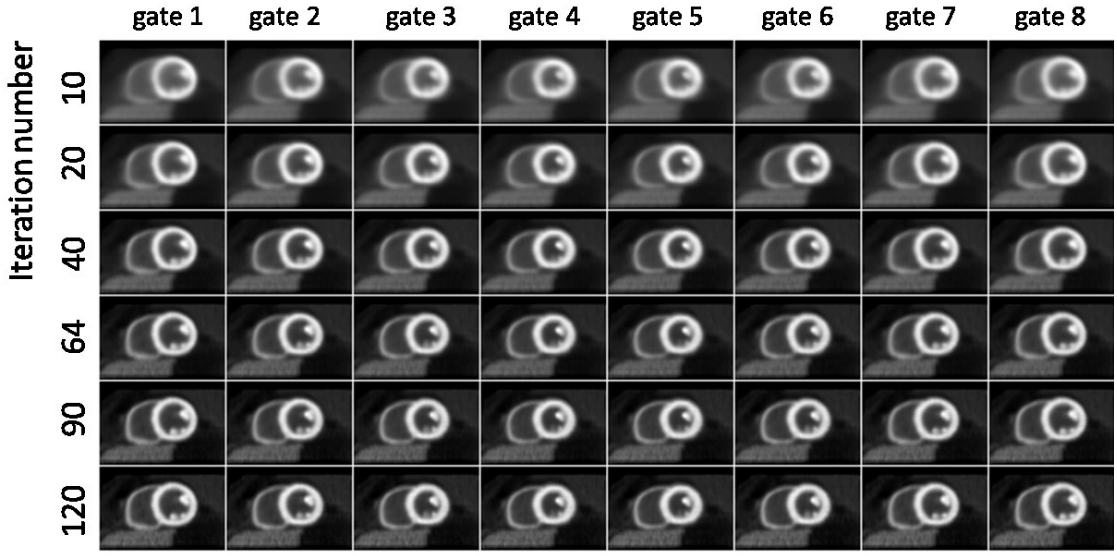

Figure 3-39 Cardiac gated images of multiple iteration using R&C MCDR with smoothed MVF from 4D XCAT.

4. MOTION CORRECTION TECHNIQUES

DUAL R&C MOTION CORRECTION DURING RECONSTRUCTION

In this section, results of using transpose motion transform and inverse motion approximations were studied, the effects of using activity-preserving and non-activity preserving models were also included in this section.

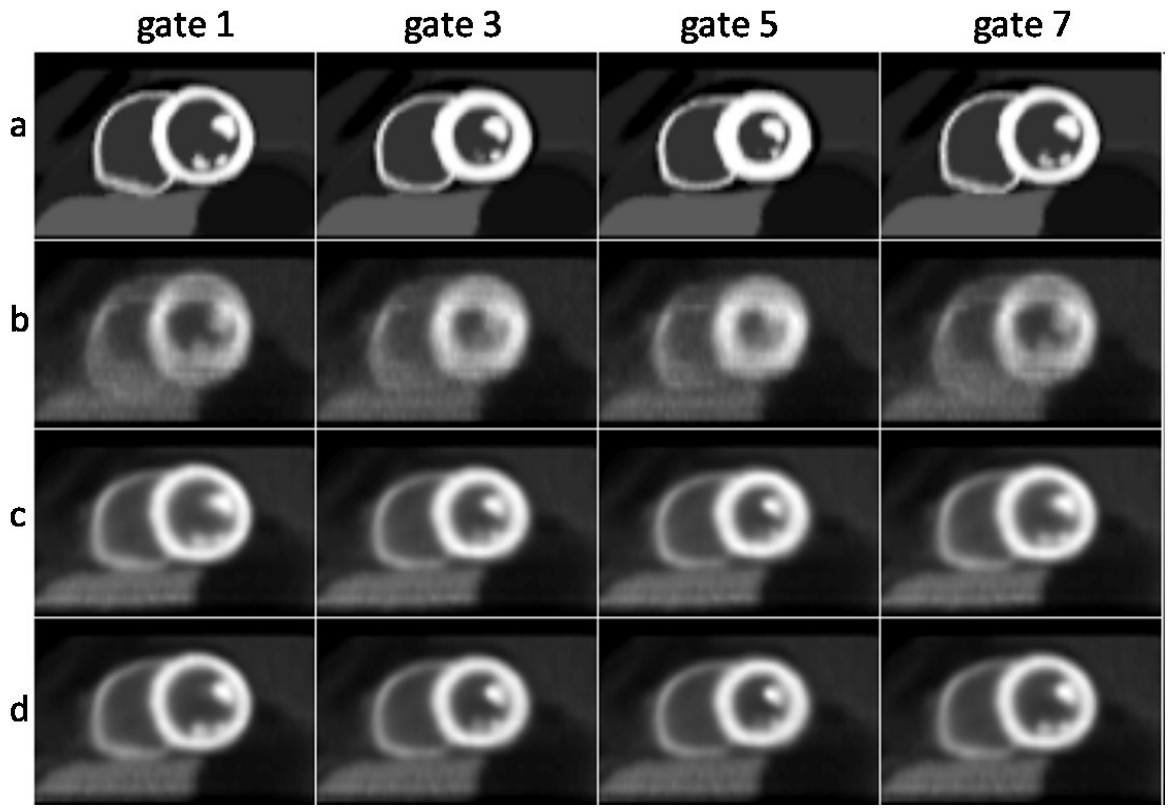

Figure 3-40 Sample short axis view of the cardiac gated images of using different reconstruction methods. 4 out of 8 cardiac gates are shown in this figure. a) 4D XCAT phantom, and almost noise-free reconstructed images from the same short-axis image slice with b) without motion correction, c) with dual R&C MCDR with inverse motion transform, and d) with dual R&C MCDR with transpose motion transform.

Dual R&C MCDR (Equation 2-18) with non-activity preserving image transformation (Equation 2-23) of using transpose motion transform (MCDR transpose) and inverse motion transform approximation (MCDR inverse) was studied. Same true MVF with reduced resolution as well as noise free simulation data were used for both methods. The reconstructed images using both MCDR approaches and image without motion correction are shown in Figure 3-40, in which case 40 iterations were used for all three methods. While both MCDR transpose and MCDR inverse showed significant improvement of image quality by reducing respiratory motion, MCDR transpose showed slightly better sharpness than that of using MCDR inverse. Quantitative results of the relationship of FWHM and RMSER are also shown in Figure 3-41. The uses of transpose motion transform demonstrated superior resolution performance as well as smaller RMSER for

different number of iterations. However, it should be also noted that when inverse motion transform was used with MVF with superior resolution, its inferior resolution performance reduced resolution mismatch artifacts, which resulted in improved image quality. In the following section, MCDR transpose is used unless otherwise specified.

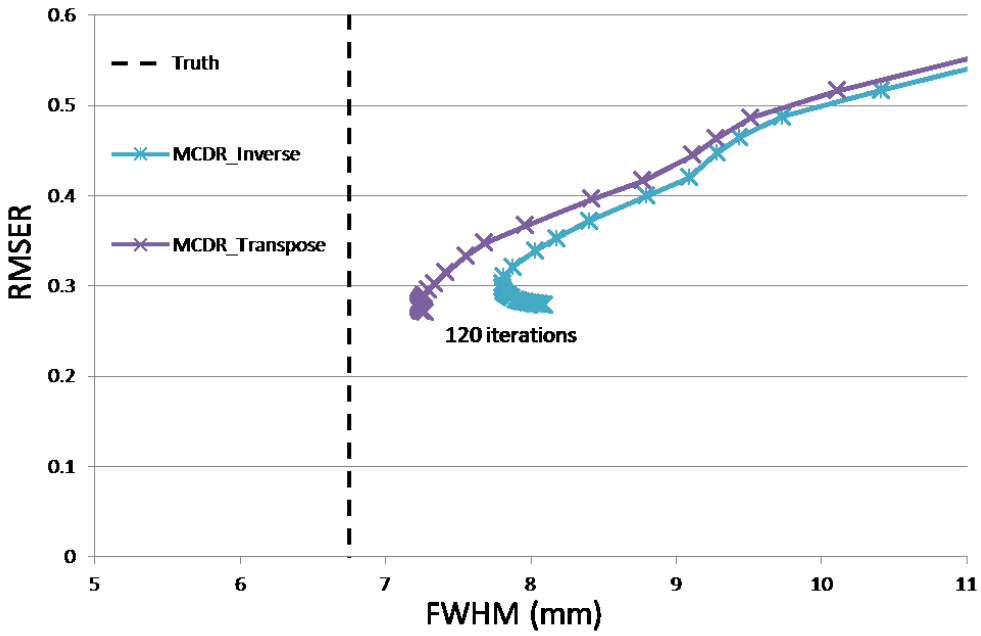

Figure 3-41 RMSER and measured FWHM across the myocardium wall at different iteration numbers Results of using MCDR with inverse approximation (MCDR_Inverse) and MCDR using accurate implementation of transpose motion transform (MCDR_Transpose) with maximum of 120 iterations were included.

Non-activity-preserving motion transform does not preserve the total count, but the value of individual voxel does not change either during image transformation. Activity preserving motion transform preserves the total count of certain region, such as the total counts in the myocardium during a cardiac cycle. Both activity preserving motion transform and non-activity preserving motion transform were studied using MCDR approach with almost noise free data and true motion vector fields from 4D XCAT. The results are shown in Figure 3-42b (non-activity preserving) and Figure 3-42c (activity preserving). Unlike non-activity preserving motion transform, activity preserving motion transform resulted in the change of activity level in the myocardium, which caused a "blinking" effect in the beating heart, as shown in Figure 3-43. The

change of activity level was not observed in non-activity preserving motion transform. Study using simulations with uptakes only present in myocardium to eliminate the possible effects of partial volume were carried out. The calculated total activity in reconstructed image with myocardium being the only uptake across different cardiac gates is show in Figure 3-44. The results suggested that activity preserving model did not change the total activity in myocardium for different cardiac gates but non-activity preserving model did. Thus the cause of the blinking effect is likely to be partial volume effects, as the thickness of myocardium wall changes as the heartbeat.

As suggested in Equation 2-21 and Equation 2-22. The calculation of the transpose motion transform for non-activity preserving transform turns out to be the same as the activity preserving inverse motion transform. The inverse motion transform for non-activity preserving transform is the same as the transpose motion transform in activity preserving scheme. Therefore, MCDR using inverse approximation is effectively mixing the activity preserving model and non-activity preserving model at once. In order for accurate implementation of activity preserving or non-activity preserving motion model, MCDR with exact transpose implementation is required.

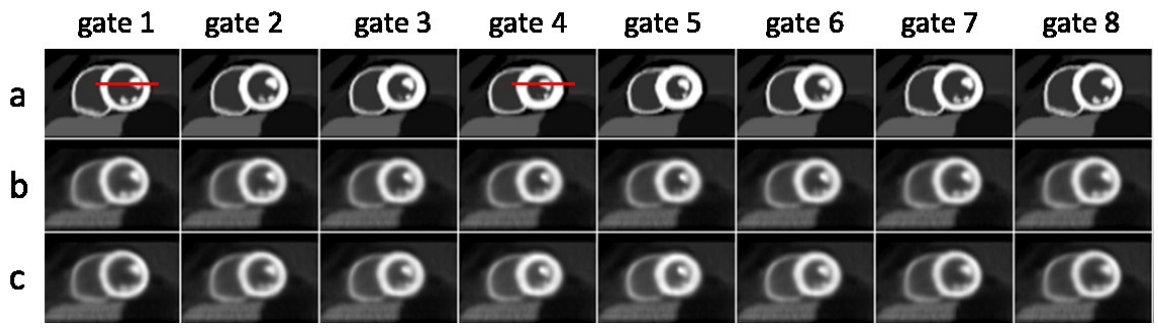

Figure 3-42 Short axis view of cardiac gated images using

a) 4D XCAT phantom, b) non-activity preserving MCDR, c) activity preserving MCDR.

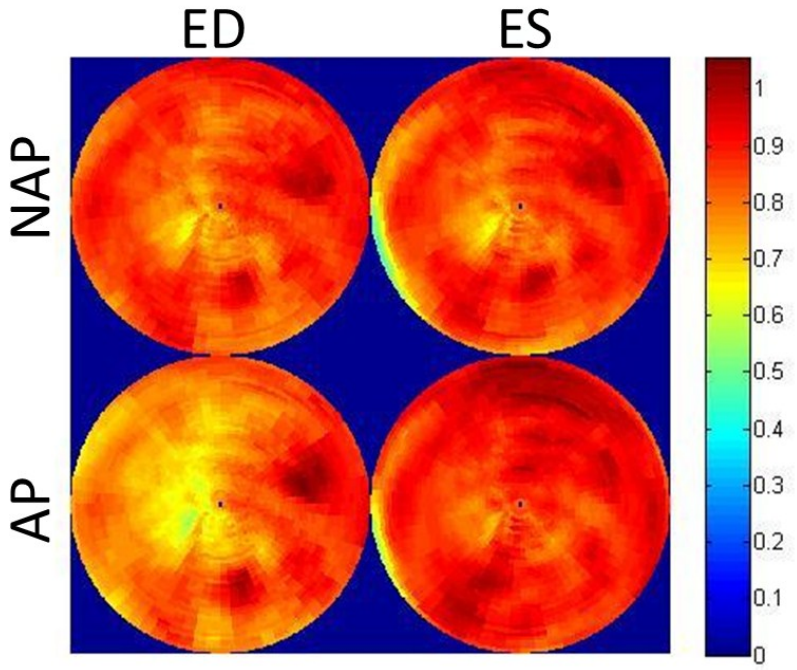

Figure 3-43 Normalized bull's eye map for left ventricle for both ED and ES using AP an NAP. With activity preserving (AP), the uptake of myocardium in ED showed reduced value because of larger partial volume effects caused by thinner myocardium wall.

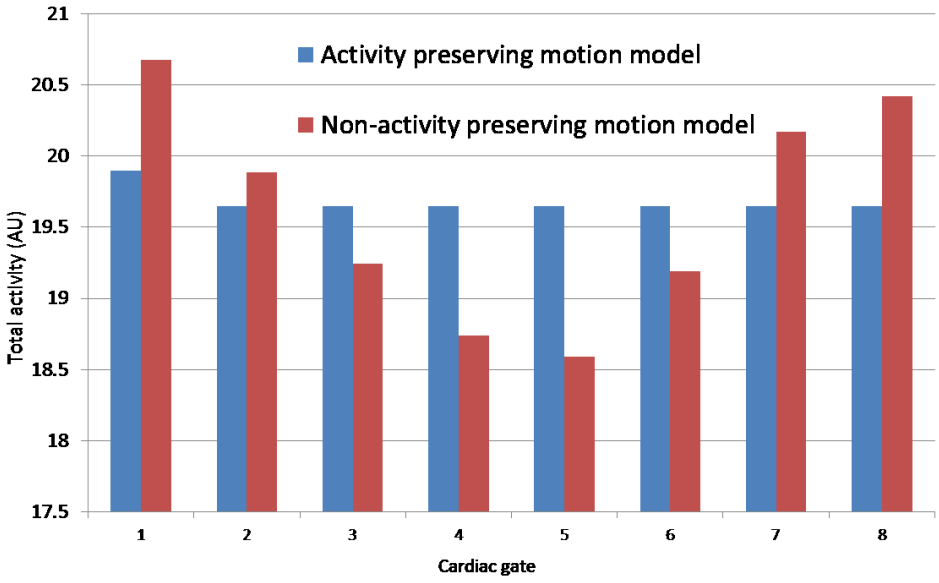

Figure 3-44. Comparison of activity of the heart with activity preserving and non-activity preserving model. The total activity of the heart is measured and only myocardium has activity uptakes, where gate 1 is ED and gate 4 is ES.

DUAL R&C MOTION CORRECTION BEFORE RECONSTRUCTION

In the case of MCDR and MCAR, The choice of reference frame is not a problem given reliable motion estimation; as one can always use inverse motion transform to go back to arbitrary gates. With the use of scout reconstruction as an approximation to the true activity distribution used in $p'_i = \sum_h \sum_j \frac{K_{h,j} x_{g,j}}{p_{g,h}} \cdot \delta\left(h\left(\boldsymbol{m'_{h,j}}\right) - i\right) p_{g,h}$

Equation 2-28, the choice of reference frame could affect the accuracy of motion correction.

The effects of different reference frame were shown in Figure 3-45. In the coronal view of end-systolic phase, the use of choice 1 reference frame resulted in some unwanted artifacts in the lower right part of the left ventricle even with true MVF. Choice 1 also resulted thin myocardium wall which was not true in the phantom. These artifacts were not present when choice 2 were used.

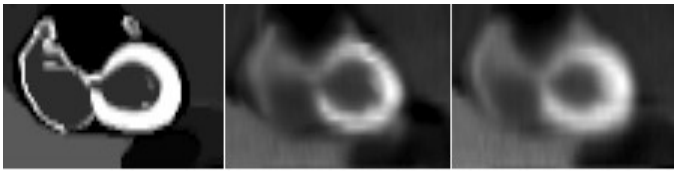

Figure 3-45 Coronal view of end-systolic phase of (left) phantom image, (middle) motion correction using reference frame choice 1, (right) motion correction using reference frame choice 2.

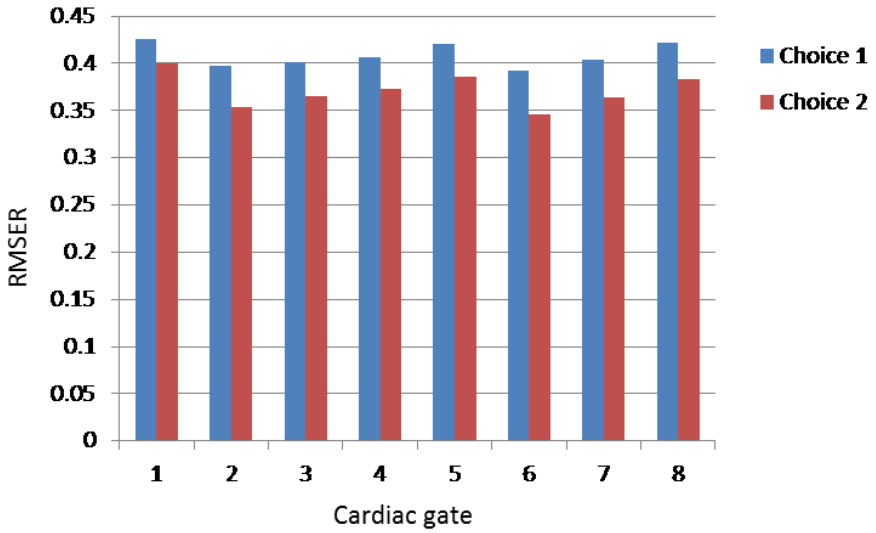

Figure 3-46 RMSER of 8 cardiac gate with MCBR using choice 1 and choice 2.

Quantitative analysis was also applied to choice 1 and choice 2. Figure 3-46 shows the RMSER of 8 cardiac gates when using two difference choices of reference frames. The result is consistent with Figure 3-45. These results of using both quantitative and qualitative comparisons in the above figures showed that for MCBR, the choice of reference frame is important. The above artifacts were likely caused by the combination of large amplitude of motion vectors and the scout reconstruction used to replace the true activity distribution. When a balanced choice such as choice 2 were used, the approximation error were likely reduced with the use of smaller motion amplitude and partially cancelled out by opposite motion vectors from different gates.

COMPARISON OF MCAR, MCDR AND MCBR FOR DUAL R&C

PATIENT DATA

Clinical patient data was used to evaluate the performance of MCDR and MCAR. The list of used patient data is shown in Table 3-9.

Table 3-9 Patient list for comparison of MCDR and MCAR.

Patient ID	P053	P055	M007	P057	V001

Total counts (1/mm)	44k	45k	20k	46k	243k
Total Scan Time (min)	6.9	4.5	10.8	5.5	12

Figure 3-47 shows the short-axis view of cardiac gated PET images obtained from patient V001 with 32 iterations for three different methods: NMC, MCAR and MCDR. Both MCAR and MCDR provide higher image quality in terms of improved resolution with minimum motion blur and much lower image noise level as compared to that without dual motion correction. The MCDR provided the best image quality with visible improvement in terms of higher contrast compared with MCAR.

The contrast-to-noise curve of using the same patient scan is shown in Figure 3-48. Each data point in Figure 3-48 represents a different iteration number during image reconstruction. Maximum number of iterations in image reconstruction for all three approaches is 120. With increased number of iterations, the data points shift from lower-left to upper-right (high contrast, high noise) in the contract-to-noise plot. The results that MCAR and MCDR both improved image qualities and MCDR outperforms MCAR were consistent to the result from Figure 3-47.

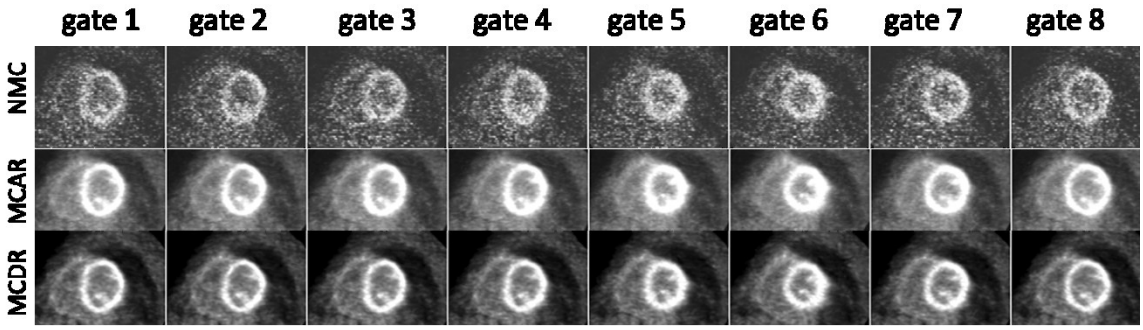

Figure 3-47 Short-axis cardiac gated PET images from a patient PET scan (V001).

1st tow : image reconstruction method without motion correction, 2nd row : dual R&C MCAR, 3rd row dual R&C MCDR.

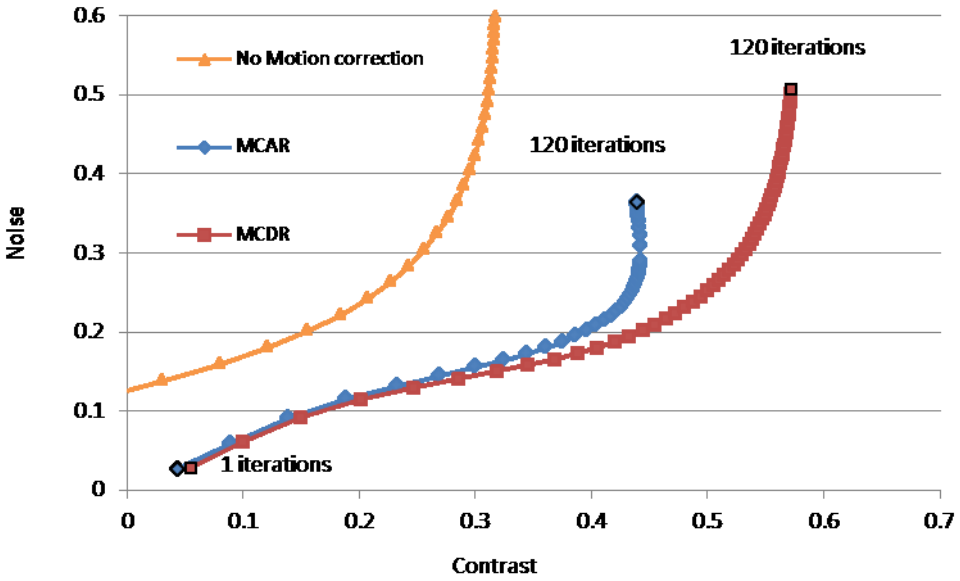

Figure 3-48 Contrast-to-noise plot from a patient V001 using three different image reconstruction methods.

Results from another patient (M004) with much higher noise level showed a different situation in Figure 3-49a. The comparison of using the same iteration number of 40 resulted in much higher noise level with MCDR than that with MCAR, which was inconsistent with that shown in Figure 3-47. To study this effect, contrast-to-noise curve for the same patient was measured and is shown in Figure 3-50. Both MCAR and MCDR showed significant improvement when compared with no motion correction. Even with over 100 iterations, MCAR did not achieve as high an image contrast as that of MCDR, but it reached convergence at around 40 iterations and remained at a similar contrast-noise point achieved by MCDR with only 9 iterations. This result suggested that images from the MCAR approach requires higher iterations to reach the same imaging parameters compared to the MCDR method. With increasing iterations, MCDR provided a wider range of contrast-noise trade-offs and extended to higher contrast values. This result also suggested that a full performance comparison between MCDR and MCAR should include the entire contrast-to-noise curves covering sufficiently larger number of iterations instead at a particular iteration number, in which case MCDR and MCAR could be at different stages of convergence. Figure 3-49b shows the results from images obtained using MCAR and MCDR at a lower iteration number of 9, from which the measured noise of MCDR was found to be at the same level of MCAR of 40 iterations as shown in Figure 3-50. This suggested that images with the same noise levels from MCAR in Figure 3-49a can be achieved using

MCDR with a lower iteration number. A comparison at the "knee" region of the contrast-noise curve was chosen and is shown at Figure 3-49c.

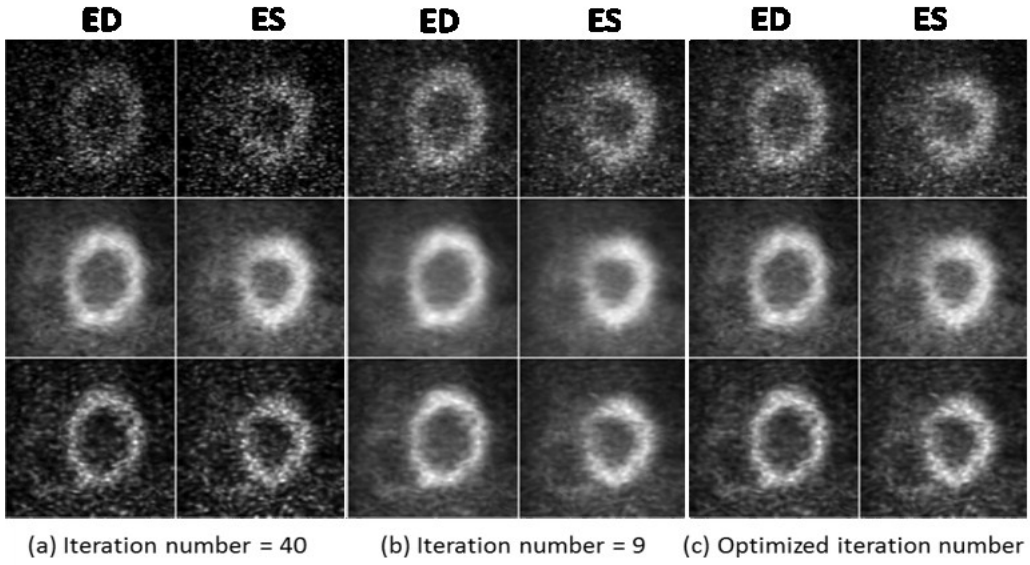

Figure 3-49 Short-axis view of cardiac gated PET images from patient scan M007

1st tow: End-diastolic phase (ED) and end-systolic phase (ES) using image reconstruction method without motion correction, 2nd row : with dual R&C MCAR, and (3rd row) the MCDR approach. (a) Same iteration number of 40 was used for all methods, (b) same iteration number 9 was used for all methods, (c) optimized iteration number (data point with black outline shown in Figure 3-50) was used for each method.

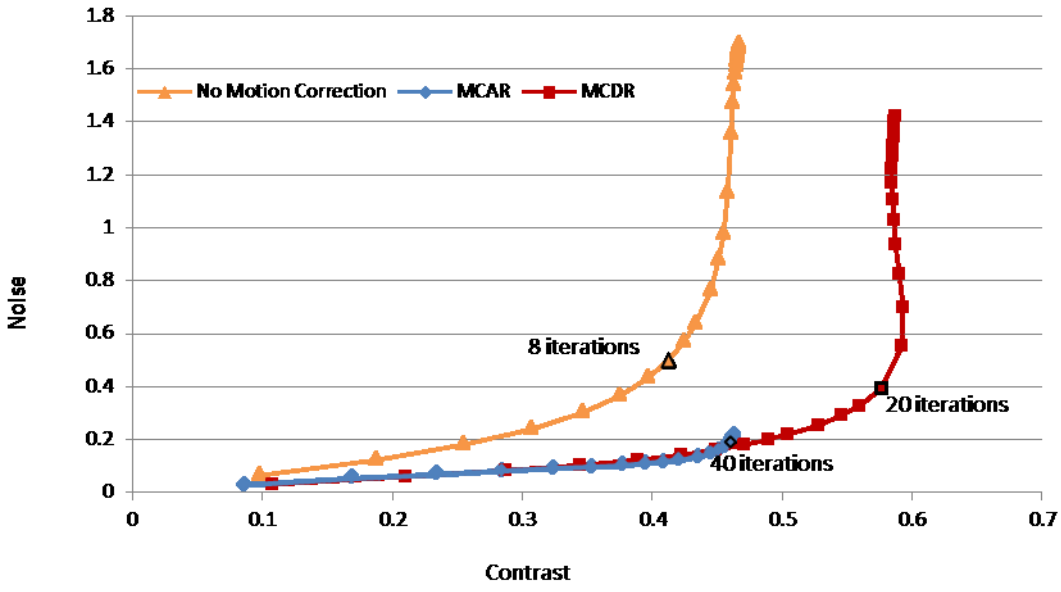

Figure 3-50 Contrast-to-noise plot from a patient scan M007 using three different image reconstruction methods.

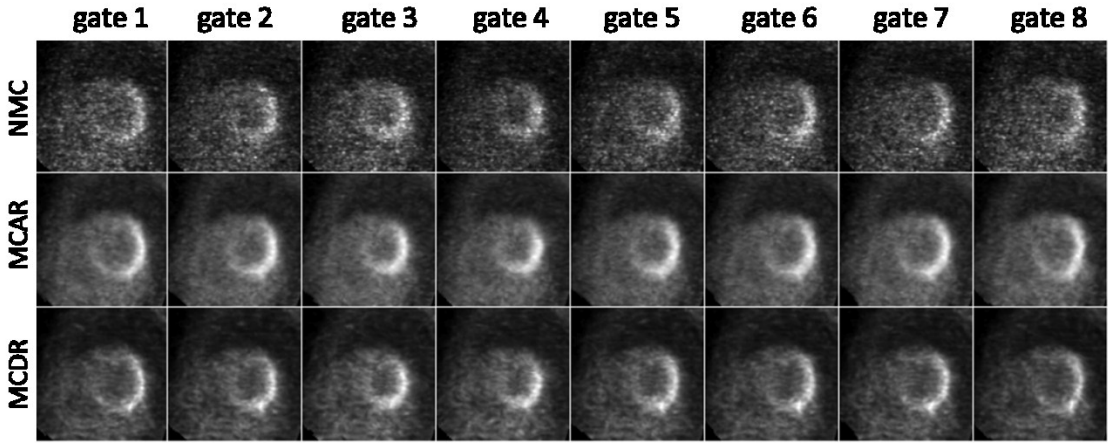

Figure 3-51 Short-axis view of cardiac gated PET images from patient scan P053.

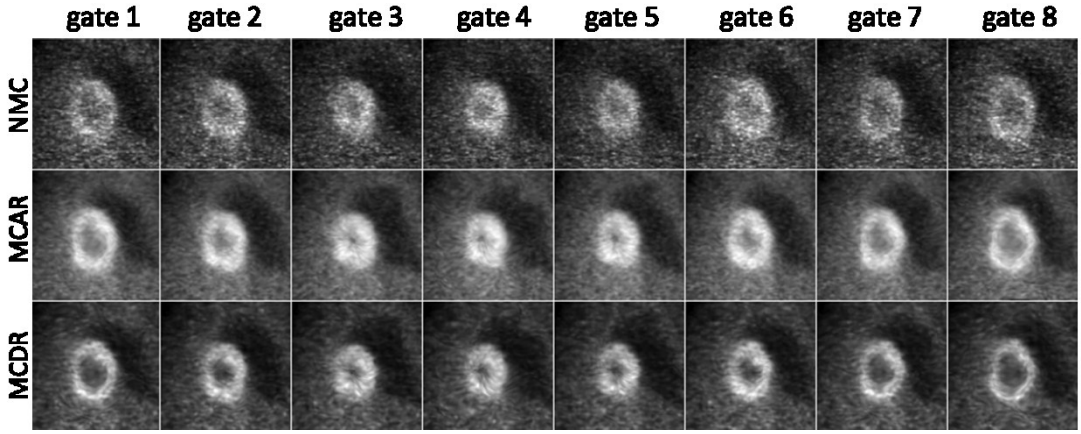

Figure 3-52 Short-axis view of cardiac gated PET images from patient scan P055.

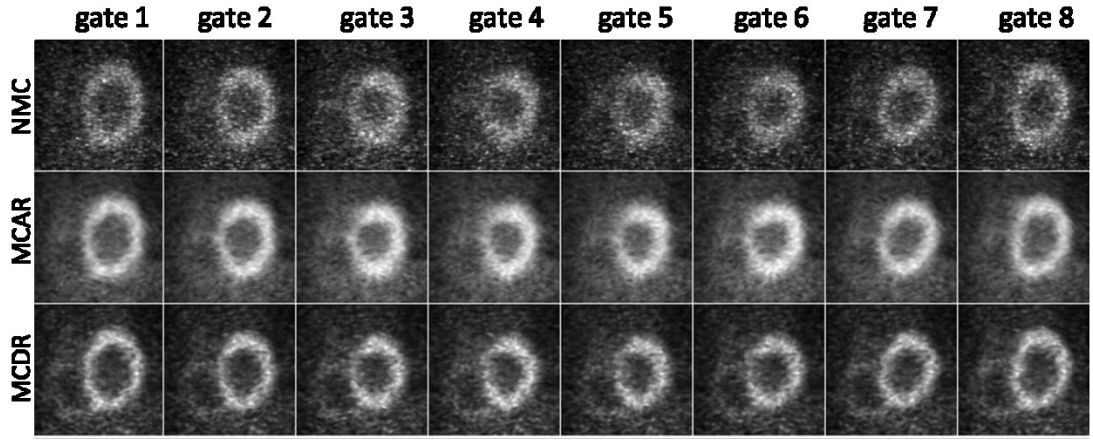

Figure 3-53 Short-axis view of cardiac gated PET images from patient scan M007.

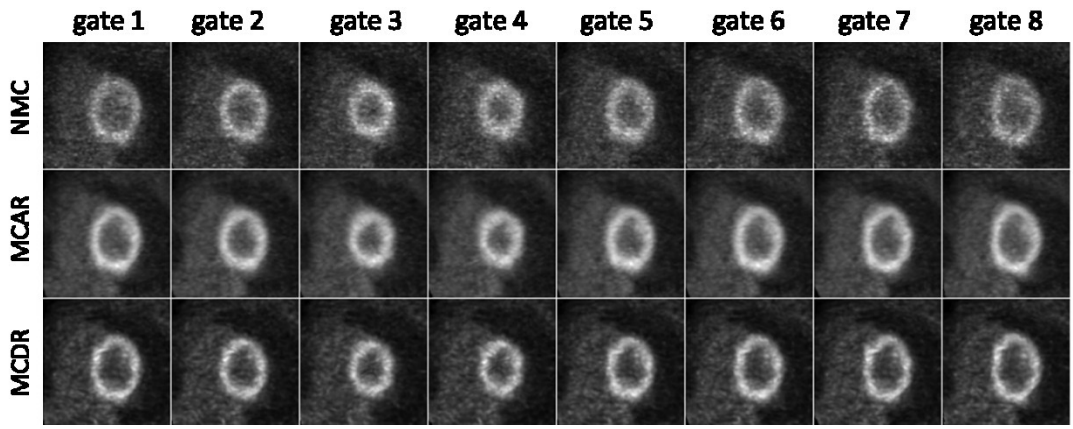

Figure 3-54 Short-axis view of cardiac gated PET images from patient scan P057.

Quantitative image quality evaluation using contrast-noise trade-off curves obtained from other patient data showed similar contrast-noise curves as shown in Figure 3-50. Figure 3-48 was only observed in one patient. For each of the three methods (no motion correction in the first row, MCAR in the second row and MCDR in the third row), an iteration number at the "knee" region of the contrast-noise curve was chosen in a comparison of the short-axis images from the patient studies shown in Figure 3-51, Figure 3-52, Figure 3-53, and Figure 3-54. No post-reconstruction smoothing was applied to images in any methods shown in these figures.

PHANTOM DATA

TRUE MVF FROM 4DXCAT

Dual R&C MCAR, MCBR, MCDR, and reconstruction without motion correction was applied to almost noise free data as well as noisy data using true motion vector fields from XCAT with activity preserving motion transform. The count level was shown in Table 3-1 and was determined using typical clinical 3D PET scans ~10 minutes.

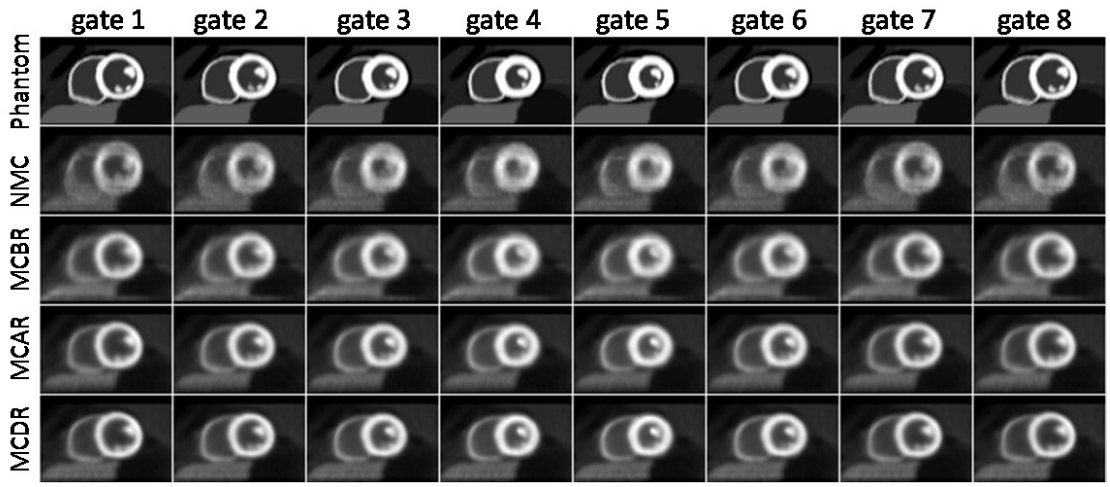

Figure 3-55 Short axis view of cardiac gated images using almost noise free simulation data.

The reconstructed images for almost noise free data are shown in Figure 3-55. The iteration number for MCAR, MCDR, MCBR, and the one without motion correction (NMC) was fixed to 40. All different methods showed improved image quality by reducing motion blur, while MCDR performed the best among the three visually. A quantitative comparison of RMSER and resolution for noise-free data was shown in Figure 3-56. The result shows that MCDR yields the best results for both RMSER and resolution recovery, which was consistent with visual comparison. While both MCAR and MCBR yield similar resolution recovery effects, the approximation used for MCBR results in higher RMSER due to the approximation used during that approach.

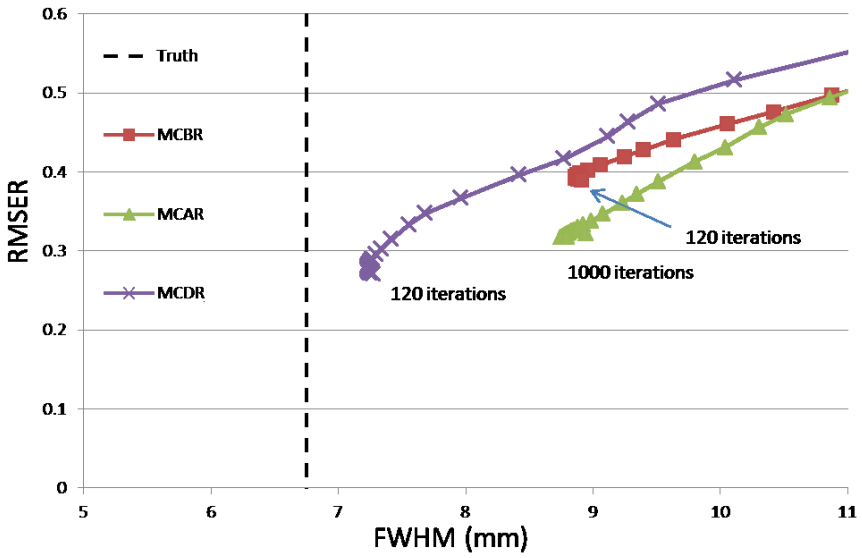

Figure 3-56 RMSER and measured FWHM of myocardium wall in different image iterations.

Noisy data using all three motion correction methods with fixed iteration at 40 are shown in Figure 3-57 (simulated 20 minutes scan), Figure 3-58 (simulated 10 minutes scan), Figure 3-59 (simulated 5 minutes scan), and Figure 3-60 (simulated 3 minutes scan). Additional Butterworth filter was applied on noisy reconstructed images without motion correction, no smoothing filter was used for motion corrected images. All three dual R&C methods demonstrated improved image quality when compared with images without motion correction for all four noise levels. MCBR showed inferior contrast and lower noise when compared with MCAR and MCDR in low noise situations, suggesting that the convergence speed for different method was different, and the studies of contrast, bias, and noise for all three methods using multiple iteration numbers are required.

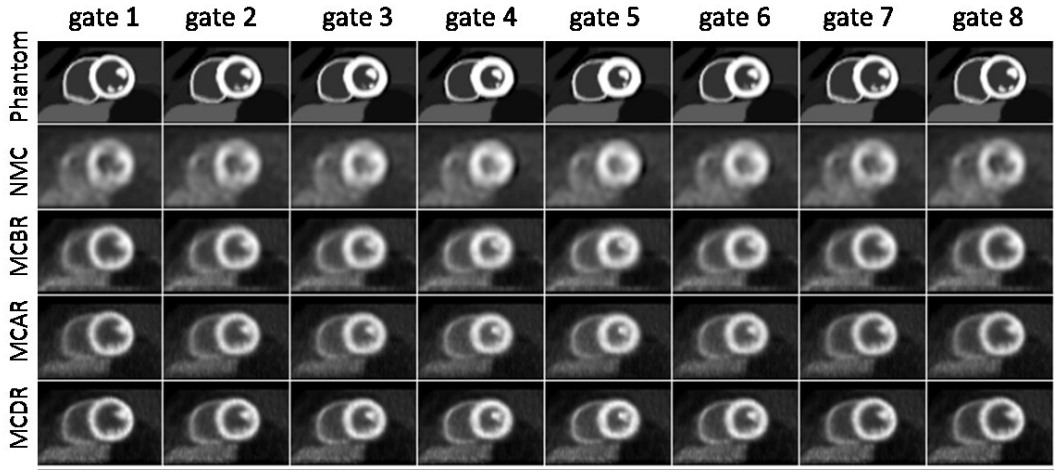

Figure 3-57 Short axis view of cardiac gated images using simulation data of a 20 minutes scan.

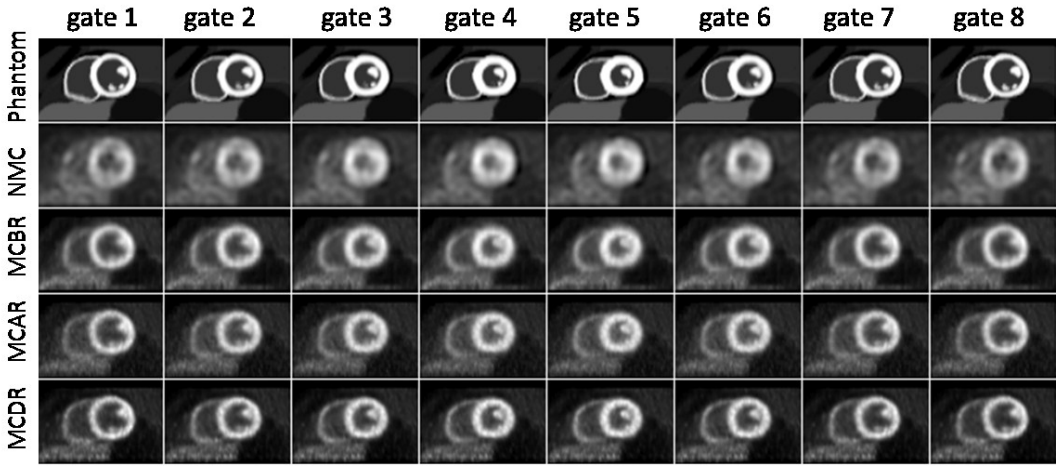

Figure 3-58 Short axis view of cardiac gated images using simulation data of a 10 minutes scan.

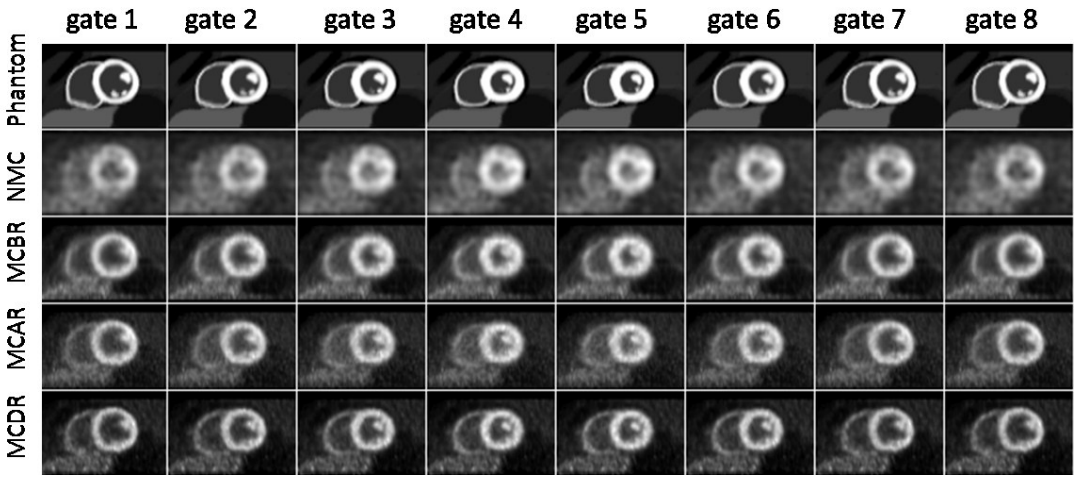

Figure 3-59 Short axis view of cardiac gated images using simulation data of a 5 minutes scan.

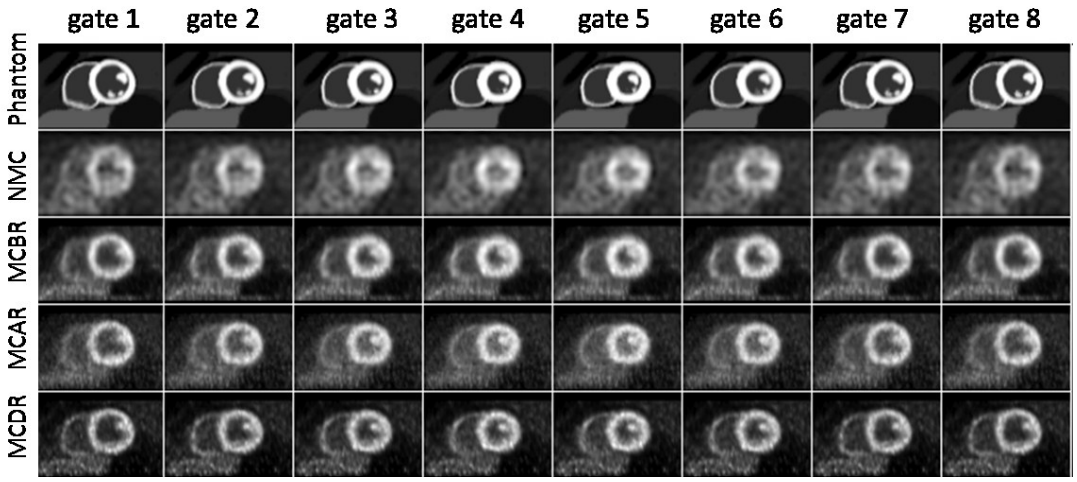

Figure 3-60 Short axis view of cardiac gated images using simulation data of a 3 minutes scan.

Noise properties for all four methods were studied using 100 noise realizations. Image noise was estimated using two different estimation methods (image-based noise estimation defined in Equation 2-34 and ensemble-based noise estimation defined in Equation 2-35) in two different VOIs (myocardium and blood pool). Figure 3-61 shows the comparison of image-based noise estimation and ensemble-based noise estimation using reconstructed images without motion correction. The results showed that image-based noise estimation can be a good replacement of ensemble-based noise estimation regardless of VOI. However, similar conclusion was not observed in MCBR (Figure 3-62), MCAR (Figure 3-63), and MCDR (Figure 3-64), in which cases the image-based noise estimation from myocardium VOI showed no linear

correspondence with ensemble-based noise estimation, suggesting image-based noise measured in myocardium region should not be used as an indication of noise levels. Image-based noise estimation from blood pool VOI on the other hand still linearly corresponded with ensemble-based noise estimation, suggesting it was reasonable to use image-based noise estimation from the blood pool region to approximate image noise in cases where ensemble-based noise is not possible such as patient studies. The difference in ensemble-based noise estimation using myocardium VOI or blood pool VOI is insignificant, suggesting either one can be used to represent image noise. As our interest is the myocardium region, myocardium VOI was used for ensemble-noise estimations unless otherwise noted. The noise plots were generated using simulation study of a 3 minutes scan, results from other noise levels showed similar conclusions.

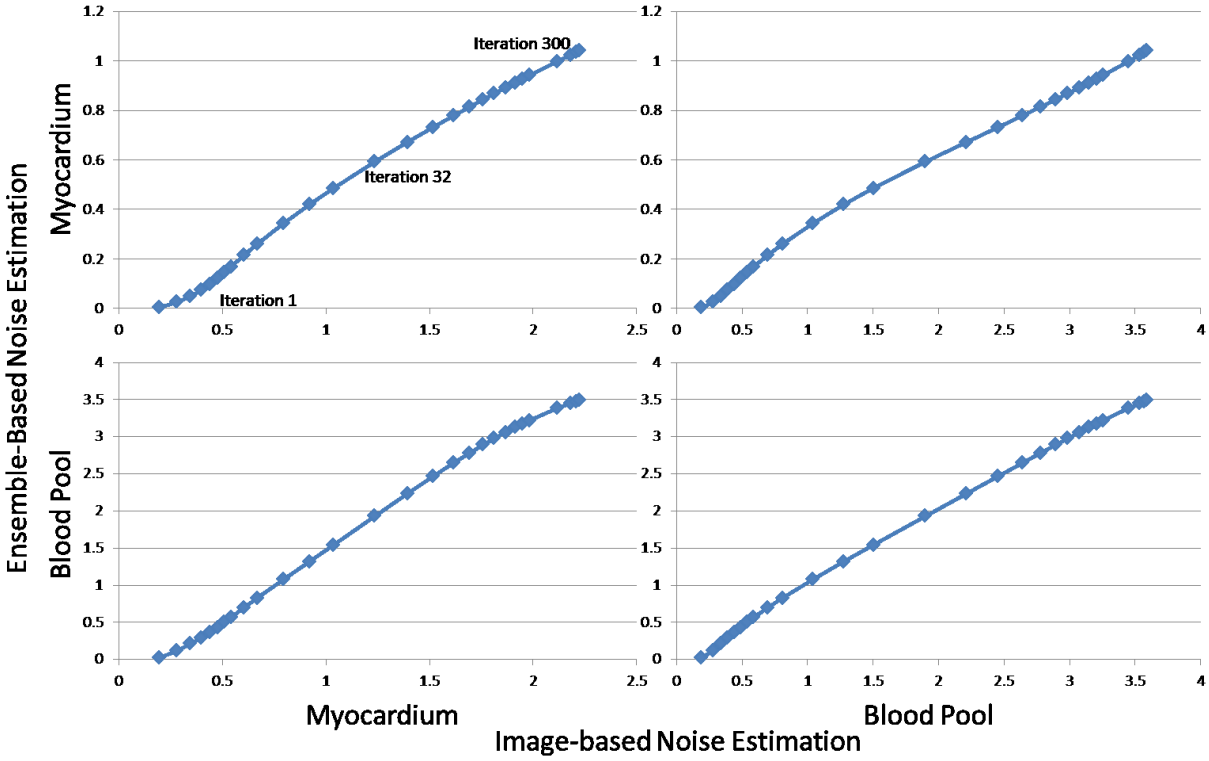

Figure 3-61 Image-based noise estimation and ensemble-based noise estimation using no motion correction.

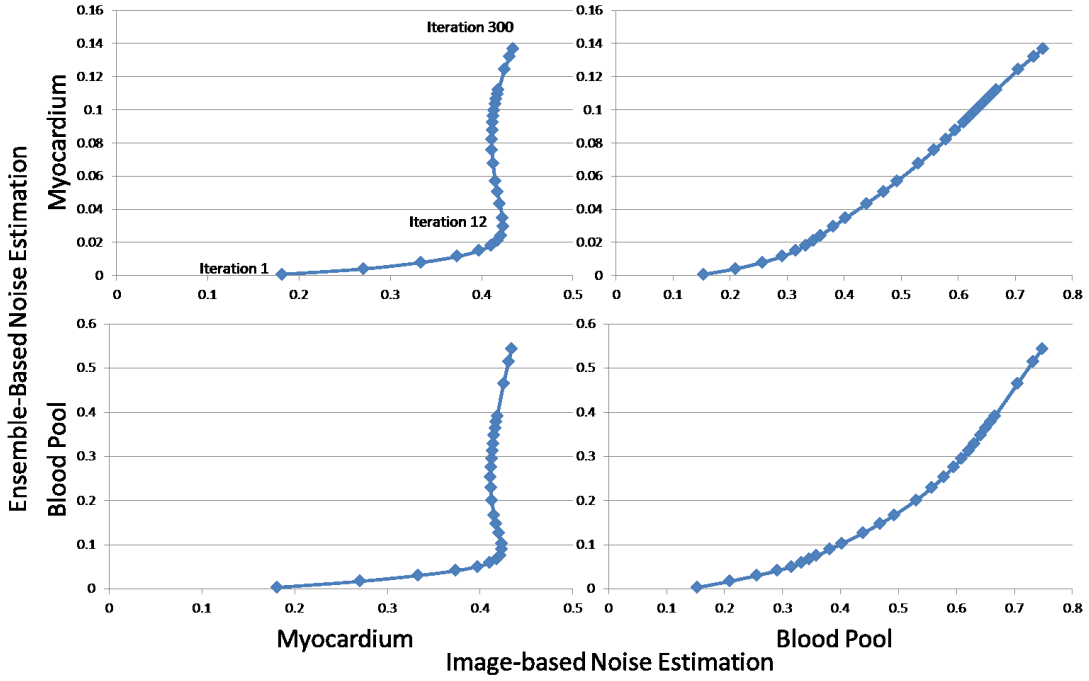

Figure 3-62 Image-based noise estimation and ensemble-based noise estimation using MCBR.

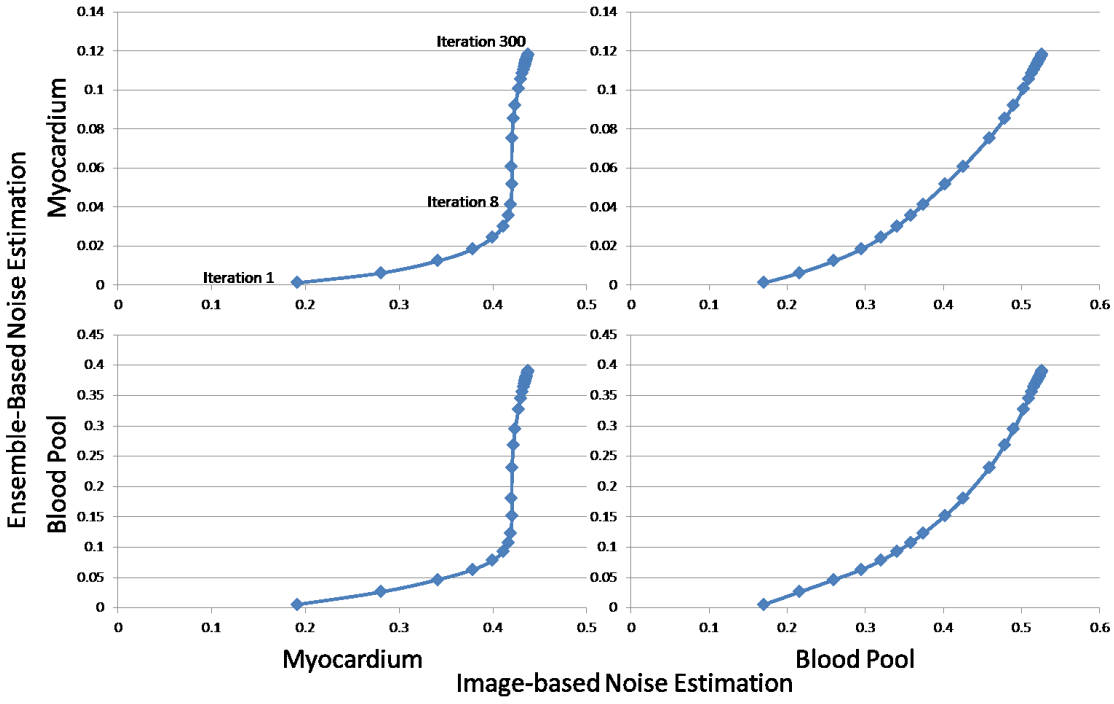

Figure 3-63 Image-based noise estimation and ensemble-based noise estimation using MCAR.

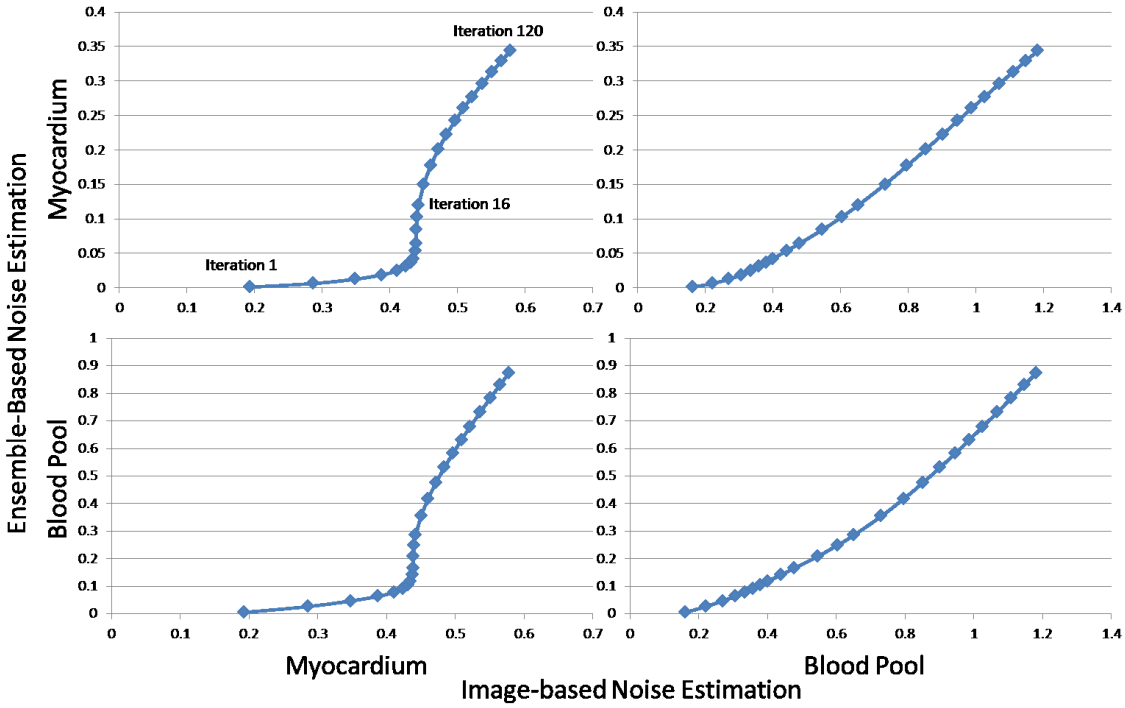

Figure 3-64 Image-based noise estimation and ensemble-based noise estimation using MCDR.

The reason for image-based noise estimation in the myocardium region with dual R&C motion correction was applied failed to correlate with ensemble-based noise estimation was that it violated the assumption that the voxels in the VOI is independent and identically distributed as the motion transformation in the myocardium changed the distribution for each voxel. The voxels in the blood pool was less affected due to the reason that the cardiac motion transformation did not affect the blood pool.

Figure 3-65 shows the contrast-noise using image-based noise estimation from the blood pool VOI to match the patient studies. The highest iteration number for MCDR was 120 and 500 for the other three. All data points were calculated using the mean value from all 100 noise realizations and the error for each data point was insignificant. The same iteration settings and number of noise realization were the same for other plots unless otherwise specified. Similar to Figure 3-50, MCAR overlaps MCDR in the first half of the curve, suggesting MCAR was equivalent to MCDR in the early iterations.

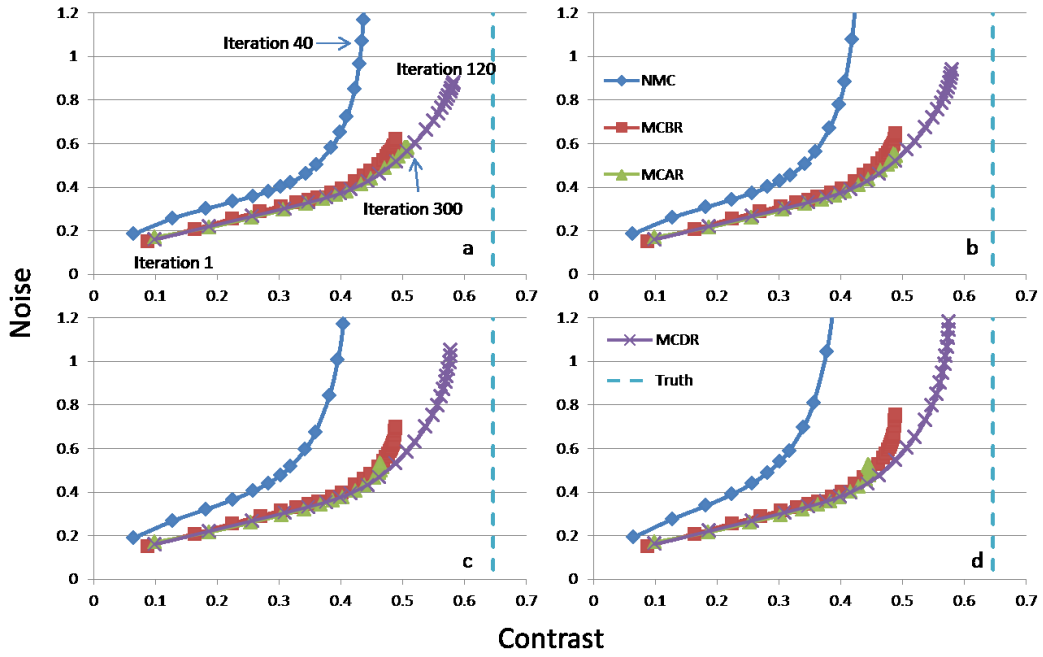

Figure 3-65 Contrast-noise curves using image-based nosie estimations for dual R&C motion correction a) Simulated 20 minute scan, b) Simulated 10 minute scan, c) Simulated 5 minute scan, d), Simulated 3 minute scan.

Contrast-nosie curves using ensemble-based noise estimation was also calculated and was shown in Figure 3-66. Unlike that in Figure 3-65, MCAR separated from MCDR and was closer to Figure 3-48. Suggesting that the overlap of MCAR and MCDR was actually caused by using image-based noise as an approximation. In both Figure 3-65 and Figure 3-66, MCAR showed significant reduction of contrast with increased noise level, which was not oberseved in MCBR and MCDR. While MCDR consistently yielded the best contrast-noise trade-offs. MCBR outperformed MCAR in low count situations (scan time <10 minutes).

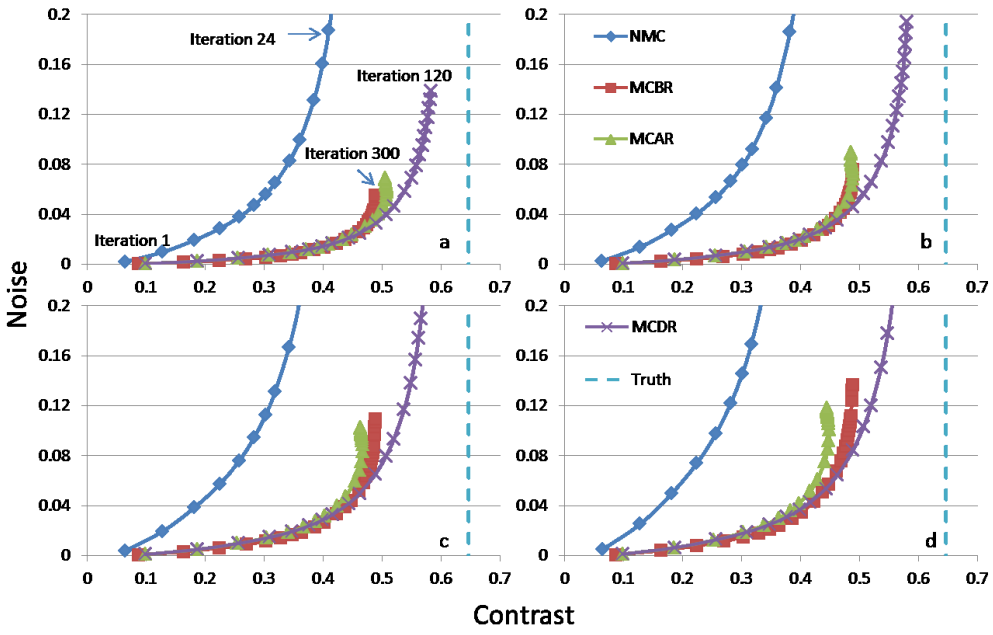

Figure 3-66 Contrast-noise curves using ensemble-based nosie estimations for dual R&C motion correction a) Simulated 20 minute scan, b) Simulated 10 minute scan, c) Simulated 5 minute scan, d), Simulated 3 minute scan.

The contrast-noise curves (Figure 3-67) were also calculated to demonstrate the quantitative accuracy of all three methods with true MVF for varieties of noise levels. MCDR always yielded the best results and all three motion correction methods showed significant improvement over the result without motion correction. Similar to the phenomenon observed in Figure 3-66, with the increase of noise, MCAR showed increase bias. The explanation of this phenomenon is: to achieve MCAR with 48 total respiratory and cardiac gates, 48 reconstructions each using ~1/48 of the total counts is required. With iterative image reconstruction approach is not strictly linear and with the possibility of resulting bias in low count situations [ref the kidney input function paper], the summation of 48 reconstructed results with 1/48 total counts from each results in larger error when compared with only one reconstruction using the total counts. The result also shows that MCBR approach was less sensitive to noise and motion estimation error in terms of RMSER when compared with the MCAR. Figure 3-66 and Figure 3-67 also suggested that MCDR showed faster convergence speed when compared with MCAR and MCBR.

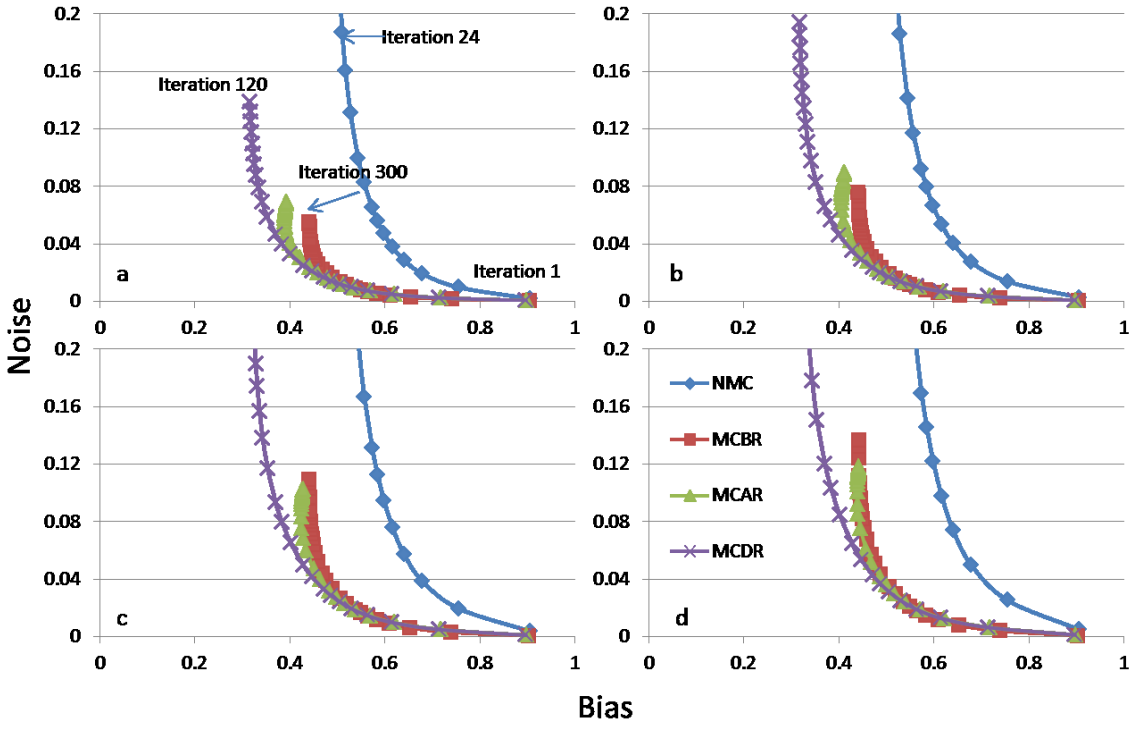

Figure 3-67 Bias-Noise tradeoff curve of three different dual R&C motion correction methods using (a) simulation of 20 minutes scan, (b) simulation of 10 minutes scan, (c) simulation of 5 minutes scan, and (d) simulation of 3 minutes scan.

RMSER of the myocardium region was also calculated for different methods and different noise levels and was shown in Figure 3-68. Iteration number of reconstruction was optimized individually when calculating RMSER. All three dual R&C motion correction techniques demonstrated reduced RMSER and MCDR consistently yields the best results among other methods for different noise levels. For less noisy data, MCAR results lower RMSER than MCBR, but the rank of these two reverses with higher noise level, which was consistent with Figure 3-66 and Figure 3-67.

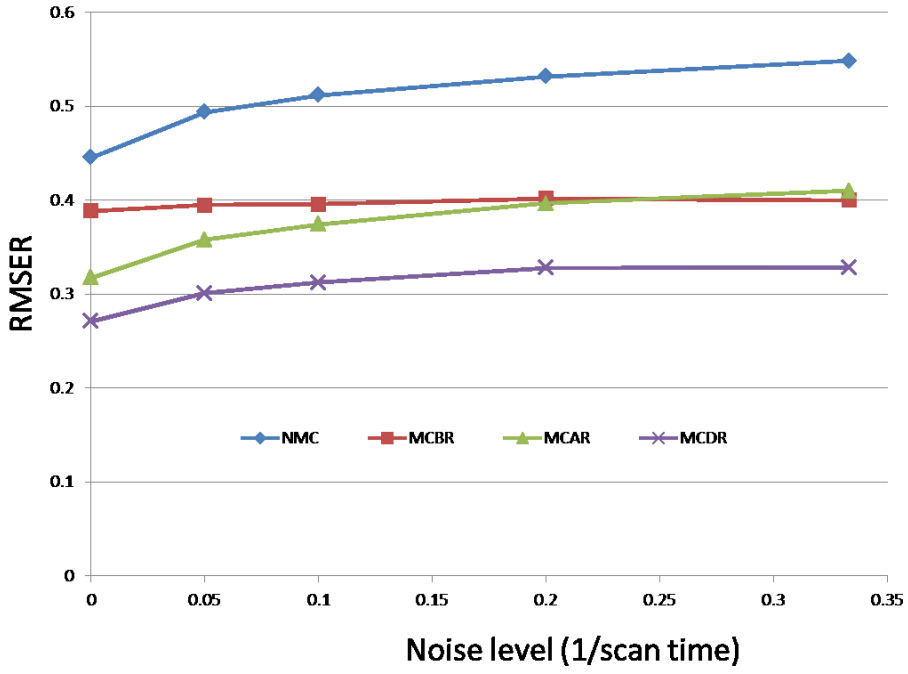

Figure 3-68 Measured RMSER of different noise levels using MCBR, MCAR, and MCDR using true motion vector field from XCAT.

ESTIMATED MVF

Figure 3-69 shows the result of three motion correction approaches with individually estimated respiratory and cardiac motion using almost noise free simulation data. The phantom image and images without motion correction are identical with that in Figure 3-55. Similar to the results obtained from Figure 3-55, all three dual R&C motion correction methods demonstrated improved image quality and reduced motion blur compared with images without motion correction. Figure 3-70, Figure 3-71, Figure 3-72, and Figure 3-73 show the reconstructed images with different demonstrated)Inferior image quality compared with Figure 8 was observed due to inaccurate motion estimation. Increased noise levels also results in decreased inaccuracy of motion estimation.

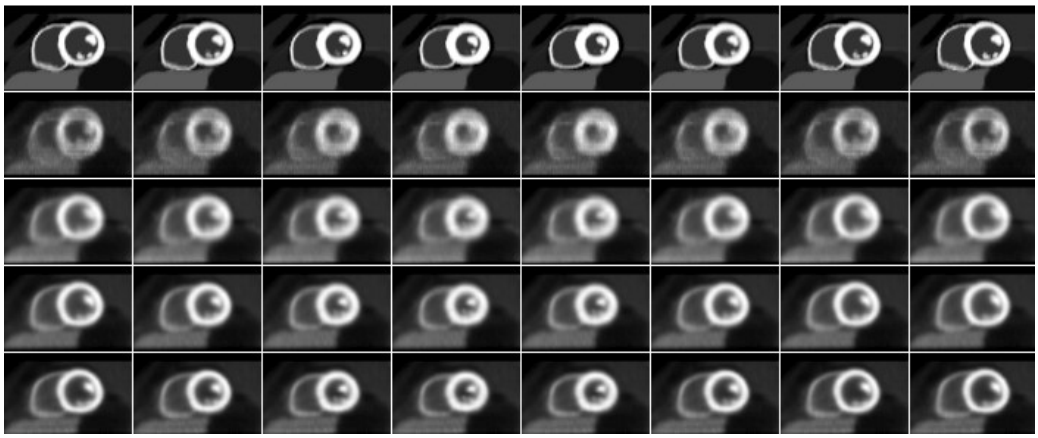

Figure 3-69 Short axis view of cardiac gated images using almost noise free simulation data.

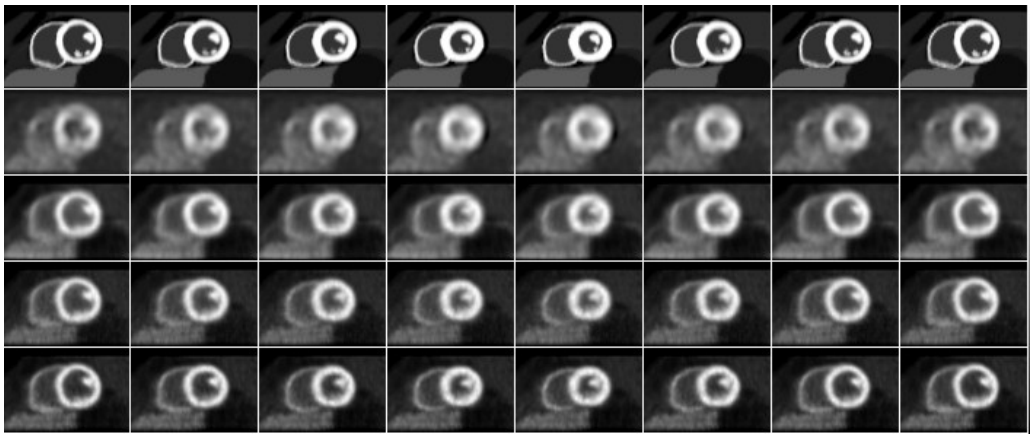

Figure 3-70 Short axis view of cardiac gated images using simulation data of a 20 minutes scan.

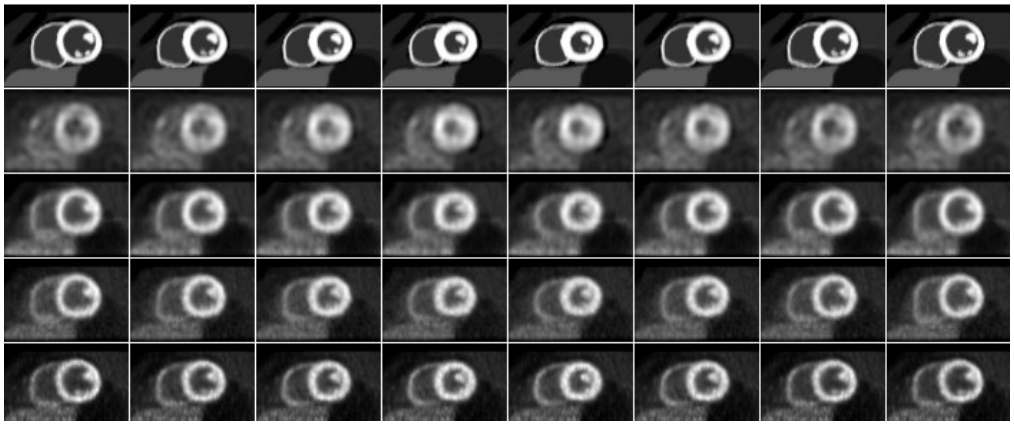

Figure 3-71 Short axis view of cardiac gated images using simulation data of a 10 minutes scan.

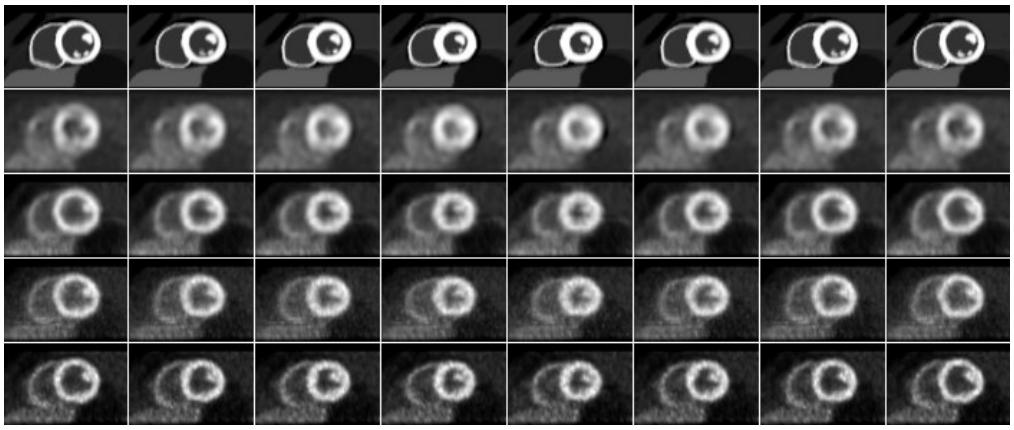

Figure 3-72 Short axis view of cardiac gated images using simulation data of a 5 minutes scan.

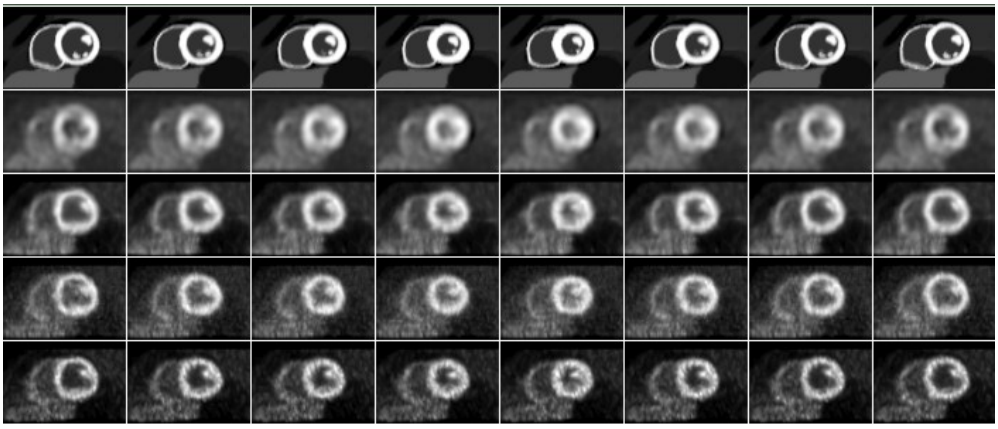

Figure 3-73 Short axis view of cardiac gated images using simulation data of a 3 minutes scan.

RMSER of the myocardium region using estimated MVF was also calculated for different methods and different noise levels and was shown in Figure 3-74. Iteration number of reconstruction was optimized individually when calculating RMSER. Similar with the results shown in Figure 3-68, all three dual R&C motion correction techniques demonstrated reduced RMSER and MCDR consistently yields the best results among other methods for different noise levels. For less noisy data, MCAR results lower RMSER than MCBR, but the rank of these two reverses with higher noise level. The overall RMSER is larger than using true MVF.

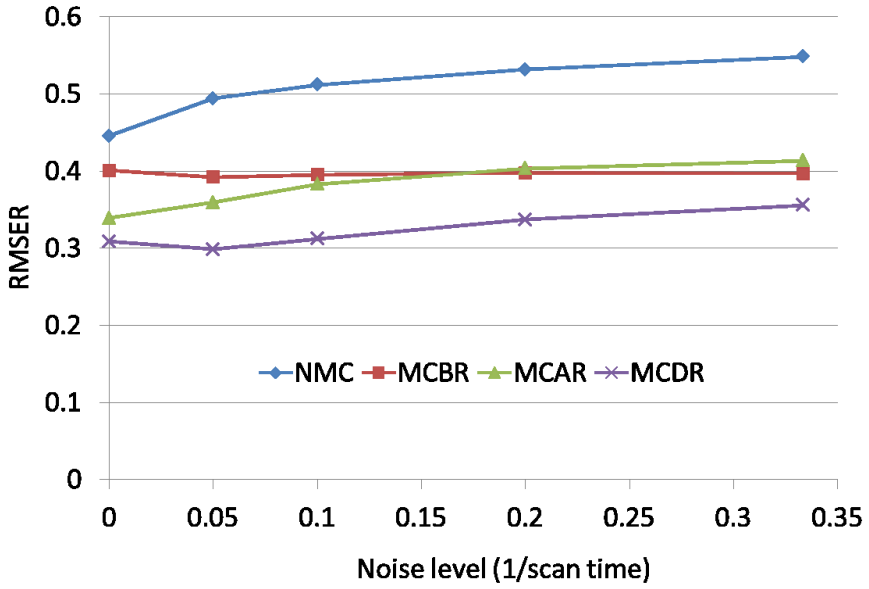

Figure 3-74 Measured RMSER of different noise levels using MCBR, MCAR, and MCDR using individual estimated MVF.

CHAPTER 4. CONCLUSIONS

GATING TECHNIQUES

We demonstrated that in cases where the myocardium uptake in the PET data is high (sinogram contrast larger than 1.7), both data-driven and MRI navigator gating can be used. In cases when the uptake is low (sinogram contrast smaller than 1.4), MRI navigator proves to be a reliable method for extracting respiratory motion signal while the data-driven method failed. Results in literature suggests that in some cases there could be motion mismatch between the diaphragm respiratory motion and heart respiratory motion [100], this effects are not observed in this study due to limited patient data. Overall, the benefit and shortcomings of both methods are listed in Table 4-1.

Table 4-1 Pros and cons for PET-based and MRI-based respiratory gating methods.

	Pros	Cons
PET-based data-driven method	1. Direct measurement of myocardium motion. 2. No need for extra MRI sequence or external device	1. Sensitive to myocardium uptake and noise level 2. Inaccurate absolute motion amplitude
MRI-based navigator gating	1. Independent of myocardial uptake and noise level 2. Accurate absolute motion amplitude	1. Possible mismatch of respiratory motion in the heart and diaphragm dome. 2. Require additional MRI sequence 3. Can introduce artifact in MRI images

While the noise level also affects the accuracy of data-driven methods, in the range of our limited patient data, we have found that the noise effect to be not as important as the uptake levels in the myocardium.

Similar approach using Equation 2-3 can be adopted for cardiac gating, but ECG-based cardiac gating is shown to be more reliable [67] in the literature as the cardiac motion signal may not detected in some patient studies,, and therefore is used for cardiac gating in our study.

MOTION ESTIMATION TECHNIQUES

In this work, we focused on the study of PET-based motion estimation and MR-based motion estimation from navigator. The general conclusion is that for dual R&C motion estimation purpose, we have found that Method 3 in MEAR to provide the best option.

MOTION ESTIMATION AFTER IMAGE RECONSTRUCTION

Both MVF-based evaluation (Figure 3-20) and CC using almost noise free data (Table 3-6) suggests that Method 3 and Method 4 outperform Method 1 and Method 2. As Method 4 is more computational expensive, we have found Method 3 should be used for dual R&C motion estimation based on our findings.

Method 1 results in comparable accuracy in almost noise free case suggesting the inferior performance of Method 1 is caused by high image noise level in the dual R&C gated reconstructed images, which implies that although Method 1 is theoretically correct, in practical case Method 1 should not be used. The decrease of accuracy in Method 2 suggests that the respiratory and cardiac motion is not independent. The comparable results of Method 3 and Method 4 suggest that the effects of cardiac motion on respiratory motion estimation can be neglected. Therefore, although respiratory and cardiac motion are not independent, one only need to consider the effects of respiratory motion on cardiac motion estimation. The explanation is that the spatial variation of respiratory motion is much lower when compared with the spatial variation of cardiac motion, thus cardiac motion estimation using a set of images with respiratory motion blur results in higher inaccuracy but not the otherwise.

MVF-based evaluation method as shown in Figure 3-22 suggests that the motion estimation using PET-based images is rather inaccurate, while image-based evaluation using CC as shown in Figure 3-25 and Table 3-6 suggests the difference in terms of image difference is minimal. The reason for that is the aperture problem; the motion components that do not contribute visible changes on the images cannot be accurately estimated using current method. Therefore although current motion estimation approach can provided improved image quality, more advanced method such as feature based motion estimation [95] are required for quantification of cardiac motion using PET images.

Although image-based MVF evaluation cannot provide the exact assessment of MVF due to the aperture problem, we have found that in cases when MVF-based evaluation is not available, the CC index using noise-free images is an appropriate way to provide a ranking for different motion estimation methods. As noise-free images are not available in clinical situation, an accurate quantitative evaluation method of PET-imaged motion estimation based on clinical data still remains to be a major challenge. The CC calculated using the same set of noisy images which is used for estimating MVF would lead to false ranking of the performance of the motion estimation method. As in this case, the high CC value is caused by the registration of noise pattern rather than real image structure and motion. Therefore, the same image dataset should not be used for both estimation and evaluation and Motion Estimation during image reconstruction

Although MEDR shows improved estimation accuracy than MEAR on cardiac motion estimation (Figure 3-29), for dual R&C motion estimation, MEDR suffers the same noise challenge as that in dual R&C MEAR. While separate estimation of respiratory and cardiac motion (similar to Method 2 in MEAR) could reduce the influence of noise, the effects of respiratory motion on cardiac motion estimation must be taken into consideration as suggested by the results from previous section. Similar approaches for MEDR required projection based motion correction to reduce the respiratory motion for accurate cardiac motion estimation, which was an approximation (Equation 2-28). Furthermore, MEAR has the potential to integrate images from other modalities such as MRI or CT, which is more promising for accurate motion estimation. Given those reasons, MEDR is not used for dual R&C motion correction.

MOTION ESTIMATION BEFORE IMAGE RECONSTRUCTION

The proposed new respiratory motion estimation method, MEBR, may not be as accurate as the other two methods (MEAR and MEDR). The inaccuracy can be attributed to the over-simplification used in the motion estimation (Figure 2-24). Another assumption used is that the motion in different angles are independent, which is not true in real cases. On the other hand, MEBR does not require additional image reconstructions and can be potentially fast than the other methods.

However, the proposed MEBR method cannot apply to cardiac motion correction, as the approximation made in MEBR requires relatively simple motion (Figure 2-24). Therefore, MEBR cannot be used for dual R&C motion estimation which is its limitation.

MOTION ESTIMATION FROM MR NAVIGATOR

While it is feasible to use MR navigator for respiratory motion estimation, we have demonstrated inferior results (Figure 3-36) when compared with PET-base motion estimation method (MEAR) when the PET data have low statistical fluctuations and high cardiac to background ratio. The assumption of using MR-navigator (respirator motion is affine and can be simplified using 1D motion model) is the main reason for the inferior performance as the real respiratory motion is 3D. However, the use of MR navigator has the benefit of independent or PET image quality, and therefor can be an alternative when the signal in PET images is low. However, the current MR navigator approach does not allow the estimation of cardiac motion.

MOTION CORRECTION TECHNIQUES

In this work, we have developed and evaluated three dual R&C motion correction methods, motion correction before, during, and after image reconstruction, i.e. MCBR, MCDR, and MCAR. All three methods demonstrate dramatic improvement in terms of image quality and quantitation when compared with images without motion correction (Figure 3-60). The dramatic improvement can also be translated into reduced scan time or injection dose, which can reduce cost for related medical exams and be beneficial to patient health.

Our comparison of AP motion transform and NAP transform shows that the AP motion model preserves the total activity in myocardium. “Blinking” effects in the 4D beating heart is present in the AP motion model, and is likely caused by the partial volume effects (Figure 3-43). The NAP motion models changes the total activity within the myocardium, but reduces the “blinking” effect. When accurate quantitation of myocardium is required, the combined use of AP motion model and partial volume effect correction is likely to provide better results.

Studies from multiple noise realizations (Figure 3-63) suggest that myocardium VOI-based noise estimation cannot represent the true image noise with motion correction. On the other hand blood pool VOI-based noise estimation shows good correlations with ensemble based noise estimation. Our results suggest that blood pool VOI based noise estimation should be used instead of myocardium VOI based noise estimation when ensemble based noise estimation is not available.

Below is the conclusions found for individual 4D image reconstruction method:

MOTION CORRECTION AFTER IMAGE RECONSTRUCTION

Being developed previously in our group and well-studied in literature, MCAR is essentially a post-processing technique that is independent of reconstructions. The implementation of MCAR can be relatively simple compared with MCDR and MCBR, which makes it easier for clinical application. However, based on our Monte Carlo simulation, the quantitative accuracy of MCAR is very sensitive to noise level, which makes the quantitative performance of MCAR relatively poor in short scans/low dose scans (Figure 3-68). The reason that MCAR has poor quantitative performance is that each image reconstruction is done on dual gated data with extremely high noise. Studies in the literature [101] suggested the existence of quantitative bias in the reconstruction images, which cannot be reduced by averaging operation done after image reconstruction. However, in cases where only qualitative results are required (low noise, high bias images) and implementations of other advanced methods are unrealistic, MCAR can be a good option.

MOTION CORRECTION DURING IMAGE RECONSTRUCTION

The MCDR method is found to be the method that achieves the best image quality as well as the highest quantitative accuracy over different noise levels in our study. The use of exact implementation of transpose motion transform outperforms the use of inverse motion transform that used in the literature, suggesting the approximation does affect the performance of MCDR. We have also found that the use of inverse approximation is essentially mixing AP transform with NAP transform, and therefore resulting in an approach that follows neither AP nor NAP constrain. With these facts, we conclude that MCDR with the

exact implementation is the best option for providing quantitative images when the acquired data has low statistical noise fluctuation and high cardiac to background uptake ratio.

MOTION CORRECTION BEFORE IMAGE RECONSTRUCTION

The main advantage of MCBR is its computational speed its handle of statistical noise in the acquired data. The computational cost for the MCDR and MCAR method can be a deterrent as the larger than 48 times increase in computational time required for MCDR in a single iteration and for MCAR to reconstruction 48 reconstructions with 6 respiratory and 8 cardiac grates. The MCDR method is even slower due to the fact that motion transform is required in every iteration. While parallel computing is a viable solution, MCBR with only two reconstructions needed provides an alternative approach to dramatically reduce the computational time by applying motion correction on projection data before a single reconstruction. With the approximations used in MCBR, the image quality as well as quantitative accuracy is slightly inferior to the other two in high counts situations. However, in low counts situations, the MCBR method results in even better quantitative accuracy than MCAR, as the later approach is more sensitive to noise. Possible improvement can be made in MCBR by iteratively replacing the scout reconstruction with motion corrected images.

CHAPTER 5. FUTURE WORK

In this work, we have demonstrated the feasibility of 4D image reconstruction with dual respiratory and cardiac motion correction. However, there are still more works that need to be done to further improve the image quality and accuracy of the provide estimate motion information for better improved clinical diagnosis.

Figure 2-1 provides the general guidelines for 4D image reconstructions with motion correction. For the first step, generation of 4D data, additional methods could be applied to improve the PET-data driven methods to further expand the range to patient with low myocardium uptakes. The possible influence of the tracer dynamic, i.e., the change of organs uptakes on the data-driven methods remains a mystery. Current evaluations are based on patient data and the accuracy of gating may not be guaranteed. Realistic Monte Carlo simulations of the listmode data with known respiratory and cardiac motion signals are required for an evaluation study with known truth.

The major challenge lies in the second step, in which we showed that the accuracy of cardiac motion estimation remains low because of the aperture problem. Although this inaccuracy may not be important for better image quality, it is important for functional analysis of the heart such as stress and strain. Feature-based approach can be one of the promising approaches that can improve the accuracy and robustness of cardiac motion estimation [95]. The motion estimation error contributes to the quantitative accuracy as shown in Figure 3-74. The estimation parameters were optimized based on normal myocardium motion, which is the one we used in our simulation. A sick heart with abnormal motion could be more challenging to estimate and more studies are required for abnormal myocardium motion to further reduce motion estimation error. Image noise is another factor that degrades the accuracy of estimated motion, and it could be the bottleneck for further reduction of scan time or patient dose. Accurate 4D cardiac motion estimated from simultaneous PET/MRI could be the solution but more work are required for fast MRI acquisition for motion estimation as current MRI sequence used for motion estimation could take very long time.

The improvement for the third step includes the motion compensation for intra-frame motion, which may become increasingly important with the continuously improvement on PET systems. The inaccuracy of

MCBR could be further reduced by iterative approach, i.e. the use of accurate activity distributions generated from MCBR instead of the scout image.

Channelized hoteling observer (CHO) can also be applied to better evaluation as the CHO provides models the performance of the visual system. The evaluation using CHO could provide more insight on the performance of different methods. While limited numbers of patient data are used for testing in this dissertation, more detailed analysis using varieties of patient data, including those from normal and abnormal patients, are required to test the robustness of 4D image reconstruction with motion correction.

Although our 4D image reconstruction algorithm was developed for the imaging of myocardium in PET, it could be applied to SPECT and CT as well. It could also improve the imaging of plaques using PET, as with the use of NaF recently. There is usually no myocardium uptakes in plaque imaging and the images of plaque are degraded by both respiratory and cardiac motion. With the use of similar techniques on plaque imaging, we could be one step closer for early detection of CAD.

REFERENCE

1. M.M. Ter-Pogossian, M.E. Phelps, E.J. Hoffman, and N.A. Mullani, *A positron-emission transaxial tomograph for nuclear imaging (PETT).* Radiology, 1975. **114**(1): p. 89-98.

2. R.H. Huebner, K.C. Park, J.E. Shepherd, J. Schwimmer, J. Czernin, M.E. Phelps, and S.S. Gambhir, *A meta-analysis of the literature for whole-body FDG PET detection of recurrent colorectal cancer.* Journal of Nuclear Medicine, 2000. **41**(7): p. 1177-1189.

3. H.T. Chugani, M.E. Phelps, and J.C. Mazziotta, *Positron Emission Tomography Study of Human-Brain Functional-Development.* Annals of Neurology, 1987. **22**(4): p. 487-497.

4. N. Tamaki, Y. Yonekura, K. Yamashita, H. Saji, Y. Magata, M. Senda, Y. Konishi, K. Hirata, T. Ban, and J. Konishi, *Positron Emission Tomography Using F-18 Deoxyglucose in Evaluation of Coronary-Artery Bypass-Grafting.* American Journal of Cardiology, 1989. **64**(14): p. 860-865.

5. P.E. Kinahan and J.G. Rogers, *Analytic 3d Image-Reconstruction Using All Detected Events.* Ieee Transactions on Nuclear Science, 1989. **36**(1): p. 964-968.

6. L.A. Shepp and Y. Vardi, *Maximum likelihood reconstruction for emission tomography.* IEEE Trans Med Imaging, 1982. **1**(2): p. 113-22.

7. K. Lange and R. Carson, *EM reconstruction algorithms for emission and transmission tomography.* J Comput Assist Tomogr, 1984. **8**(2): p. 306-16.

8. H.M. Hudson and R.S. Larkin, *Accelerated Image-Reconstruction Using Ordered Subsets of Projection Data.* Ieee Transactions on Medical Imaging, 1994. **13**(4): p. 601-609.

9. S. Macmahon, R. Peto, J. Cutler, R. Collins, P. Sorlie, J. Neaton, R. Abbott, J. Godwin, A. Dyer, and J. Stamler, *Blood-Pressure, Stroke, and Coronary Heart-Disease .1. Prolonged Differences in Blood-Pressure - Prospective Observational Studies Corrected for the Regression Dilution Bias.* Lancet, 1990. **335**(8692): p. 765-774.

10. L.L. Demer, K.L. Gould, R.A. Goldstein, R.L. Kirkeeide, N.A. Mullani, R.W. Smalling, A. Nishikawa, and M.E. Merhige, *Assessment of Coronary-Artery Disease Severity by Positron Emission Tomography - Comparison with Quantitative Arteriography in 193 Patients.* Circulation, 1989. **79**(4): p. 825-835.

11. M. Schwaiger, *Myocardial Perfusion Imaging with Pet.* Journal of Nuclear Medicine, 1994. **35**(4): p. 693-698.

12. R. Medina, I.P. Panidis, J. Morganroth, M.N. Kotler, and G.S. Mintz, *The Value of Echocardiographic Regional Wall Motion Abnormalities in Detecting Coronary-Artery Disease in Patients with or without a Dilated Left-Ventricle.* American Heart Journal, 1985. **109**(4): p. 799-803.

13. M.F. Di Carli, S. Dorbala, J. Meserve, G. El Fakhri, A. Sitek, and S.C. Moore, *Clinical myocardial perfusion PET/CT.* Journal of Nuclear Medicine, 2007. **48**(5): p. 783-793.

14. Y. Petibon, G. El Fakhri, R. Nezafat, N. Johnson, T. Brady, and J. Ouyang, *Towards coronary plaque imaging using simultaneous PET-MR: a simulation study.* Physics in Medicine and Biology, 2014. **59**(5).

15. N. Ghosh, O.E. Rimoldi, R.S.B. Beanlands, and P.G. Camici, *Assessment of myocardial ischaemia and viability: role of positron emission tomography.* European Heart Journal, 2010. **31**(24): p. 2984-2995.

16. K. Fukushima, P.E. Bravo, T. Higuchi, K.H. Schuleri, X.P. Lin, M.R. Abraham, J.S. Xia, W.B. Mathews, R.F. Dannals, A.C. Lardo, Z. Szabo, and F.M. Bengel, *Molecular Hybrid Positron Emission Tomography/Computed Tomography Imaging of Cardiac Angiotensin II Type 1 Receptors.* Journal of the American College of Cardiology, 2012. **60**(24): p. 2527-2534.

17. W. Okumura, T. Iwasaki, T. Toyama, T. Iso, M. Arai, N. Oriuchi, K. Endo, T. Yokoyama, T. Suzuki, and M. Kurabayashi, *Usefulness of fasting F-18-FDG PET in identification of cardiac sarcoidosis.* Journal of Nuclear Medicine, 2004. **45**(12): p. 1989-1998.

18. K. Classic, *Medical imaging physics, fourth edition.* Health Physics, 2002. **83**(6): p. 921-921.

19. O. Klein and Y. Nishina, *About the Scattering of Radiation by free Electrons after the new relativistic Quantum dynamics of Dirac.* Zeitschrift Fur Physik, 1929. **52**(11-12): p. 853-868.

20. P.E. Kinahan, D.W. Townsend, T. Beyer, and D. Sashin, *Attenuation correction for a combined 3D PET/CT scanner.* Medical Physics, 1998. **25**(10): p. 2046-2053.

21. C.S. Levin and E.J. Hoffman, *Calculation of positron range and its effect on the fundamental limit of positron emission tomography system spatial resolution.* Physics in Medicine and Biology, 1999. **44**(3): p. 781-799.

22. B.E. Hammer, N.L. Christensen, and B.G. Heil, *Use of a Magnetic-Field to Increase the Spatial-Resolution Positron Emission Tomography.* Medical Physics, 1994. **21**(12): p. 1917-1920.

23. A.J. Reader, S. Ally, F. Bakatselos, R. Manavaki, R.J. Walledge, A.P. Jeavons, P.J. Julyan, S. Zhao, D.L. Hastings, and J. Zweit, *One-pass list-mode EM algorithm for high-resolution 3-D PET image reconstruction into large arrays.* Ieee Transactions on Nuclear Science, 2002. **49**(3): p. 693-699.

24. M. Rafecas, G. Boning, B.J. Pichler, E. Lorenz, M. Schwaiger, and S.I. Ziegler, *Effect of noise in the probability matrix used for statistical reconstruction of PET data.* Ieee Transactions on Nuclear Science, 2004. **51**(1): p. 149-156.

25. S. Siegel and M. Dahlbom, *Implementation and Evaluation of a Calculated Attenuation Correction for Pet.* Ieee Transactions on Nuclear Science, 1992. **39**(4): p. 1117-1121.

26. A. Martinez-Moller, M. Souvatzoglou, G. Delso, R.A. Bundschuh, C. Chefd'hotel, S.I. Ziegler, N. Navab, M. Schwaiger, and S.G. Nekolla, *Tissue Classification as a Potential Approach for Attenuation Correction in Whole-Body PET/MRI: Evaluation with PET/CT Data.* Journal of Nuclear Medicine, 2009. **50**(4): p. 520-526.

27. M. Hofmann, F. Steinke, V. Scheel, G. Charpiat, J. Farquhar, P. Aschoff, M. Brady, B. Scholkopf, and B.J. Pichler, *MRI-Based Attenuation Correction for PET/MRI: A Novel Approach Combining Pattern Recognition and Atlas Registration.* Journal of Nuclear Medicine, 2008. **49**(11): p. 1875-1883.

28. A. Rezaei, M. Defrise, G. Bal, C. Michel, M. Conti, C. Watson, and J. Nuyts, *Simultaneous Reconstruction of Activity and Attenuation in Time-of-Flight PET.* Ieee Transactions on Medical Imaging, 2012. **31**(12): p. 2224-2233.

29. D. Brasse, P.E. Kinahan, C. Lartizien, C. Comtat, M. Casey, and C. Michel, *Correction methods for random coincidences in fully 3D whole-body PET: Impact on data and image quality.* Journal of Nuclear Medicine, 2005. **46**(5): p. 859-867.

30. H. Zaidi, *Scatter modelling and correction strategies in fully 3-D PET.* Nuclear Medicine Communications, 2001. **22**(11): p. 1181-1184.

31. J.M. Ollinger, *Model-based scatter correction for fully 3D PET.* Physics in Medicine and Biology, 1996. **41**(1): p. 153-176.

32. C.W. Stearns, *Scatter correction method for 3D PET using 2D fitted Gaussian functions.* J Nucl Med 36.5 (1995), 1995. **105P.**

33. D.L. Bailey and S.R. Meikle, *A Convolution-Subtraction Scatter Correction Method for 3d Pet.* Physics in Medicine and Biology, 1994. **39**(3): p. 411-424.

34. C.S. Levin, M. Dahlbom, and E.J. Hoffman, *A Monte-Carlo Correction for the Effect of Compton-Scattering in 3-D Pet Brain Imaging.* Ieee Transactions on Nuclear Science, 1995. **42**(4): p. 1181-1185.

35. L.X. Shao, R. Freifelder, and J.S. Karp, *Triple Energy Window Scatter Correction Technique in Pet.* Ieee Transactions on Medical Imaging, 1994. **13**(4): p. 641-648.

36. S.R. Cherry, S.R. Meikle, and E.J. Hoffman, *Correction and Characterization of Scattered Events in 3-Dimensional Pet Using Scanners with Retractable Septa.* Journal of Nuclear Medicine, 1993. **34**(4): p. 671-678.

37. C.C. Watson, *New, faster, image-based scatter correction for 3D PET.* Ieee Transactions on Nuclear Science, 2000. **47**(4): p. 1587-1594.

38. K. Shibuya, E. Yoshida, F. Nishikido, T. Suzuki, T. Tsuda, N. Inadama, T. Yamaya, and H. Murayama, *Limit of Spatial Resolution in FDG-PET due to Annihilation Photon Non-Collinearity.* World Congress on Medical Physics and Biomedical Engineering 2006, Vol 14, Pts 1-6, 2007. **14**: p. 1667-1671.

39. V.Y. Panin, F. Kehren, C. Michel, and M. Casey, *Fully 3-D PET reconstruction with system matrix derived from point source measurements.* Ieee Transactions on Medical Imaging, 2006. **25**(7): p. 907-921.

40. R. Lecomte, D. Schmitt, and G. Lamoureux, *Geometry Study of a High-Resolution Pet Detection System Using Small Detectors.* Ieee Transactions on Nuclear Science, 1984. **31**(1): p. 556-561.

41. D. Strul, R.B. Slates, M. Dahlbom, S.R. Cherry, and P.K. Marsden, *An improved analytical detector response function model for multilayer small-diameter PET scanners.* Physics in Medicine and Biology, 2003. **48**(8): p. 979-994.

42. V.V. Selivanov, Y. Picard, J. Cadorette, S. Rodrigue, and R. Lecomte, *Detector response models for statistical iterative image reconstruction in high resolution PET.* Ieee Transactions on Nuclear Science, 2000. **47**(3): p. 1168-1175.

43. S. Yamamoto and H. Ishibashi, *A GSO depth of interaction detector for PET.* Ieee Transactions on Nuclear Science, 1998. **45**(3): p. 1078-1082.

44. M. Defrise, D.W. Townsend, D. Bailey, A. Geissbuhler, C. Michel, and T. Jones, *A Normalization Technique for 3d Pet Data.* Physics in Medicine and Biology, 1991. **36**(7): p. 939-952.

45. E.J. Hoffman, T.M. Guerrero, G. Germano, W.M. Digby, and M. Dahlbom, *Pet System Calibrations and Corrections for Quantitative and Spatially Accurate Images.* Ieee Transactions on Nuclear Science, 1989. **36**(1): p. 1108-1112.

46. R.D. Badawi, M.A. Lodge, and P.K. Marsden, *Algorithms for calculating detector efficiency normalization coefficients for true coincidences in 3D PET.* Physics in Medicine and Biology, 1998. **43**(1): p. 189-205.

47. C.F.J. Wu, *On the Convergence Properties of the Em Algorithm.* Annals of Statistics, 1983. **11**(1): p. 95-103.

48. A.J. Reader, S. Ally, F. Bakatselos, R. Manavaki, R.J. Walledge, A.P. Jeavons, P.J. Julyan, S. Zhao, D.L. Hastings, and J. Zweit, *Regularized one-pass list-mode EM algorithm for high resolution 3D PET image reconstruction into large arrays.* 2001 Ieee Nuclear Science Symposium, Conference Records, Vols 1-4, 2002: p. 1853-1858.

49. A.J. Reader, R. Manavaki, S. Zhao, P.J. Julyan, D.L. Hastings, and J. Zweit, *Accelerated list-mode EM algorithm.* Ieee Transactions on Nuclear Science, 2002. **49**(1): p. 42-49.

50. C. Kolbitsch, C. Prieto, C. Tsoumpas, and T. Schaeffter, *A 3D MR-acquisition scheme for nonrigid bulk motion correction in simultaneous PET-MR.* Medical Physics, 2014. **41**(8): p. 490-503.

51. S.A. Nehmeh, Y.E. Erdi, G.S.P. Meirelles, O. Squire, S.M. Larson, J.L. Humm, and H. Schoder, *Deep-inspiration breath-hold PET/CT of the thorax.* Journal of Nuclear Medicine, 2007. **48**(1): p. 22-26.

52. S.A. Nehmeh and Y.E. Erdi, *Respiratory motion in positron emission tomography/computed tomography: A review.* Seminars in Nuclear Medicine, 2008. **38**(3): p. 167-176.

53. C. Liu, L.A. Pierce, A.M. Alessio, and P.E. Kinahan, *The impact of respiratory motion on tumor quantification and delineation in static PET/CT imaging.* Physics in Medicine and Biology, 2009. **54**(24): p. 7345-7362.

54. S. Chen and B.M.W. Tsui, *Accuracy Analysis of Image-based Respiratory Motion Estimation and Compensation in Respiratory-gated PET Reconstruction.* 2008 Ieee Nuclear Science Symposium and Medical Imaging Conference (2008 Nss/Mic), Vols 1-9, 2009: p. 3566-3569.

55. W. Sureshbabu and O. Mawlawi, *PET/CT imaging artifacts.* J. Nucl. Med. Technol., 2005. **vol. 33** (September 1): p. no. 3 156-161.

56. L. Le Meunier, R. Maass-Moreno, J.A. Carrasquillo, W. Dieckmann, and S.L. Bacharach, *PET/CT imaging: Effect of respiratory motion on apparent myocardial uptake.* Journal of Nuclear Cardiology, 2006. **13**(6): p. 821-830.

57. A. Martinez-Moller, M. Souvatzoglou, N. Navab, M. Schwaiger, and S.G. Nekolla, *Artifacts from misaligned CT in cardiac perfusion PET/CT studies: Frequency, effects, and potential solutions.* Journal of Nuclear Medicine, 2007. **48**(2): p. 188-193.

58. I.S. Rogers, K. Nasir, A.L. Figueroa, R.C. Cury, U. Hoffmann, D.A. Vermylen, T.J. Brady, and A. Tawakol, *Feasibility of FDG Imaging of the Coronary Arteries Comparison Between Acute Coronary Syndrome and Stable Angina.* Jacc-Cardiovascular Imaging, 2010. **3**(4): p. 388-397.

59. J. Freiberg, J.D. Hove, K.F. Kofoed, T. Fritz-Hansen, S. Holm, H.B. Larsson, and H. Kelbaek, *Absolute quantitation of left ventricular wall and cavity parameters using ECG-gated PET.* Journal of Nuclear Cardiology, 2004. **11**(1): p. 38-46.

60. G.J. Klein, B.W. Reutter, M.H. Ho, J.H. Reed, and R.H. Huesman, *Real-time system for respiratory-cardiac gating in positron tomography.* Ieee Transactions on Nuclear Science, 1998. **45**(4): p. 2139-2143.

61. A. Martinez-Moller, D. Zikic, R.M. Botnar, R.A. Bundschuh, W. Howe, S.I. Ziegler, N. Navab, M. Schwaiger, and S.G. Nekolla, *Dual cardiac-respiratory gated PET: implementation and results from a feasibility study.* Eur J Nucl Med Mol Imaging, 2007. **34**(9): p. 1447-54.

62. M. Dawood, F. Buther, N. Lang, O. Schober, and K.P. Schafers, *Respiratory gating in positron emission tomography: A quantitative comparison of different gating schemes.* Medical Physics, 2007. **34**(7): p. 3067-3076.

63. C.K. McKibben and N.V. Reo, *A piezoelectric respiratory monitor for in vivo NMR.* Magnetic Resonance in Medicine, 1992. **27**(2): p. 338-42.

64. L. Boucher, S. Rodrigue, R. Lecomte, and F. Benard, *Respiratory gating for 3-dimensional PET of the thorax: Feasibility and initial results.* Journal of Nuclear Medicine, 2004. **45**(2): p. 214-219.

65. X.A. Li, C. Stepaniak, and E. Gore, *Technical and dosimetric aspects of respiratory gating using a pressure-sensor motion monitoring system.* Medical Physics, 2006. **33**(1): p. 145-154.

66. S.A. Nehmeh, Y.E. Erdi, C.C. Ling, K.E. Rosenzweig, H. Schoder, S.M. Larson, H.A. Macapinlac, O.D. Squire, and J.L. Humm, *Effect of respiratory gating on quantifying PET images of lung cancer.* J Nucl Med, 2002. **43**(7): p. 876-81.

67. F. Buther, M. Dawood, L. Stegger, F. Wubbeling, M. Schafers, O. Schober, and K.P. Schafers, *List Mode-Driven Cardiac and Respiratory Gating in PET.* Journal of Nuclear Medicine, 2009. **50**(5): p. 674-681.

68. M.J. Park, S. Chen, T.S. Lee, G.S.K. Fung, M. Lodge, and B.M.W. Tsui, *Generation and Evaluation of a Simultaneous Cardiac and Respiratory Gated Rb-82 PET Simulation.* 2011 Ieee Nuclear Science Symposium and Medical Imaging Conference (Nss/Mic), 2011: p. 3327-3330.

69. T. Kokki, H.T. Sipila, M. Teras, T. Noponen, N. Durand-Schaefer, R. Klen, and J. Knuuti, *Dual gated PET/CT imaging of small targets of the heart: Method description and testing with a dynamic heart phantom.* Journal of Nuclear Cardiology, 2010. **17**(1): p. 71-84.

70. T. Pan, T.Y. Lee, E. Rietzel, and G.T.Y. Chen, *4D-CT imaging of a volume influenced by respiratory motion on multi-slice CT.* Medical Physics, 2004. **31**(2): p. 333-340.

71. M. Prummer, J. Hornegger, G. Lauritsch, L. Wigstrom, E. Girard-Hughes, and R. Fahrig, *Cardiac C-Arm CT: A Unified Framework for Motion Estimation and Dynamic CT.* Ieee Transactions on Medical Imaging, 2009. **28**(11): p. 1836-1849.

72. T.F. Li, B. Thorndyke, E. Schreibmann, Y. Yang, and L. Xing, *Model-based image reconstruction for four-dimensional PET.* Medical Physics, 2006. **33**(5): p. 1288-1298.

73. A.A. Isola, M. Grass, and W.J. Niessen, *Fully automatic nonrigid registration-based local motion estimation for motion-corrected iterative cardiac CT reconstruction.* Medical Physics, 2010. **37**(3): p. 1093-1109.

74. S.Y. Chun, T.G. Reese, J.S. Ouyang, B. Guerin, C. Catana, X.P. Zhu, N.M. Alpert, and G. El Fakhri, *MRI-Based Nonrigid Motion Correction in Simultaneous PET/MRI.* Journal of Nuclear Medicine, 2012. **53**(8): p. 1284-1291.

75. B. Guerin, S. Cho, S.Y. Chun, X. Zhu, N.M. Alpert, G. El Fakhri, T. Reese, and C. Catana, *Nonrigid PET motion compensation in the lower abdomen using simultaneous tagged-MRI and PET imaging.* Medical Physics, 2011. **38**(6): p. 3025-3038.

76. Y. Petibon, J. Ouyang, X. Zhu, C. Huang, T.G. Reese, S.Y. Chun, Q. Li, and G. El Fakhri, *Cardiac motion compensation and resolution modeling in simultaneous PET-MR: a cardiac lesion detection study.* Physics in Medicine and Biology, 2013. **58**(7): p. 2085-2102.

77. N. White, C. Roddey, A. Shankaranarayanan, E. Han, D. Rettmann, J. Santos, J. Kuperman, and A. Dale, *PROMO: Real-Time Prospective Motion Correction in MRI Using Image-Based Tracking.* Magnetic Resonance in Medicine, 2010. **63**(1): p. 91-105.

78. M. Dawood, F. Buther, X.Y. Jiang, and K.P. Schafers, *Respiratory motion correction in 3-D PET data with advanced optical flow algorithms.* Ieee Transactions on Medical Imaging, 2008. **27**(8): p. 1164-1175.

79. F. Gigengack, L. Ruthotto, M. Burger, C.H. Wolters, X.Y. Jiang, and K.P. Schafers, *Motion Correction in Dual Gated Cardiac PET Using Mass-Preserving Image Registration.* Ieee Transactions on Medical Imaging, 2012. **31**(3): p. 698-712.

80. W.J. Bai and M. Brady, *Regularized B-spline deformable registration for respiratory motion correction in PET images.* Physics in Medicine and Biology, 2009. **54**(9): p. 2719-2736.

81. B.A. Mair, D.R. Gilland, and J. Sun, *Estimation of images and nonrigid deformations in gated emission CT.* Ieee Transactions on Medical Imaging, 2006. **25**(9): p. 1130-1144.

82. L. Livieratos, L. Stegger, P.M. Bloomfield, K. Schafers, D.L. Bailey, and P.G. Camici, *Rigid-body transformation of list-mode projection data for respiratory motion correction in cardiac PET.* Physics in Medicine and Biology, 2005. **50**(14): p. 3313-3322.

83. S. Chen, P. Bravo, M. Lodge, and B.M. Tsui, *Four-dimensional PET image reconstruction with respiratory and cardiac motion compensation from list-mode data.* J NUCL MED MEETING ABSTRACTS, 2012. **2012 53: 106**.

84. F. Lamare, M.J.L. Carbayo, T. Cresson, G. Kontaxakis, A. Santos, C.C. Le Rest, A.J. Reader, and D. Visvikis, *List-mode-based reconstruction for respiratory motion correction in PET using non-rigid body transformations.* Physics in Medicine and Biology, 2007. **52**(17): p. 5187-5204.

85. P. Dasari, K. Johnson, J. Dey, C. Lindsay, M.S. Shazeeb, J.M. Mukherjee, S.K. Zheng, and M.A. King, *MRI Investigation of the Linkage Between Respiratory Motion of the Heart and Markers on Patient's Abdomen and Chest: Implications for Respiratory Amplitude Binning List-Mode PET and SPECT Studies.* Ieee Transactions on Nuclear Science, 2014. **61**(1): p. 192-201.

86. R.L. Harrison, S.D. Vannoy, D.R. Haynor, S.B. Gillispie, M.S. Kaplan, and T.K. Lewellen, *Preliminary Experience with the Photon History Generator Module of a Public-Domain Simulation System for Emission Tomography.* Nuclear Science Symposium & Medical Imaging Conference, Vols 1-3, 1993: p. 1154-1158.

87. S. Jan, G. Santin, D. Strul, S. Staelens, K. Assie, D. Autret, S. Avner, R. Barbier, M. Bardies, P.M. Bloomfield, D. Brasse, V. Breton, P. Bruyndonckx, I. Buvat, A.F. Chatziioannou, Y. Choi, Y.H. Chung, C. Comtat, D. Donnarieix, L. Ferrer, S.J. Glick, C.J. Groiselle, D. Guez, P.F. Honore, S. Kerhoas-Cavata, A.S. Kirov, V. Kohli, M. Koole, M. Krieguer, D.J. van der Laan, F. Lamare, G. Largeron, C. Lartizien, D. Lazaro, M.C. Maas, L. Maigne, F. Mayet, F. Melot, C. Merheb, E. Pennacchio, J. Perez, U. Pietrzyk, F.R. Rannou, M. Rey, D.R. Schaart, C.R. Schmidtlein, L. Simon, T.Y. Song, J.M. Vieira, D. Visvikis, R.V. de Walle, E. Wieers, and C. Morel, *GATE: a simulation toolkit for PET and SPECT.* Physics in Medicine and Biology, 2004. **49**(19): p. 4543-4561.

88. C.L. Chen, Y.C. Wang, J.J.S. Lee, and B.M.W. Tsui, *Integration of SimSET photon history generator in GATE for efficient Monte Carlo simulations of pinhole SPECT.* Medical Physics, 2008. **35**(7): p. 3278-3284.

89. W.P. Segars, G. Sturgeon, S. Mendonca, J. Grimes, and B.M. Tsui, *4D XCAT phantom for multimodality imaging research.* Med Phys, 2010. **37**(9): p. 4902-15.

90. P.G. Danias, M.V. McConnell, V.C. Khasgiwala, M.L. Chuang, R.R. Edelman, and W.J. Manning, *Prospective navigator correction of image position for coronary MR angiography.* Radiology, 1997. **203**(3): p. 733-736.

91. S.K. Balci, G. P, and W. W.M, *Non-rigid Groupwise Registration using B-Spline Deformation Model.* MICCAI Open Science Workshop, 2007.

92. S. Chen, *Development of 4D Image Reconstruction Method with Respiratory Motion Compensation for Oncological PET Imaging.* Ph.D. Dissertation, 2011.

93. K. Thielemans, C. Tsoumpas, S. Mustafovic, T. Beisel, P. Aguiar, N. Dikaios, and M.W. Jacobson, *STIR: software for tomographic image reconstruction release 2.* Physics in Medicine and Biology, 2012. **57**(4): p. 867-883.

94. T. Feng and B.M.W. Tsui, *Non-Rigid Respiratory Motion Correction for 4D Gated PET Sinogram Data.* 2013 Ieee Nuclear Science Symposium and Medical Imaging Conference (Nss/Mic), 2013.

95. J. Wang, G.S.K. Fung, T. Feng, and B.M.W. Tsui. *An interventricular sulcus guided cardiac motion estimation method*. in *Nuclear Science Symposium and Medical Imaging Conference (NSS/MIC), 2013 IEEE*. 2013.

96. K.P. Schafers and L. Stegger, *Combined imaging of molecular function and morphology with PET/CT and SPECT/CT: Image fusion and motion correction.* Basic Research in Cardiology, 2008. **103**(2): p. 191-199.

97. T. Feng, M.A. Ahlman, L. Guo, D.A. Bluemke, and B. Tsui, *Development and evaluation of two 4D image reconstruction methods with dual respiratory and cardiac motion compensation for gated myocardial perfusion PET.* IEEE Nuclear Science Symposium and Medical Imaging (NSS/MIC) Conference Record, 2014.

98. T. Feng, J. Wang, G.S.K. Fung, and B.M.W. Tsui, *Non-rigid dual respiratory and cardiac motion correction methods after, during, and before image reconstruction for 4D cardiac PET.* Under review in Physics in Medicine and Biology, 2015.

99. T. Feng, G.S.K. Fung, J. Xu, J. Wang, and B.M. Tsui, *Maximum likelihood based joint 4D motion vector field estimation and image reconstruction in 4D PET.* J NUCL MED MEETING ABSTRACTS, 2013. **2013 54: 537.**

100. K. Nehrke, P. Bornert, D. Manke, and J.C. Bock, *Free-breathing cardiac MR imaging: Study of implications of respiratory motion-initial results.* Radiology, 2001. **220**(3): p. 810-815.

101. T. Feng, B.M.W. Tsui, X. Li, M. Lodge, N.C.M. Gulaldi, and Z. Szabo, *Evaluation of Image-Derived and Arterial Blood Sampled Input Functions for PET Imaging of the Angiotensin II Subtype I Receptor.* Accepted in Medical Physics, 2015.

Tao Feng

110 w. 39 St, APT 1503

Baltimore, MD 21210

Email: tfeng4@jhu.edu

Phone: +1(443) 927-6712

EDUCATION AND TRAINING:

Ph.D. Johns Hopkins University (Expected in October 2015). Electrical & Computer Engineering.

Dissertation: 4D Image Reconstruction with Dual Respiratory and Cardiac Motion Correction for Cardiac PET. *Adviser: Dr. Benjamin Tsui*

B.Sc. Tsinghua University (June 2010). Engineering Physics. Minor in Computer Science and Engineering

RESEARCH INTERESTS

My areas of expertise are PET/CT and PET/MR imaging, image reconstruction, motion correction, Monte Carlo simulation, kinetic modeling, and SPECT collimator design. Current research topics include: 4D image reconstruction with cardiac and respiratory motion correction for PET/CT and PET/MR. Development and evaluation of PET-based respiratory and cardiac motion estimation methods. Simulation and evaluation of cardiac plaque imaging methods using NaF PET/MR.

I am also interested in

- System design/modeling and simulation.
- Imaging science and imaging physics.
- Task-based image evaluation methods.
- Quantitation reconstruction and image correction methods.

- Tracer evaluation

RESEARCH EXPERIENCE:

September 2010 – Present, Research Assistant, Johns Hopkins University, Baltimore, MD, USA

Supervisor: Dr. Benjamin Tsui

- 4D motion correction for respiratory and cardiac motion on PET scans using listmode data.
- Quantitation of image derived input function for kinetic PET scans using both pig and human data.
- Multi-pinhole collimator design.

July 2014 – July 2015, Internship, MedData Research Inc. Walkersville, MD, USA

Supervisor: Dr. David Bluemke

- 4D motion correction for respiratory and cardiac motion using simultaneously PET/MR.

July 2009 – February 2010, Intern Study, University of Hong Kong, Hong Kong, China

- Combinatorial Group Testing, mathematical form and implementation using C++ and Java.

2006 – 2010, Undergraduate Student Projects, Tsinghua University, Beijing, China

- Virtual Liver Surgery System based on PET at the lab of Medical Physics & Engineering.
- CT Image reconstruction using AMD GPU, Stream computing based on Brook+ and CAL.

JOURNAL PUBLICATIONS:

1. **Tao Feng**, Jizhe Wang, George Fung, Benjamin Tsui, "Non-rigid dual respiratory and cardiac motion correction methods after, during, and before image reconstruction for 4D cardiac PET". Manuscript submitted to Phy. Med. Biol, 2015.

2. **Tao Feng**, Benjamin Tsui, Xin Li, Martin Lodge, Nedim Gulaldi, Zsolt Szabo, "Evaluation of Image-Derived and Arterial Blood Sampled Input Functions for PET Imaging of the Angiotensin II Subtype I Receptor", Manuscript accepted by Medical Physic, 2015.

3. Nedim Gulaldi, Jinsong Xia, **Tao Feng**, Kelvin Hong, William Mathews, Dawn Ruben, Ihab R. Kamel, Benjamin M.W. Tsui and Zsolt Szabo, "Modeling of the Renal Kinetics of the AT1 Receptor Specific PET Radioligand [11C]KR31173", BioMed Research International, 2013.

CONFERENCE PRESENTATIONS AND PROCEDDINGS:

1. **Tao Feng**, Jizhe Wang, Benjamin Tsui, "Development and Evaluation of Four PET Image-Based Dual Respiratory and Cardiac Motion Estimation Methods" accepted for oral presentation at NSS/MIC IEEE 2015.

2. **Tao Feng,** Mark Ahlman, Christoph Kolbitsch, George. Fung, David Bluemke, Benjamin Tsui, "Simulation Study on Factors Affecting the Detectability of Coronary Artery Plaques in NaF PET Imaging" accepted for poster presentation at NSS/MIC IEEE 2015.

3. Jizhe Wang, **Tao Feng**, Benjamin Tsui, "Development and Evaluation of Data-Driven Respiratory Gating Methods with Simulated List-Mode PET Data" accepted for poster presentation in NSS/MIC IEEE 2015.

4. Taek-Soo Lee, Andrew Rittenbach, **Tao Feng**, Benjamin Tsui, "Application of Post Reconstruction Dual Respiratory and Cardiac Motion Compensation for 4D High-Resolution Small Animal Myocardial SPECT Images" accepted for poster presentation in NSS/MIC IEEE 2015.

5. **Tao Feng**, Mark Ahlman, Christoph Kolbitsch, Liheng Guo, Benjamin Tsui, David Bluemke, "Comparison of MR and PET derived respiratory motion estimates for dual respiratory and cardiac motion correction in cardiac PET" Oral presentation in SNMMI 2015, Presenter.

6. Benjamin M. Tsui, Jingyan Xu, Jizhe Wang, **Tao Feng**, M. Abraham, Stefan Zimmerman, "Thomas H. Schindler, "Extraction of Cardiac Motion and Myocardial Contractility from 4D Cardiac PET Images" Oral presentation in SNMMI 2015.

7. Jizhe Wang, **Tao Feng**, Jingyan Xu, Amy Perkins, Benjamin Tsui, "An improved data-driven method for respiratory motion signal detection and magnitude estimation from noisy list-mode cardiac PET data" Oral presentation in SNMMI 2015.

8. **Tao Feng**, Benjamin Tsui, "Non-rigid 4D Respiratory and Cardiac Motion Correction on Projection Data before Image Reconstruction for Cardiac PET", Oral presentation in Fully 3D 2015, Presenter.

9. **Tao Feng**, Mark Ahlman, Liheng Guo David Bluemke, Benjamin Tsui. "Development and evaluation of two 4D image reconstruction methods with dual respiratory and cardiac motion compensation for gated myocardial perfusion PET", Poster presentation in NSS/MIC IEEE 2014.

10. Jizhe Wang, Lingzhi Hu, **Tao Feng**, Jingyan Xu, Lingxiong Shao, Benjamin Tsui, "Improved spatial and temporal resolution of gated myocardial perfusion PET using post reconstruction dual respiratory and cardiac motion compensation", Poster presentation in NSS/MIC IEEE 2014.

11. **Tao Feng**, Mark Ahlman, Benjamin Tsui, Liheng Guo, Mike Guttman, Elliot McVeigh, David Bluemke, "Hybrid MR-guided and PET-guided motion correction of PET images in simultaneous PET/MR", Oral presentation in SNMMI 2014, Presenter.

12. Liheng Guo, Mark Ahlman, **Tao Feng**, Michael Guttman, Elliot McVeigh, David Bluemke, Benjamin Tsui, Daniel Herzka, "Real-time 3D MR respiratory motion acquisition for simultaneous PET/MR imaging", Oral presentation in SNMMI 2014.

13. **Tao Feng**, Benjamin Tsui, "Non-rigid respiratory motion correction for 4D gated PET sinogram data", Poster presentation in NSS/MIC IEEE 2013.

14. Jizhe Wang. George Fung, **Tao Feng**, Benjamin Tsui, "An interventricular sulcus guided cardiac motion estimation method" Oral presentation in NSS/MIC IEEE 2013.

15. Taek-Soo Lee, **Tao Feng**, and Benjamin Tsui, "Application of Image-Based Registration Method for Simultaneous Compensation of Cardiac and Respiratory Motions in Dual Gated Myocardial Perfusion SPECT" Poster presentation in Fully 3D 2013.

16. **Tao Feng**, George Fung, Jingyan Xu, Jizhe Wang, Benjamin Tsui, "Maximum likelihood based joint 4D motion vector field estimation and image reconstruction in 4D PET." Oral presentation in SNMMI 2013, Presenter.

17. Taek-Soo Lee, **Tao Feng**, Benjamin Tsui, "Cardiac and respiratory motion compensation for dual gated SPECT" Poster presentation in SNMMI 2013.

18. Jizhe Wang, George Fung, **Tao Feng**, Benjamin Tsui, "A feature guided cardiac motion estimation method in PET." Oral presentation in SNMMI 2013.

19. Jizhe Wang, George Fung, **Tao Feng**, Benjamin Tsui, "A papillary muscle guided motion estimation method for gated cardiac imaging", Poster presentation in SPIE 2013.

20. **Tao Feng**, Benjamin Tsui, Xin Li, Martin Lodge, Nedim Gulaldi, Zsolt Szabo, "Evaluation of image-derived and arterial blood sampled input functions for PET imaging of the angiotensin II subtype I receptor." Oral presentation in SNM 2012, Presenter.

21. Yajie Wang, **Tao Feng**, Le Shen, Yuxiang Xing, "Research on ATI-CAL for accelerating FBP reconstruction" Poster presentation in NSS/MIC IEEE 2009.

22. **Tao Feng**, Yajie Wang, Yiming Wang, Yuxiang Xing, "Acceleration of 3D CT Backprojection Based on ATI Stream Computing" Poster presentation in Fully 3D HPIR workshop 2009, presenter.

INVITED TALKS

2013 4D Image Reconstruction with Respiratory and Cardiac Motion Correction on Positron Emission Tomography (PET), National Institutes of Health, Bethesda, MD, August 2013.

2015 Motion Correction with Combined MR and PET Information, Siemens Biograph mMr Cardiac Imaging Workshop, Cedars-Sinai Hospital, Los Angeles, CA, June 2015.

TEACHING EXPERIENCE:

- January 2014, Co-instructor, EN.600.146.13, Introduction to Medical Imaging (Intersession), Johns Hopkins University, Baltimore, MD, USA.

- Spring 2013, Course Assistant, ECE/BME 520.434/580.472, Modern Biomedical Imaging Instrumentation & Techniques, Johns Hopkins University, Baltimore, MD, USA.

SERVICES, ACTIVITIES AND VOLUNTEER WORK:

- Journal club organizer: Help organizing weekly journal clubs in Division of Medical Imaging Physics (DMIP). Duties include finding presenter, organize group lunch, and maintaining journal club website.
- Elected DMIP Student Representative: Duties include bridging the communications between students and faculties, help students with their issues.

LANGUAGES

English: Fluent, Chinese (Mandarin): Fluent

COMPUTER SKILLS:

C/C++, MATLAB, Microsoft Windows, Microsoft Office, EndNote, Linux, ImageJ, MIPAV, Perl, Python, Shell scripts, GATE (Geant4 Application for Tomographic Emission), STIR (Software for Tomographic Image Reconstruction)